Sensing and Estimation of Airflow Angles and Atmospheric Winds for Small Unmanned Aerial Vehicles

Pengzhi Tian

Submitted to the graduate degree program in Department of Aerospace Engineering and the Graduate Faculty of the University of Kansas in partial fulfillment of the requirements for the degree of Doctor of Philosophy.

Committee members

Dr. Haiyang Chao, Chairperson

Dr. Shawn Keshmiri

Dr. Bozenna Pasik-Duncan

Dr. Craig McLaughlin

Dr. Zhongquan Zheng

Date defended: June 03, 2020

The Dissertation Committee for Pengzhi Tian certifies
that this is the approved version of the following dissertation :

Sensing and Estimation of Airflow Angles and Atmospheric Winds for Small Unmanned Aerial Vehicles

Dr. Haiyang Chao, Chairperson

Date approved: June 04, 2020

Abstract

This dissertation focuses on development of new sensing, estimation, and analysis methods for unmanned aerial vehicle (UAV) operations in dynamic wind fields. Three main problems are studied, including airflow angle estimation, 3D wind estimation, and UAV wake encounter identification, simulation, and validation. A thorough survey is performed first on wind sensing and estimation methods using fixed-wing UAVs. Four flow angle estimation filters are then proposed and validated for accurate UAV flow angle estimation at low cost. Furthermore, two 3D wind estimation filters are proposed for small fixed-wing UAVs and validated by utilizing different wind models. Finally, a novel UAV wake encounter simulation platform is developed to simulate UAV response during wake encounters and compared with results from close formation wake encounter flight.

Acknowledgements

First and foremost, I would like to take this opportunity to thank everyone who has been on this journey with me. Thank you Dr. Haiyang Chao, my Ph.D. advisor, thank you for offering me the great opportunity to work on these exciting projects and supporting me without reservation throughout my Ph.D. study. Thank you my committee members, Dr. Shawn Keshmiri, Dr. Bozenna Pasik-Duncan, Dr. Craig McLaughlin, and Dr. Zhongquan Zheng, thank you for always being there to answer my questions and give me valuable feedback.

I would like to thank my collaborators, Dr. Nathaniel A. Brunsell, Dr. Huazhen Fang, Harold Patrick Flanagan, Saket Gowravaram, Dr. Yu Gu, Jacksen Hugh Goyer, Steven G. Hagerott, Dr. Anpeng He, and Dr. Huixuan Wu, thank you for your continued support and valuable inputs on my research.

I would also like to thank all friends and colleagues I met at KU. Thank you all for your friendship and support throughout the years.

Many thanks go to my major funding support from the University of Kansas, NASA, NASA-KS-EPSCoR, and USDA-NIFA.

Last but not least, I would like to express my deepest gratitude to my family:
感谢我的父母、爱人，感谢你们一路上对我的支持，感谢你们对我无私的爱。
感谢我的儿子致远小朋友，你灿烂的笑容是我前行路上无尽动力的源泉。

Contents

List of Figures

List of Tables

Chapter 1

Introduction

1.1 Background and Motivation

With the emergence of autonomous technologies, unmanned aerial vehicles (UAVs) are becoming ubiquitous in both military and civilian markets. Example applications include aerial photography, precision agriculture, human and cargo transportation, infrastructure inspection, disaster damage assessment, meteorological measurement, wildfire monitoring, chemical leak detection and monitoring, as well as search and rescue. However, it is still very challenging to maintain safe and efficient UAV operations in places where complex and dynamic flow fields are present, such as urban cities, mountainous areas, wildfire burning sites, or high-traffic airports. Unlike autonomous ground vehicles which interact with roads, traffic, and pedestrians, UAVs interact mainly with surrounding flow/wind fields. The flow fields surrounding UAVs could be atmospheric winds generated by weather patterns, structure/building induced vortices and turbulence, or wake vortices generated by other manned aircraft or UAVs. These dynamic winds can greatly affect flight safety and performance, especially for small UAVs as they are slower in speed and lighter in weight. On the other hand, the presence of certain flow fields, especially thermals, wind shear, and wake vortex, can help increase the endurance of UAVs if proper knowledge of flow fields is known and correct control maneuvers are performed. A thorough investigation on wind-UAV interactions will not only help develop enabling technologies for improved safety and autonomy of UAVs but also help government agencies propose new regulations for the seamless integration of UAVs into our everyday lives. This dissertation is to study the interactions between UAVs and surrounding flow fields from the sensing and estimation perspective. Three problems are focused on including air-

flow angle estimation (angle of attack (AOA/α) and angle of sideslip (AOS/β)), UAV based 3D wind estimation, and UAV wake encounter simulation and flight validation. The motivations for each of the three problems are described briefly as below.

Airflow angles or flow angles, including AOA and AOS, are critical to the safety and flight performance of any manned or unmanned aircraft, as they have a big impact on associated aerodynamic forces and moments. The importance of AOA and AOS is shown in the 2018 and 2019 Boeing 737 MAX accidents. Although there are existing sensors that can measure AOA and AOS directly, these sensors are generally expensive or require extensive calibrations. Additionally, UAVs are often limited by size and weight. Therefore, it is important to design novel algorithms/filters to estimate AOA and AOS instead of measuring them directly. The estimated AOA and AOS can be used to improve the safety and efficiency of small UAVs for applications such as stall detection, sensor fault detection, thermal soaring, etc.

In addition to airflow angles, sensing and estimation of wind and turbulence are also very important for the safety and performance of UAVs. Challenges here are mainly due to the highly dynamic spatio-temporal characteristic of wind and noisy direct or indirect flow angle measurements onboard UAVs. Therefore, novel filters combining different wind models and UAV kinematic-dynamic responses are necessary for accurate wind estimation along the UAV flight trajectory. Given estimated 3D wind information, it is possible to identify certain spatial patterns of wind fields, such as thermals, wind shear, and wake vortex.

Of many different types of dynamic wind fields, wake vortex is one particular type that is often encountered by aircraft, especially at busy airports or during close formation flight. In the near future, manned aircraft may share the same airport as flying taxis or cargo UAVs, which raises serious safety concerns. Therefore, it is crucial to be able to predict UAV responses during wake encounters through simulation analysis and flight validations.

1.2 Dissertation Contributions

To address challenges mentioned above, this dissertation thoroughly investigated and summarized the existing work in wind sensing and estimation using small fixed-wing UAVs; proposed several novel filters for estimation of AOA, AOS, and 3D wind; and developed a new framework for UAV wake encounter simulation. The major contributions of this dissertation include the followings:

1. Provided a thorough survey of wind representation models, available UAV sensors, and algorithms for UAV based wind sensing and estimation;

2. Proposed a novel complementary filter (CF) and a novel extended Kalman filter (EKF) for the estimation of AOA and AOS without relying on direct flow angle measurements and GPS measurements;

3. Simulation and flight test evaluation of four different types of AOA and AOS estimation filters using two different UAV platforms under nominal flight conditions and aggressive maneuvers;

4. Proposed a 9-state EKF to estimate 3D wind using small fixed-wing UAVs without relying on direct flow angle measurements;

5. Proposed a 12-state EKF for UAV based 3D wind estimation, which combines the sinusoidal wave model with the typical random walk process to model wind dynamics;

6. Simulation and flight test validations of proposed 3D wind estimation filters, and comparison between UAV based wind estimates and ground 3D wind measurements from a weather station;

7. Development of HawkWakeSim, a novel wake encounter simulator with coupled aerodynamics and flight dynamics, and cross validation of the developed simulator using wake encounter data identified from UAV close formation flights.

1.3 Dissertation Organization

The organization of this dissertation can be summarized as follows. In Chapter 1, the research motivations and dissertation contributions are introduced. In Chapter 2, the general problem of small fixed-wing UAV based wind field sensing and estimation is described and a thorough survey is provided. Chapter 3 focuses on the development of novel filters for inertial flow angle estimation of small UAVs. Chapter 4 presents two new EKFs for 3D wind estimation using small fixed-wing UAVs. In Chapter 5, HawkWakeSim, a novel UAV wake encounter simulator, is introduced with coupled aerodynamics and flight dynamics. Finally, conclusions and future work are be summarized in Chapter 6.

Chapter 2

Wind Sensing and Estimation Using Small Fixed-Wing UAVs: A Survey

Abstract

For future unmanned aerial vehicle (UAV) beyond visual line of sight (BVLOS) operations, it is essential to have the knowledge of the wind along the UAV trajectory and predict the wind field ahead for improved flight safety and efficiency. This chapter provides a survey of the state of the art sensors and estimation algorithms for wind estimation using small fixed-wing UAVs. Different types of wind models are investigated first from existing work, which include time domain models, power spectral density (PSD) based frequency domain models, and spatial domain models. Representative UAV sensors showing the wind impact on UAVs are then compared and discussed, together with typical statistical estimation filters. Finally, summaries of existing wind estimation approaches and recommendations are provided for interested researchers.

2.1 Introduction

The awareness of surrounding flow fields or wind is critical to safe and efficient flight of manned and unmanned aircraft, especially for small unmanned aerial vehicles (UAVs). However, it is not easy to measure or estimate winds surrounding aircraft despite their persistent existence. The difficulty lies in the cost and payload limit of small UAVs as well as spatio-temporal dynamics of wind fields, as they are continuously changing over space and time. The general problem of wind

sensing and estimation using small UAVs can be divided into two categories, (1) wind sensing and estimation along the UAV flight trajectory at specific time and locations; (2) wind field estimation by considering the spatio-temporal characteristic of wind.

The classical wind sensing and estimation problem along the aircraft flight trajectory can be tackled by solving the wind triangulation equation, Eq. (2.1), which is depicted in Fig. 2.1. $\boldsymbol{V_g}$ $[V_n, V_e, V_d]$ is the ground speed expressed in the north-east-down (NED) inertial frame, $\boldsymbol{V}$ $[u, v, w]$ is the airspeed expressed in the body frame, $\boldsymbol{V}_{\mathrm{w}}$ $[\mathrm{w}_n, \mathrm{w}_e, \mathrm{w}_d]$ is the wind speed expressed in the NED frame, and $\boldsymbol{R_b^n}(\phi, \theta, \psi)$ is the rotation matrix from the body frame to the NED frame shown in Eq.(2.2). The most straight forward way for UAV based wind sensing is to directly measure all related variables in Eq. (2.1) and perform direct calculations. However, not every parameter can be easily or accurately measured. For example, it is rare for UAVs to have direct measurements of 3D airspeed $\boldsymbol{V}$ $[u, v, w]$. Some UAVs are equipped with an air data system (ADS) to measure air triplets, including the true airspeed V, angle of attack AOA/α, and sideslip angle AOS/β. With measured $[V, \alpha, \beta]$, $[u, v, w]$ can be calculated by Eq.(2.3). However, a high fidelity ADS that can provide air triplets measurements is usually very expensive and requires extensive calibration, not to say that UAVs especially small ones are usually limited by space and weight. In recent years, the development of cheaper, smaller, and more powerful microprocessors and sensors makes it possible to use delicately designed statistical algorithms to solve these problems/equations. Ultimately, it becomes a trade off between direct measurement (hardware/sensors) and estimation (software/algorithms).

$$\begin{bmatrix} \mathrm{w}_n \\ \mathrm{w}_e \\ \mathrm{w}_d \end{bmatrix} = \begin{bmatrix} V_n \\ V_e \\ V_d \end{bmatrix} - \boldsymbol{R_b^n}(\phi, \theta, \psi) \begin{bmatrix} u \\ v \\ w \end{bmatrix}, \tag{2.1}$$

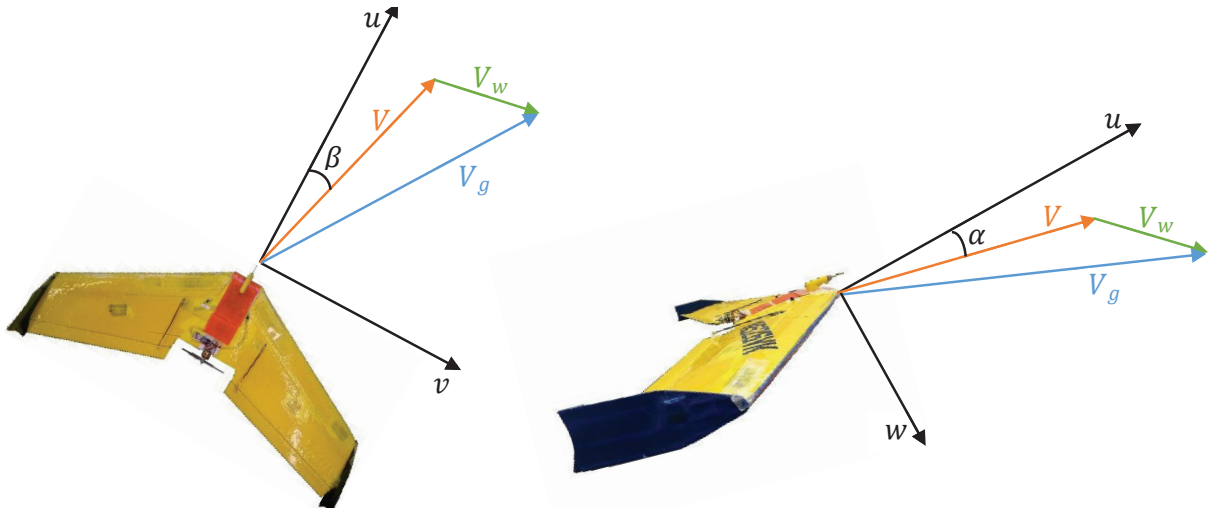

Figure 2.1: Wind triangle illustration.

$$\boldsymbol{R}_{\boldsymbol{b}}^{\boldsymbol{n}}(\phi,\theta,\psi) = \begin{bmatrix} \cos\psi\cos\theta & -\sin\psi\cos\phi+\cos\psi\sin\theta\sin\phi & \sin\psi\sin\phi+\cos\psi\sin\theta\cos\phi \\ \sin\psi\cos\theta & \cos\psi\cos\phi+\sin\psi\sin\theta\sin\phi & -\cos\psi\sin\phi+\sin\psi\sin\theta\cos\phi \\ -\sin\theta & \cos\theta\sin\phi & \cos\theta\cos\phi \end{bmatrix} \tag{2.2}$$

$$\begin{bmatrix} V \\ \alpha \\ \beta \end{bmatrix} = \begin{bmatrix} \sqrt{u^2+v^2+w^2} \\ \tan^{-1}(\frac{w}{u}) \\ \sin^{-1}(\frac{v}{V}) \end{bmatrix}. \tag{2.3}$$

Given measured or estimated wind information along the UAV trajectory, the spatio-temporal variations of the wind field can be further derived. This requires good measurements or estimates of wind along the UAV trajectory at specific time and locations, as well as appropriate models for accurate wind field interpolation, extrapolation, or reconstruction. The simplest approach is to assume that the wind field is frozen, or the wind field does not change in a relatively short time period when the UAV flies over. Spatial variations of the wind field can then be treated as functions of 3D positions. For certain applications like thermal soaring, the problem can be further simplified by considering wind variations in only one dimension, usually vertically. Alternatively, wind field can be analyzed from perspectives of power spectral density (PSD) or total energy where the focus

is on the wind energy distribution and its impact on UAVs instead of spatio-temporal variations.

This chapter provides a comprehensive survey of existing wind sensing and estimation methods using small fixed-wing UAVs, including wind models, sensors, and estimation algorithms. The objective is to provide an overview of the state of the art UAV based wind estimation methods in a hope to motivate new breakthroughs in the interdisciplinary area of guidance, navigation, and control (GNC) and aerodynamic or fluid dynamic communities. This chapter can also serve as a selection guide for researchers who want to develop customized UAVs for wind measurements. The major contributions of this chapter can be summarized as follows:

1. A survey of typical wind models for UAV based wind sensing and estimation;
2. A survey of available sensors for UAV based wind sensing and estimation;
3. A summary of existing approaches for UAV based wind sensing and estimation;
4. Potential future directions for UAV based wind estimation.

The organization of this chapter can be summarized as follows. The wind representation and modeling are described in Sec. 2.2. Available UAV sensors for wind sensing and estimation are introduced and compared in Sec. 2.3. The most commonly used algorithms for UAV based wind estimation are presented in Sec. 2.4. Summaries of existing work and recommendations for selection of wind models, sensors, and algorithms are presented in Sec. 2.5. Future directions and conclusions are made in Sec. 2.6.

2.2 Wind Representation and Modeling

The wind can be generally described as the superposition of mean wind, waves, and gust [1]. Mean wind speed is the wind speed averaged over a specific time interval, which can also be treated as the prevailing wind for many cases. In contrast, a gust is a brief and sudden increase in wind speed along a specific direction, the duration of which is usually less than 20 seconds. Example wind measurements from a Campbell Scientific ultrasonic wind anemometer (CSAT3B) are shown in Fig. 2.2, where the data is 500 seconds in total at a sampling rate of 100 Hz. Corresponding

Periodogram and Welch PSD plots are shown in Fig. 2.3 and Fig. 2.4, respectively. There exist different types of prevailing wind and gust models. Wind representation and modeling in this section is divided into three categories, temporal models, PSD models, and spatial models.

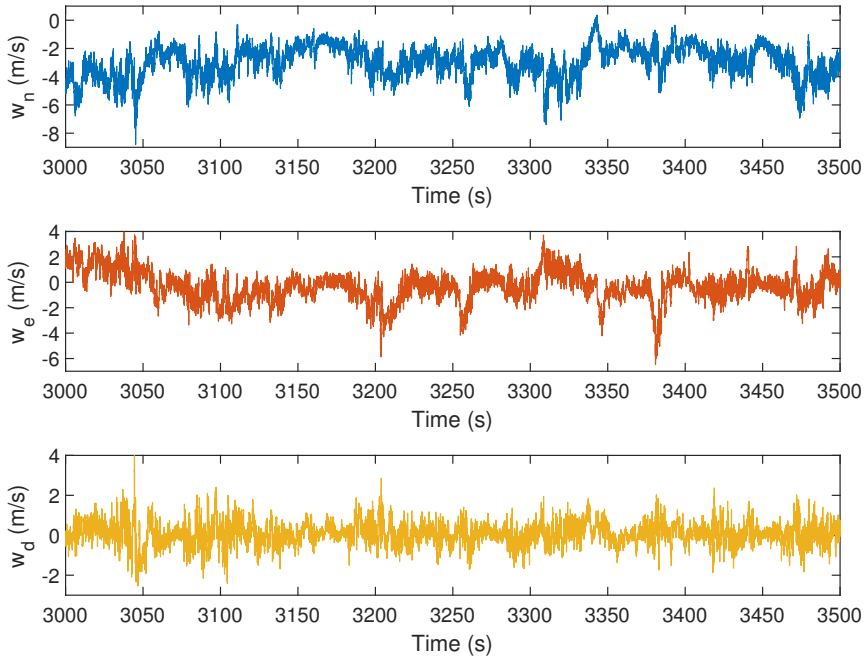

Figure 2.2: Ultrasonic wind anemometer measurements.

2.2.1 Temporal Wind Models

Due to the non-deterministic nature of wind, stochastic models such as random walk (RW) models have been widely used to represent wind speed changes. Two of the most commonly used temporal wind models are the first order and the second order RW models, which are based on Gaussian RW processes and Markov chain models. These two temporal wind models are widely used in the wind energy community for synthetic wind speed generations and prevailing wind estimation [2, 3].

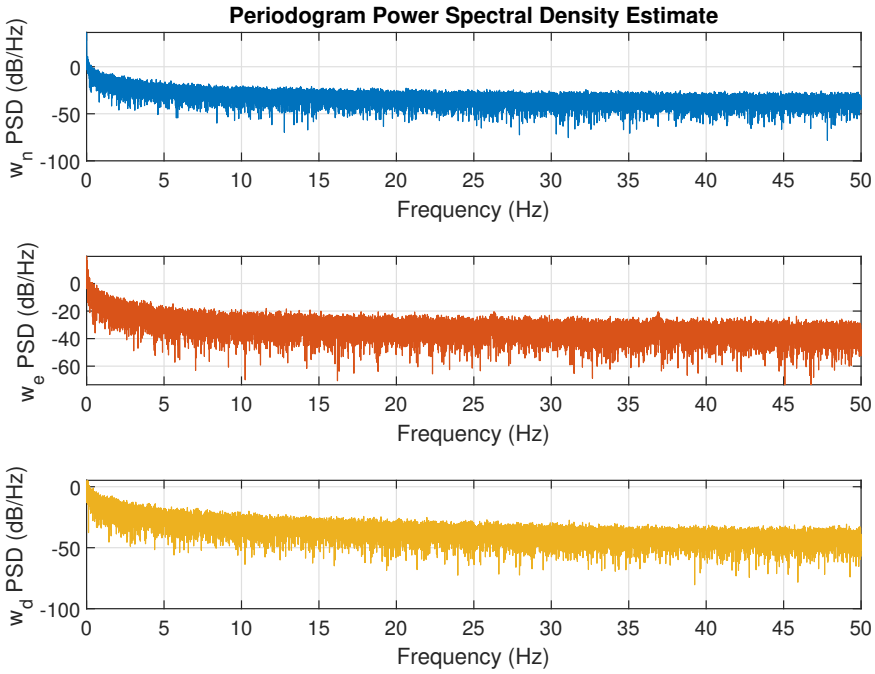

Figure 2.3: Periodogram PSD of ultrasonic wind anemometer measurements.

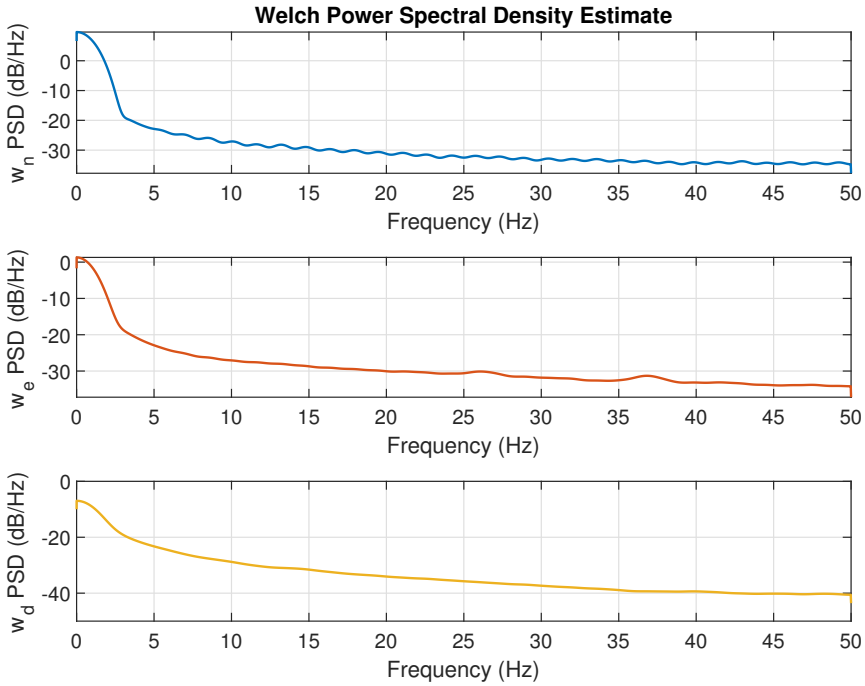

Figure 2.4: Welch PSD of ultrasonic wind anemometer measurements.

2.2.1.1 First Order Random Walk Model

By assuming wind dynamics as first order Gaussian RW processes, the wind model can be derived as Eq.(2.4), where $\mathbf{w_{wk}}$ is zero-mean white Gaussian noise and $[\mu_n, \mu_e, \mu_d]$ is the wind acceleration expressed in the NED frame. The first order RW model can also be referred to as the slowly evolving wind model.

$$\begin{bmatrix} \dot{w}_n \\ \dot{w}_e \\ \dot{w}_d \end{bmatrix} = \begin{bmatrix} \mu_n \\ \mu_e \\ \mu_d \end{bmatrix} = \begin{bmatrix} 0 \\ 0 \\ 0 \end{bmatrix} + \mathbf{w_{wk}}. \tag{2.4}$$

2.2.1.2 Second Order Random Walk Model

Similarly, wind dynamics can be modeled as second order Gaussian RW processes as shown in Eq.(2.5) and Eq.(2.6), where $\mathbf{w}_{\mu\mathbf{k}}$ is zero-mean white Gaussian noise.

$$\begin{bmatrix} \dot{w}_n \\ \dot{w}_e \\ \dot{w}_d \end{bmatrix} = \begin{bmatrix} \mu_n \\ \mu_e \\ \mu_d \end{bmatrix}, \tag{2.5}$$

$$\begin{bmatrix} \ddot{w}_n \\ \ddot{w}_e \\ \ddot{w}_d \end{bmatrix} = \begin{bmatrix} \dot{\mu}_n \\ \dot{\mu}_e \\ \dot{\mu}_d \end{bmatrix} = \begin{bmatrix} 0 \\ 0 \\ 0 \end{bmatrix} + \mathbf{w}_{\mu\mathbf{k}}. \tag{2.6}$$

Compared with the first order RW process, the second order RW process has a longer memory of historical data and the underlying correlation. Researchers have found that the second order RW process is more accurate in generating synthetic wind speed time series [2, 3]. Another advantage of using the second order RW model is that it allows wind accelerations be explicitly included in the UAV dynamic equations, as shown in Eq.(2.7) [4], where $\boldsymbol{R_n^b}(\phi, \theta, \psi) = \boldsymbol{R_b^n}(\phi, \theta, \psi)^\mathsf{T}$ is the

rotation matrix from the NED frame to the body frame. However, as more states are introduced in the second order RW model, it makes the implementation more difficult and may make the tuning process harder if used in stochastic filters.

$$\begin{bmatrix} \dot{u} \\ \dot{v} \\ \dot{w} \end{bmatrix} = \begin{bmatrix} -qw + rv - g\sin\theta + a_x \\ -ru + pw + g\cos\theta\sin\phi + a_y \\ -pv + qu + g\cos\theta\cos\phi + a_z \end{bmatrix} - \boldsymbol{R}_{\boldsymbol{n}}^{\boldsymbol{b}}(\phi,\theta,\psi) \begin{bmatrix} \mu_n \\ \mu_e \\ \mu_d \end{bmatrix}. \tag{2.7}$$

2.2.2 Power Spectral Density Based Wind Models

In addition to the time domain wind modeling, frequency domain models, especially PSD models, are also widely used to represent wind variations. Frequency domain models can provide information of wind energy distribution across different frequencies. PSD is often used for continuous gust/turbulence modeling and for flight controller validation. A continuous gust profile is also referred to as turbulence. The turbulence V_{w_t} can be considered as the combination of a series of individual gust and is often idealized as a stationary Gaussian random process. A stationary Gaussian random process can be generated by the superposition of an infinite number of sinusoidal components using Eq. (2.8) [5], where $\Phi(\omega_k)$ is the PSD function, ω_k is the frequency of each individual component, and Ψ_k is the random phase angle. Among a variety of continuous gust models, the von Kármán and Dryden models are most commonly used PSD functions for flight controller design and turbulence modeling in aircraft gust load analysis.

$$\mathbf{V}_{\mathrm{w_t}}(t) = \sum_{k=1}^{\infty} \sqrt{\Phi(\omega_k)\Delta\omega}\cos(\omega_k t + \Psi_k). \tag{2.8}$$

2.2.2.1 Dryden Wind Turbulence Model

The mathematical expressions for the Dryden wind turbulence model are shown in Eqs. (2.9) - (2.14) [6], where $[\Phi_{\mathrm{w}_{tu}}(\omega), \Phi_{\mathrm{w}_{tv}}(\omega), \Phi_{\mathrm{w}_{tw}}(\omega)]$ represent power spectral densities of turbulence along UAVs' body axes. V_{w_t} $[\mathrm{w}_{tu}, \mathrm{w}_{tv}, \mathrm{w}_{tw}]$ and $[\Phi_{p_t}(\omega), \Phi_{q_t}(\omega), \Phi_{r_t}(\omega)]$ represent power spectral densities for three angular velocity components caused by turbulence $[p_t, q_t, r_t]$. b is the aircraft

wingspan, σ_{w_*} is the turbulence intensity, and L_{w_*} is the turbulence length scale, which is a function of altitude. Note that $_t$ stands for turbulence.

$$\Phi_{w_{tu}}(\omega) = \frac{2\sigma_{w_{tu}}^2 L_{w_{tu}}}{\pi V} \cdot \frac{1}{1+\left(L_{w_{tu}}\frac{\omega}{V}\right)^2}, \tag{2.9}$$

$$\Phi_{w_{tv}}(\omega) = \frac{\sigma_{w_{tv}}^2 L_{w_{tv}}}{\pi V} \cdot \frac{1+3\left(L_{w_{tv}}\frac{\omega}{V}\right)^2}{\left[1+\left(L_{w_{tv}}\frac{\omega}{V}\right)^2\right]^2}, \tag{2.10}$$

$$\Phi_{w_{tw}}(\omega) = \frac{\sigma_{w_{tw}}^2 L_{w_{tw}}}{\pi V} \cdot \frac{1+3\left(L_{w_{tw}}\frac{\omega}{V}\right)^2}{\left[1+\left(L_{w_{tw}}\frac{\omega}{V}\right)^2\right]^2}, \tag{2.11}$$

$$\Phi_{p_t}(\omega) = \frac{\sigma_{w_{tw}}^2}{V L_{w_{tw}}} \cdot \frac{0.8\left(\frac{\pi L_{w_{tw}}}{4b}\right)^{\frac{1}{3}}}{1+\left(\frac{4b\omega}{\pi V}\right)^2}, \tag{2.12}$$

$$\Phi_{q_t}(\omega) = \frac{\pm\left(\frac{\omega}{V}\right)^2}{1+\left(\frac{4b\omega}{\pi V}\right)^2} \cdot \Phi_{w_{tw}}(\omega), \tag{2.13}$$

$$\Phi_{r_t}(\omega) = \frac{\mp\left(\frac{\omega}{V}\right)^2}{1+\left(\frac{3b\omega}{\pi V}\right)^2} \cdot \Phi_{w_{tv}}(\omega). \tag{2.14}$$

2.2.2.2 Von Kármán Wind Turbulence Model

The von Kármán wind turbulence model describes the continuous gusts by using similar parameters as the Dryden wind turbulence model. The major difference between these two models is that the von Kármán model has irrational PSDs for linear velocity components while the Dryden model has rational ones. Mathematical expressions for the von Kármán model are shown in Eq. (2.15) - (2.17) [7]. Power spectral densities for three angular velocity components of von Kármán turbulence are the same with those in the Dryden turbulence model, shown in Eq. (2.12) - (2.14).

$$\Phi_{w_{tu}}(\omega) = \frac{2\sigma_{w_{tu}}^2 L_{w_{tu}}}{\pi V} \cdot \frac{1}{\left[1+\left(1.339 L_{w_{tu}}\frac{\omega}{V}\right)^2\right]^{\frac{5}{6}}}, \tag{2.15}$$

$$\Phi_{w_{tv}}(\omega) = \frac{\sigma_{w_{tv}}^2 L_{w_{tv}}}{\pi V} \cdot \frac{1 + \frac{8}{3}\left(1.339 L_{w_{tv}} \frac{\omega}{V}\right)^2}{\left[1 + \left(1.339 L_{w_{tv}} \frac{\omega}{V}\right)^2\right]^{\frac{11}{6}}}, \tag{2.16}$$

$$\Phi_{w_{tw}}(\omega) = \frac{\sigma_{w_{tw}}^2 L_{w_{tw}}}{\pi V} \cdot \frac{1 + \frac{8}{3}\left(1.339 L_{w_{tw}} \frac{\omega}{V}\right)^2}{\left[1 + \left(1.339 L_{w_{tw}} \frac{\omega}{V}\right)^2\right]^{\frac{11}{6}}}. \tag{2.17}$$

Note that both models assume the wind turbulence is varying in space but frozen in time, and they rely on UAVs' motion through the turbulence field to generate temporal variations in wind speed (they are expressed in UAVs' body frame instead of the NED frame). These two turbulence models can be incorporated into UAVs' equations of motion as wind disturbances. Compared with the Dryden model, the von Kármán model generally fits the wind measurements better. However, the desired filter implementations of the von Kármán model can only be approximated due to its irrational PSDs.

2.2.3 Spatial Wind Models

In addition to temporal wind speed correlations, certain wind fields also have strong correlations with the spatial information. Examples include mountain waves, thermal wind, and aircraft wake vortex. A general spatial wind field can be modeled by a function correlating 3D wind speed and 3D positions. The most intuitive way of finding the correlation function is using a polynomial, which may be difficult to find for a general wind field. Two other methods that are also widely used include empirical models and computational fluid dynamic (CFD) based models. Empirical modeling is to model certain types of spatial wind fields based on former experience and measurements. Example empirical models include wind shear model, discrete gust model, and thermal model [6, 8, 9]. CFD models often require the knowledge of surrounding structures/terrains with high computational costs.

2.2.3.1 Wind Shear Model

There are two wind shear models that are widely used [8]. The first one is the wind profile power law, shown in Eq. (2.18) [10], where V_{w_h} is the horizontal wind speed $\sqrt{{w_n}^2+{w_e}^2}$, h is the altitude, and h_r is the altitude where the reference horizontal wind speed $V_{w_{h_r}}$ is measured at. The wind shear exponent γ is an empirical coefficient, which varies with the stability condition of the atmosphere. For nominal conditions, γ is approximately $1/7$. The second one is the wind profile log law, shown in Eq.(2.19) [11], where $V_{w_{h_6}}$ is the horizontal wind speed measured at 6 meters above the ground and z_0 is an empirical constant. Both models can be used to predict or extrapolate wind speed at a certain altitude while their relative accuracy in predicting the mean wind changes at different altitudes. The study of wind shear can help small UAVs extract energy from the atmosphere (dynamic soaring) to achieve longer flight endurance.

$$V_{w_h} = V_{w_{h_r}} \left(\frac{h}{h_r}\right)^{\gamma}, \tag{2.18}$$

$$V_{w_h} = V_{w_{h_6}} \frac{\ln\left(\frac{h}{z_0}\right)}{\ln\left(\frac{6}{z_0}\right)}. \tag{2.19}$$

2.2.3.2 Discrete Gust Model

One widely used idealized gust model is the one-minus-cosine gust model. The one-minus-cosine model is often used to describe an individual gust, or so called a discrete gust [6]. The mathematical expression for the one-minus-cosine model is shown in Eq. (2.20), where V_{m_g} is the gust amplitude, d_{m_g} is the gust length, x is the distance traveled, and V_{w_g} is the resultant wind velocity in the body axis frame. Note that $_g$ stands for the discrete gust.

$$V_{w_g} = \begin{cases} 0 & x < 0 \\ \frac{V_{m_g}}{2}\left(1-\cos\left(\frac{\pi x}{d_{m_g}}\right)\right) & 0 \le x \le d_{m_g} \\ V_{m_g} & x > d_{m_g} \end{cases} \tag{2.20}$$

2.2.3.3 Thermal Model

Thermals, commonly referred to as updrafts, are columns of rising air generated by the uneven ground surface heating. The vertical wind speed within an individual thermal column decays from the maximum magnitude at the thermal center following a bell shape, as shown in Eq. (2.21) [9], where $\mathrm{w}_z(x,y)$ is the vertical wind speed at position (x,y), (x_0,y_0) is the position of the thermal center/core, and R_0 is the radius of the thermal column. In this model, the thermal column is assumed to be stationary, where its position and vertical speed distribution does not change over the time. The study of thermals can help small UAVs extract energy from the atmosphere (static soaring) for long range flight.

$$\mathrm{w}_z(x,y) = \mathrm{w}_z(x_0,y_0)e^{-\left(\frac{(x-x_0)^2+(y-y_0)^2}{{R_0}^2}\right)}\left[1-\left(\frac{(x-x_0)^2+(y-y_0)^2}{{R_0}^2}\right)\right]. \tag{2.21}$$

2.2.3.4 Wake Vortex Model

Wake vortex, also known as wake turbulence, is an atmospheric disturbance that generated by a flying aircraft when the air below the wing circulate around the wingtip due to the pressure difference. The generated wingtip vortices are counter-rotating pairs that trail from wingtips and can remain in the air for several minutes after the aircraft flies by. Burnham-Hallock model, a commonly used wake vortex model, is shown in Eq. (2.22) [12], where Γ_0 is the initial wake vortex strength, r_c is the vortex core radius, r is the radial distance to the vortex filament center line. The initial wake vortex strength is primarily determined by the airspeed and the weight (lift) of the aircraft. The decaying of the generated wake vortex can be described as different models such as Sarpkaya decay model [13]. Real time measurement of wake vortex locations is critical to fuel saving formation flight of manned and unmanned aircraft [14].

$$\mathrm{w}_\theta(r) = \frac{\Gamma_0}{2\pi r}\frac{r^2}{r^2+r_c^2}. \tag{2.22}$$

2.2.3.5 Terrain Based CFD Model

Other than empirical models mentioned in previous subsections, winds can also be represented and simulated using CFD models [15, 16]. The CFD wind models can be used to compute spatially varying wind fields, and they are generally accurate if initial conditions, boundary conditions, and surrounding/terrain information are known. However, CFD models are often computationally expensive.

2.3 UAV Sensors for Wind Sensing and Estimation

The impact of wind and turbulence on aircraft often shows in aircraft kinematics and dynamics [4]. Sensors presented in this section are those commonly used or have the potential to be used on fixed-wing UAVs to facilitate the sensing and estimation of wind fields. Based on Eq. (2.1) and Eq. (2.3) and considering wind fields estimation, the required sensors can be summarized as four major categories.

1. Sensors to measure/estimate UAVs' position $[p_n, p_e, p_d]$ and ground speed $[V_n, V_e, V_d]$, which are required to solve wind triangulation or for spatial wind field modeling;
2. Sensors to measure/estimate UAVs' orientation $[\phi, \theta, \psi]$, which are required for coordinate transformations between the body frame and the NED frame;
3. Sensors to measure/estimate air triplets $[V, \alpha, \beta]$, which are required to solve wind triangulation and for coordinate transformations between the wind frame and the body frame;
4. Sensors to measure/estimate UAVs' inertial and dynamic response to wind and turbulence $[a_x, a_y, a_z]$, $[p, q, r]$, $[\delta_a, \delta_e, \delta_r, \delta_t]$.

2.3.1 Sensors for Position and Ground Speed Measurements

Currently, most of unmanned aircraft systems rely on the Global Positioning System (GPS) for localization. In fact, many GPS receivers can also provide very accurate ground speed measure-

ments $[V_n, V_e, V_d]$ by utilizing carrier phase effect. Many GPS receivers used on small UAVs have an update rate within the range of 5 - 10 Hz and with the accuracy of a couple of meters. There are several ways to improve the accuracy of GPS, including sensor fusion with multi GPS antennas and real-time kinematic (RTK) GPS [17]. A typical differential GPS setup can achieve centimeter level accuracy, however, is usually more expensive. Comparisons of several typical GPS receivers are shown in Table 2.1. Researchers have also started to work on the problem position and velocity estimation in GPS degraded/denied environments. The most widely used alternative navigation technique is vision aided, which involves sensors such as cameras and LiDARs.

Table 2.1: Comparison of typical GPS receivers

	Horizontal Position Accuracy (CEP)	Velocity Accuracy	Heading Accuracy	Max Update Rate	Approximate Cost
Ublox LEA-6H	2.5 m	0.1 m/s	0.5 deg	5 Hz	90 USD
Ublox NEO-M8P	2.5 m	0.05 m/s	0.3 deg	10 Hz	150 USD
Ublox NEO-M8P RTK	0.025 m + 1 ppm	-	-	8 Hz	300 USD
NovAtel OEM615	1.5 m	0.03 m/s	-	50 Hz	700 USD
NovAtel OEM615 RTK	0.01 m + 1 ppm	-	-	50 Hz	2000 USD

2.3.2 Sensors for Attitude Estimation

Most UAVs nowadays rely on inertial measurement units (IMUs) for inertial measurements and attitude estimation. A typical MEMS IMU consists 3-axis accelerometers, 3-axis rate gyros, and 3-axis magnetometers. Accelerometers are used to measure translational accelerations $[a_x, a_y, a_z]$, rate gyros are used to measure rotation rates $[p, q, r]$, magnetometers are used to measure the magnetic field mostly for heading ψ correction. Attitudes $[\phi, \theta, \psi]$ of UAVs are often estimated by combining multiple raw IMU measurements to compensate for sensor noises and drifts at an update rate of 50 - 100 Hz. It is typically done by integrating $[p, q, r]$ using Eq. (2.23) and combine with other measurements, such as accelerometers and magnetometers. Specifications of several widely used IMUs are shown in Table 2.2. Besides IMUs, there are vision-based systems to determine UAVs attitude [18].

Table 2.2: Comparison of IMUs

	Attitude Accuracy (Static: Typical)	Attitude Accuracy (Dynamic: Typical)	Update Rate	Approximate Cost
InvenSense MPU-9250 (Pixhawk Cube)	-	-	Logged at 25 Hz by Default	15 USD (200 USD)
VectorNav-100	±0.5 deg (Roll, Pitch) ±2 deg (Yaw)	±1 deg (Roll, Pitch) ±2 deg (Yaw)	400 Hz	800 USD
MicroStrain 3DM-GX3-35	±0.5 deg (Roll, Pitch, Yaw)	±2 deg (Roll, Pitch, Yaw)	1000 Hz	1000 USD
MicroStrain 3DM-GX4-25	±0.25 deg (Roll, Pitch) ±0.8 deg (Yaw)	±0.25 deg (Roll, Pitch) ±0.8 deg (Yaw)	500 Hz	1500 USD
Xsense MTi -200 VRU	±0.2 deg (Roll, Pitch)	±0.3 deg (Roll, Pitch)	2000 Hz	3000 USD

$$\begin{bmatrix} \dot{\phi} \\ \dot{\theta} \\ \dot{\psi} \end{bmatrix} = \begin{bmatrix} 1 & \sin\phi\tan\theta & \cos\phi\tan\theta \\ 0 & \cos\phi & -\sin\phi \\ 0 & \frac{\sin\phi}{\cos\theta} & \frac{\cos\phi}{\cos\theta} \end{bmatrix} \begin{bmatrix} p \\ q \\ r \end{bmatrix}. \tag{2.23}$$

2.3.3 Sensors for 3D Airspeed Measurements

3D airspeed vector $[u, v, w]$ or air triplets $[V, \alpha, \beta]$ describe the relative motion between UAVs and surrounding air. They are essential for wind/turbulence sensing and estimation. The airspeed V is generally measured by using a Pitot-tube with pressure sensors attached. AOA/α and AOS/β can be directly measured using air flow sensors, such as flow vanes or multi-hole Pitot-tubes. A flow vane, also known as a pivoted vane, is a mass-balanced wind vane that can align itself with the direction of the incoming air flow [19]. The angle between a flow vane and the reference line on the aircraft can then be measured by a potentiometer. Multi-hole Pitot-tubes can measure flow angles by sensing the pressure difference from different holes [19]. Specifications of several representative ADS are shown in Table 2.3. There also exist other direct measurement methods, such as distributed flush ADS [20], optical sensors [21], hot wire anemometer. Recently, sonic anemometers have been installed on UAVs for 3D wind speed measurements [22].

Table 2.3: Comparison of ADS

	Airspeed/Pressure Accuracy	AOA/AOS Accuracy	Update Rate	Approximate Cost
MPXV7002 (Analog)	100 Pascal	-	Analog	30 USD
Eagle Tree Airspeed MicroSensor V3	NA (Resolution: 0.45 m/s)	-	50 Hz	60 USD
US Digital MA3 Potentiometer	-	-	250 Hz	50 USD
STI22FS Potentiometer (Analog)	-	-	Analog	150 USD
Aeroprobe Micro ADS	1 m/s (Range: 8 m/s - 45 m/s)	$\pm$1 deg (Range: $\pm$20 deg)	100 Hz	5000 USD

2.3.4 Sensors to Measure UAVs' Dynamic Response to Wind

To study the interactions between UAVs and flow fields, especially UAVs' dynamic response, it is important to measure UAVs' inertial states $[a_x, a_y, a_z]$ and $[p, q, r]$. The inertial and air flow angle measurements of an aircraft are usually good indicators of turbulence encounters, which are essentially the output of the aircraft open or closed loop system in response to wind disturbance. To single out the dynamic response due to flow fields, it is important to remove dynamic response caused by control surface maneuvers by using identified aircraft dynamic models. Most of small UAVs utilize pulse width modulation (PWM) signals to control actuators. Those PWM signals are generally logged during the flight and can be mapped to control surface deflection angles after offline calibrations. For example, $[\delta_a, \delta_e, \delta_r]$ can be obtained by attaching potentiometers to the control linkages. δ_t can be calculated using logged PWM signals and identified engine thrust model.

2.4 Sensor Fusion Algorithms

In this section, filter algorithms that can be used to estimate wind fields for small fixed-wing UAVs are introduced. These algorithms can be divided into two broad categories, deterministic algorithms and statistical algorithms. Deterministic algorithms are usually more computationally efficient and easier to implement. However, they lack the ability to handle unknown noises and biases. Because small UAVs are often limited by budget and payload, statistical algorithms are

more often used for more accurate results.

2.4.1 Moving Average Filter

The moving average filter (MAF) calculates a series of averages of data subsections, as shown in Eq. (2.24), where $M(i)$ refers to the i^{th} measurement. It is very easy to implement a MAF and it requires minimal computation resources. However, it usually requires sensors to be accurate and calibrated properly. Averaging also means the loss of high frequency information, thus only good for prevailing/mean wind estimation. The same wind measurements shown in Fig. 2.2 are processed by a 20 seconds MAF and results are shown in Fig. 2.5. It can be seen that high frequency components are mostly filtered out.

$$M_{maf}(i) = \frac{\sum_{j=0}^{n-1} M(i+j)}{n}. \tag{2.24}$$

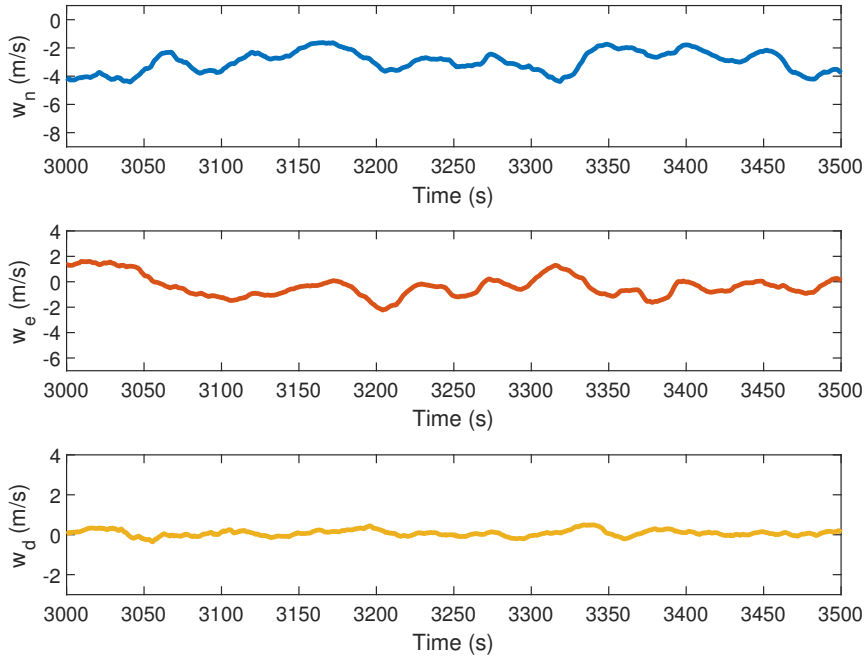

Figure 2.5: Ultrasonic wind anemometer measurements after 20 seconds MAF.

2.4.2 Complementary Filter

The idea behind the complementary filter (CF) is to combine signals coming out from two resources that are complementary to each other. One example is to combine the high frequency signal from one measurement M_1 and the low frequency signal from another measurement M_2, thus achieving a more accurate final estimate. A typical CF is formed by a high pass filter and a low pass filter, as shown in Eq. (2.25), where the second order filters are used. ζ_{cf} is the filter damping ratio and $\omega_{n_{cf}}$ is the break frequency of the CF. The CF is usually computational efficient and easy to implement.

$$M_{cf} = \underbrace{\frac{s^2}{s^2 + 2\zeta_{cf}\omega_{n_{cf}} + {\omega_{n_{cf}}}^2}}_{\text{High Pass Filter}} M_1 + \underbrace{\frac{2\zeta_{cf}\omega_{n_{cf}} s + {\omega_{n_{cf}}}^2}{s^2 + 2\zeta_{cf}\omega_{n_{cf}} s + {\omega_{n_{cf}}}^2}}_{\text{Low Pass Filter}} M_2. \tag{2.25}$$

2.4.3 Kalman Filter

The Kalman filter is the most commonly used stochastic filters for the navigation and estimation of UAVs. The Kalman filter runs recursively and consists two steps, the prediction step and the update step. It assumes process noises and measurement noises to be Gaussian. There are several types of Kalman filters, nonlinear Kalman filters are focused in this subsection as the UAV dynamics are usually nonlinear.

2.4.3.1 Extended Kalman Filter

EKF utilizes Taylor series to linearize nonlinear functions and then predict states. This subsection follows the EKF process described in [23]. The nonlinear discrete state space model is given by

$$\mathbf{x}_k = f(\mathbf{x}_{k-1}, \mathbf{u}_{k-1}, \mathbf{w}_{k-1}), \tag{2.26}$$

$$\mathbf{z}_k = h(\mathbf{x}_k, \mathbf{u}_k, \mathbf{v}_k), \tag{2.27}$$

where f is the non-linear state function, $\mathbf{w}_k$ and $\mathbf{v}_k$ are random variables that represent the process and measurement noise.

The EKF propagation equations are given as

$$\hat{\mathbf{x}}_k^- = f(\hat{\mathbf{x}}_{k-1}, \mathbf{u}_{k-1}, \mathbf{0}), \tag{2.28}$$

$$\mathbf{P}_k^- = \mathbf{A}_k \mathbf{P}_{k-1} \mathbf{A}_k^T + \mathbf{W}_k \mathbf{Q}_{k-1} \mathbf{W}_k^T, \tag{2.29}$$

where EKF measurement update equations are given as

$$\mathbf{K}_k = \mathbf{P}_k^- \mathbf{H}_k^T (\mathbf{H}_k \mathbf{P}_k^- \mathbf{H}_k^T + \mathbf{R}_k), \tag{2.30}$$

$$\hat{\mathbf{x}}_k = \hat{\mathbf{x}}_k^- + \mathbf{K}_k (\mathbf{z}_k - h(\hat{\mathbf{x}}_k^-, \mathbf{u}_k, \mathbf{0})), \tag{2.31}$$

$$\mathbf{P}_k = (\mathbf{I} - \mathbf{K}_k \mathbf{H}_k) \mathbf{P}_k^-. \tag{2.32}$$

$\mathbf{A}$, $\mathbf{W}$, and $\mathbf{H}$ are Jacobian matrices that can be calculated by

$$\mathbf{A}_{[i,j]} = \frac{\partial f_{[i]}}{\partial x_{[j]}} (\hat{\mathbf{x}}_{k-1}, \mathbf{u}_{k-1}, \mathbf{0}), \tag{2.33}$$

$$\mathbf{W}_{[i,j]} = \frac{\partial f_{[i]}}{\partial w_{[j]}} (\hat{\mathbf{x}}_{k-1}, \mathbf{u}_{k-1}, \mathbf{0}), \tag{2.34}$$

$$\mathbf{H}_{[i,j]} = \frac{\partial h_{[i]}}{\partial x_{[j]}} (\hat{\mathbf{x}}_k^-, \mathbf{u}_{k-1}, \mathbf{0}). \tag{2.35}$$

The EKF tuning process includes the tuning of initial covariance $\mathbf{P}_0$, process noise covariance $\mathbf{Q}$, and measurement noise covariance $\mathbf{R}$.

2.4.3.2 Unscented Kalman Filter

Similar to the EKF, the UKF is another type of nonlinear Kalman filter that is widely used. Instead of linearizing using Taylor series, the UKF takes use of nonlinear transformation of deterministic

sampling points (also known as sigma points) to represent underlying Gaussian distributions. It handles highly nonlinear systems better than the EKF, as the UKF does not require Taylor series approximation. The UKF also removes the need to calculate Jacobians which are often complex.

In the prediction step of the UKF, a set of sigma points is generated, as shown in Eqs. (2.36) - (2.38), where λ is the scaling parameter. These sigma points for $\mathbf{x}_{k-1}$ are then propagated by using the nonlinear function in Eq. (2.28). Then the predicted states $\mathbf{x}_k^-$ and covariance $\mathbf{P}_k^-$ are updated by weighting and summarizing all propagated sigma points, as shown in Eqs. $W_i^{(m)}$ and $W_i^{(c)}$ are weights. More details can be found in [24].

$$\hat{\mathbf{x}}_{k-1}^{(0)} = \hat{\mathbf{x}}_{k-1}, \tag{2.36}$$

$$\hat{\mathbf{x}}_{k-1}^{(i)} = \hat{\mathbf{x}}_{k-1} + \sqrt{n_{\mathbf{x}} + \lambda} \left[\sqrt{\mathbf{P}_{k-1}}\right]_i, i = 1, 2, \ldots, n_{\mathbf{x}}, \tag{2.37}$$

$$\hat{\mathbf{x}}_{k-1}^{(i+n_{\mathbf{x}})} = \hat{\mathbf{x}}_{k-1} - \sqrt{n_{\mathbf{x}} + \lambda} \left[\sqrt{\mathbf{P}_{k-1}}\right]_i, i = 1, 2, \ldots, n_{\mathbf{x}}, \tag{2.38}$$

$$\hat{\mathbf{x}}_k^- = \sum_{i=0}^{2n_{\mathbf{x}}} W_i^{(m)} \hat{\mathbf{x}}_k^{-(i)}, \tag{2.39}$$

$$\mathbf{P}_k^- = \sum_{i=0}^{2n_{\mathbf{x}}} W_i^{(c)} \left(\hat{\mathbf{x}}_k^{-(i)} - \hat{\mathbf{x}}_k^-\right) \times \left(\hat{\mathbf{x}}_k^{-(i)} - \hat{\mathbf{x}}_k^-\right)^T + \mathbf{Q}. \tag{2.40}$$

Similarly, the update step of the UKF requires sigma points of $\mathbf{x}_k$ to be generated using the same method as shown in Eqs. (2.36) - (2.38). These sigma points are then propagated through the non-linear equation h. The predicted measurements $h(\hat{\mathbf{x}}_k^-, \mathbf{u}_k, \mathbf{0})$ are again achieved by weighting and summarizing all propagated sigma points. Then the update step can be finished by using the same equations as those shown in the EKF, Eq. (2.30) - (2.32).

2.4.4 Particle Filter

Steps of a typical PF can be summarized as: draw samples/particles, propagate particles through non-linear system equations, assign and normalize particle weights, re-sample particles if necessary, and calculate estimates based on particles and their corresponding weights. Note that parti-

cles/samples need to be drawn from a known prior distribution (the importance distribution), which can be formed by using either the EKF or the UKF. The weight assigned to each particle is based on the prior distribution, posterior distribution, and the likelihood. Details for PF implementations can be found in [25].

Unlike Kalman filters where data are assumed to be Gaussian distributed, particle filters (PFs) can be used to approximate any non-linear system with any distribution. This gives the particle filters a clear advantage over Kalman filters for the UAV based 3D wind estimation problem as the UAV systems are highly nonlinear and the wind/turbulence is generally not Gaussian distributed. The disadvantage of the PF lies in its high computational cost. Although similar to the UKF in the idea of transforming samples through non-linear equations, the PF requires far more samples/particles as they are chosen randomly instead of deterministically sampled as in the UKF.

2.4.5 Other Algorithms

Other than the algorithms mentioned above, there are other algorithms that can be applied to the wind estimation problem, such as optimization based approach (for example, model predictive control) [26], fuzzy logic and data driven approach (for example, neural network and machine learning) [27].

2.5 Summaries of Existing Work and Recommendations

In this section, existing work for wind sensing and estimation using fixed-wing UAVs are summarized. General recommendations and considerations are provided to help determine which wind models, sensors, and algorithms are needed for future research related to wind sensing and estimation.

2.5.1 Summary of Existing Work

Existing work for wind sensing and estimation using fixed-wing UAVs are summarized in Table 2.4 with the main focus on those with flight validation results. Note that references shown in green are with simulation results only, while references shown in red have flight test results. In addition, in some references, results from multiple methods are presented.

Table 2.4: Existing work on wind sensing and estimation using small fixed-wing UAVs

	GPS	IMU + GPS	GPS + 1-D Pitot-Tube	IMU+GPS+ 1-D Pitot-Tube	IMU+GPS+ 1-D Pitot-Tube+ Mechanical Vanes	IMU+GPS+ Multi-Hole Pitot-Tube	IMU+GPS+ Sonic Anemometer	Other
Direct/MAF					3D prevailing [28]	2D prevailing [29–31] 3D prevailing [32] [33] PSD [34, 35]	2D prevailing [22]	
EKF		1st-Order RW: 2D prevailing [36] 3D prevailing	1st-Order RW: 2D prevailing [37] 3D prevailing [40]	1st-Order RW: 2D prevailing [30, 38] 3D prevailing [41] [28, 42] Thermal Model: Updraft estimation [44]	1st-Order RW: 3D prevailing [39]			1st-Order RW 2D prevailing Vision+1-D Pitot-tube [43]
UKF			1st-Order RW: 2D prevailing [45] 3D prevailing [45]		1st-Order RW: 3D prevailing [45, 46] 2nd-Order RW: 3D prevailing [47]			
PF						Thermal Model: Updraft estimation [48]		
Others	2D prevailing wind [30, 49, 50]							

It can be seen from the table that for 2D prevailing wind estimation, it is possible to use only IMU and GPS or even GPS by itself using optimization methods [49, 50]. However, UAVs are required to perform certain maneuvers, such as circling (roll/pitch/heading change), to make wind states observable. A standard setup for 2D prevailing wind estimation is GPS+1-D Pitot-tube [37] or IMU+GPS+1-D Pitot-tube [38]. For the problem of 3D wind sensing/estimation, most of the existing work requires direct measurements of air triplets either using a 1-D Pitot-tube and flow angle vanes or a multi-hole Pitot-tube [33]. However, if certain assumptions regarding AOA and AOS are made [28] or partial UAV aerodynamic model is available [42], it is possible to estimate 3D wind with the set up of IMU, GPS, and a 1-D Pitot-tube. For meteorological applications,

most researchers used direct calculation methods and are interested in vertical wind profile and the PSD of wind field. On the other side, in flight dynamics and control applications, most researchers used stochastic filters for mean wind estimation, with few applications using direct flow angle measurements (aircraft wake encounters). The reason is that most of the small UAVs nowadays are already equipped with GPS and IMU since they are cheap, light weight, and widely available, but very few UAVs are equipped with a high fidelity ADS. It is also observed that another major challenge comes from the validation part, since it is difficult to find a ground truth of the spatio-temporal wind information during flight tests. A common way of validation is by comparing UAV wind estimation results with measurements from other wind measurement instruments such as ground wind anemometer, radiosonde, SODAR, or LiDAR. Among these instruments, ground wind anemometers are the most widely used one, as they are relatively cheaper and easier to deploy. However, the major drawback is that they are often not at the same locations as UAVs. Therefore, measurements from weather stations need to be interpolated or extrapolated using certain wind profile models for direct comparisons.

Since a great portion of wind sensing and estimation related work is Kalman filter based, several representative Kalman filter formulations are shown below.

2.5.1.1 Representative 2D Prevailing Wind Estimation Filter

Cho presented a simple extended Kalman filter (EKF) for the estimation of 2D horizontal wind using only a conventional Pitot-tube and a GPS receiver [37]. The EKF states, inputs, and measurements are shown in Eq. (2.41), where V_{w} is the wind speed, ψ_{w} is the wind direction, sf is the scaling factor for the pressure sensor, and p_d is the dynamic pressure. The wind triangle equation for this formulation is given by Eq. (2.42), where ψ_g is UAV heading calculated from GPS. Cho's filter is one of the simplest horizontal wind estimation filter for UAVs. It requires certain UAV maneuvers including circling or figure 8 to meet the observability requirements.

$$\mathbf{x} = [V_{\mathrm{w}} \;\; \psi_{\mathrm{w}} \;\; sf]^T, \tag{2.41a}$$

$$\mathbf{u} = [V_g \;\; \psi_g]^T, \tag{2.41b}$$

$$\mathbf{z} = [p_d]^T, \tag{2.41c}$$

$$V_g{}^2 + V_{\mathrm{w}}{}^2 - 2V_g V_{\mathrm{w}} \cos(\psi_{\mathrm{w}} - \psi_g) = V_a^2 = \frac{p_d}{sf}. \tag{2.42}$$

2.5.1.2 Representative 3D Prevailing Wind Estimation Filter with Direct Flow Angle Measurements

Rhudy developed an UKF that could estimate aircraft attitude and 3D wind simultaneously using measurements from IMU, GPS, airspeed sensor, and flow angle vanes [45]. The UKF states, inputs, and measurements are shown in Eq. (2.43). These states are propagated using Eq. (2.7), Eq. (2.23), and Eq. (2.4). The measurement equations are Eq. (2.1) and Eq. (2.3). Rhudy's filter combines conventional inertial, GPS, and flow angle measurements for accurate estimates of 3D wind. However, it may be difficult to install or maintain flow angle vanes on UAVs, especially flying wings.

$$\mathbf{x} = [u \;\; v \;\; w \;\; \phi \;\; \theta \;\; \psi \;\; \mathbf{w}_n \;\; \mathbf{w}_e \;\; \mathbf{w}_d]^T, \tag{2.43a}$$

$$\mathbf{u} = [a_x \;\; a_y \;\; a_z \;\; p \;\; q \;\; r]^T, \tag{2.43b}$$

$$\mathbf{z} = [V_n \;\; V_e \;\; V_d \;\; V_{pitot} \;\; \alpha \;\; \beta]^T. \tag{2.43c}$$

2.5.1.3 Representative 3D Prevailing Wind Estimation Filter without Direct Flow Angle Measurements

To estimate 3D wind without direct flow angle measurements, certain assumptions regarding AOA and AOS have to be made. The assumptions can be either model free [28], or model aided [42]. The approach in [42] is based on an EKF, where the filter states, inputs, are the same with those shown in Eq. (2.43a) and Eq. (2.43b). However, the major difference between [45] and [42] is that instead of relying on direct flow angle measurements for update, [42] takes the model aided approach by correlating lift equations and side force equations. Details regarding filter formulations of [42] are

shown in Chapter 5.

There are also other formulations to solve the wind triangle equation. For example, wind estimation can be coupled with UAV navigation states to form a tightly coupled EKF [39]. In addition, some states or measurements can be derived instead of directly measured if UAV dynamics models are known [36]. Other states to consider in filter formulations include sensor biases and sensor alignment errors.

2.5.2 Recommendations for Wind Model, Sensor, and Algorithm

The two most important factors to consider for UAV based wind sensing and estimation are the application scenario and budget, which can help determine what platform, wind models, and sensors to use. Consequently, those selected wind models and sensors will help determine the type of estimation filters. For example, for thermal soaring missions, it is straightforward to use a glider equipped with GPS, IMU, and ADS. If resources are available, a full ADS with accurate AOA and AOS measurements can be used, with the help from certain vertical wind estimation algorithms. If the budget or payload is limited, a low cost system with the conventional Pitot-tube can be selected instead. The first order RW model and the thermal model can be used to represent wind dynamics in an EKF or UKF sensor fusion framework. In summary, it is important to find a balance between hardware/sensors and software/algorithms as well as between cost and performance accuracy.

General considerations and recommendations regarding wind model, sensor, and algorithm selection are listed as follows.

For the selection of wind models, it is crucial to identify the dominant wind component to be measured or estimated. For general UAV wind sensing and estimation problems, a combination of several wind models including prevailing wind, turbulence, and wind shear may yield the best results.

For the selection of sensors, the following major points need to be considered:

1. Sensor type and budget: The major wind impact sensor needs to be carefully selected for a UAV based on the application focus and budget. For instance, a high quality airflow angle

sensor such as a multi-hole probe is usually selected for many meteorological turbulence measurement scenarios [34, 35], while a high fidelity IMU is more important for gust alleviation control application;

2. Size and weight: UAVs, especially small UAVs are often limited by their space and weight. Small and light sensors with low power consumption are usually preferred for small UAVs due to installation challenges;

3. Update rate: Sensor and filter update rate needs to be carefully evaluated based on frequencies of interest for the targeted wind field. For example, sensors with a high update rate (50 - 100 Hz or higher) need to be selected for applications on high frequency turbulence;

4. Estimation accuracy: Although delicately designed algorithms/filters can improve the estimation accuracy, it is essentially limited by the accuracy of sensors used in the algorithm;

5. Noise level: Filters are often required for low cost sensors with a high random noise level. The high noise to signal ratio will make it difficult for the signal reconstruction;

6. Location of installation: Locations of certain sensors are critical to later modeling and control efforts. For example, the location and orientation alignment of an IMU is critical to the wind speed transformation from the body frame to the inertial frame as well as to the aircraft system identification and flight control. Another good example is the ADS, where the Pitot-tube should be installed far enough from the fuselage to stay away from the structure generated disturbance. The location of flow angle vanes also have a big impact on the sensor calibration and turbulence detection such as wake vortices [51].

For the selection of wind estimation algorithms, the following questions need to be answered:

1. Can you afford a suite of high fidelity airflow sensors for your UAV both budget wise and payload wise? If yes, get the most accurate and reliable sensors with the highest update rate within your budget; Otherwise, aerodynamic model-aided filters [36, 42] or optimization approaches [52] can be used to compensate for the missing of direct measurements;

2. How is your sensor quality and calibration? Are your sensor noises/biases/alignment errors small? If yes, deterministic algorithms such as MAF or CF can be used; Otherwise, statistical algorithms will be helpful;

3. What is your computational power constraint? CFs and EKFs are generally considered computationally efficient while UKFs, PFs, and optimization based approaches are rather computationally intensive for most UAVs' onboard microprocessors;

4. Are you planning to reuse an existing estimation framework? If yes, cascaded filter structure can be utilized [36, 38, 41]; Otherwise, a tightly coupled filter structure can be implemented [39];

5. How is the observability of the developed filter/algorithm? Certain flight maneuvers maybe required for filter convergence [50, 53];

6. Are you interested in both wind speed estimation and wind field estimation? If yes, parameters in the wind field model can be implemented as states in the filter/algorithm to be estimated [54–56].

2.6 Conclusions

This chapter presents a thorough survey of existing methods on wind sensing and estimation using small fixed-wing UAVs. Representative wind models are first introduced for the wind sensing and estimation problem. Available UAV sensors are then summarized and compared, with the focus on UAV dynamic responses to wind and turbulence. Representative statistical filter types and formulations are discussed and compared in detail with recommendations for future research directions.

Chapter 3

Design and Evaluation of UAV Flow Angle Estimation Filters

Abstract

This chapter presents the design, implementation, and evaluation of four filters for the estimation of angle of attack (AOA) and angle of sideslip (AOS) of small unmanned aerial vehicles (UAVs). Specifically, two novel filters (a complementary filter and an extended Kalman filter) are proposed and evaluated without using direct flow angle and GPS measurements; two existing AOA/AOS filters are also implemented and evaluated. All filters are designed with minimal inputs and states to ensure the ease of implementation, simplicity of tuning, and computation efficiency. Both simulation and UAV flight test results show the performance of the proposed filters. Especially, flight test results from two different UAVs (a T-tail UAV and a flying wing UAV) show that the root mean square errors of estimated inertial AOA and AOS are less than 1.5 degrees under nominal flight conditions and around 2 degrees under aggressive maneuvers compared with direct flow angle measurements.

3.1 Introduction

Angle of attack (AOA) and angle of sideslip (AOS) (also known as flow angles) describe the interaction between flight vehicles and the surrounding air, which have significant influences on aircraft aerodynamics [57]. Accurate AOA and AOS measurements/estimation are crucial to aircraft model identification and flight control [52, 58]. More importantly, AOA and AOS are flight critical. Pilots rely on AOA for stall warning and for indications of surrounding air flows in order to fly the aircraft efficiently and safely [59, 60]. The malfunction of AOA and AOS sensors could cause severe

consequences such as loss of control and catastrophic accidents [61]. Therefore, the redundancy of these signals is usually required for manned aircraft [62]. AOA and AOS measurements are also well accepted as good indicators for turbulence encounters, especially for wake vortex encounters [51, 63]. Recently, AOA and AOS are used for the estimation of 3D wind velocities along the aircraft flight trajectory [45]. For most manned aircraft, AOA and AOS are measured using air flow vanes or multi-hole pressure probes [19]. These sensors are usually mounted ahead of the fuselage nose, ahead of the wing tip, or on the fuselage forebody [64]. It is worth emphasizing that AOA and AOS sensors need to be careful installed and calibrated in order to reduce the influence on local air flows due to the presence of a Pitot-tube and fuselage [19, 65]. It requires extensive efforts and high costs to achieve desired accuracy, which is often difficult for low-cost small unmanned aerial vehicles (UAVs) [66].

In consideration of redundancy, reliability, accuracy, and cost requirements, different filtering techniques have been proposed for the estimation or reconstruction of AOA and AOS with or without direct flow angle measurements. Based on the sensors used in the filter, these methods fall into two major categories. The first category is to use filters to increase the reliability and accuracy of direct AOA and AOS measurements by removing measurement noises and local flow disturbances [46, 67, 68]. The second category works without direct flow angle measurements, which can be used either as a redundant/complementary system or as a standalone system. Filters belonging to this category are referred to as inertial AOA/AOS estimation filters [36, 38, 40, 41, 52, 62, 66, 69–75]. When direct flow angle measurements are available, filters in the first category are more frequently used for signal quality improvement. An extended Kalman Filter (EKF) is proposed in [46], where the quality of direct flow angle measurements from mechanical vanes is improved with the help from Global Positioning System (GPS) and inertial measurement unit (IMU) data. Besides Kalman filters, complementary filters (CFs) can also be used to filter out noises and local flow disturbances from direct flow angle measurements [67, 68].

For the second category, without direct flow angle measurements, inertial AOA and AOS can be estimated mainly based on inertial measurements of aircraft dynamic responses to the surrounding

flow. Inertial AOA and AOS can be calculated by integrating inertial data over time, however, the direct integration method usually suffers from nontrivial biases and drifts [66]. To solve this problem, different filtering techniques can be applied, including CFs [73, 76] and Kalman filters [36, 38, 40, 41, 62, 69–72, 74, 75]. Among these methods, [38, 41, 74] are able to estimate flow angles without relying on aircraft aerodynamic models by correlating airspeed measurements with GPS ground speed measurements using wind triangle equations. When airspeed measurements and partial aircraft aerodynamic model parameters are available, flow angles can be estimated without GPS measurements [62, 69–72, 76]. For cases when the more sophisticated aircraft model is available, even airspeed measurements are not required [36]. From aforementioned literature, it can be observed that studies on flow angle estimation often have strong correlations with wind estimation problems [36–38, 40, 41, 45, 46, 70, 73, 76]. There are also several other approaches for inertial flow angle estimation. A frequency domain system identification method is proposed in [66], where flow angles are first reconstructed in the time domain and then transformed into frequency domain to eliminate integration biases and drifts. An alternative method to assist aircraft system identification is called flight path reconstruction (FPR). For this technique, AOA and AOS are reconstructed by integrating inertial data using an output error minimization method [52]. It is also possible to estimate inertial AOA and AOS by using algorithms such as the Newton-Raphson solver [75]. However, these optimization methods are not suitable for real time applications due to their high demands on computational power.

In summary, most of the existing methods for flow angle estimation either require direct flow angle sensors, GPS measurements, or sophisticated aircraft dynamic models, which can be difficult for small UAV applications. These difficulties and logistic challenges led to few flight test validation results on UAVs. This chapter is focused on increasing the redundancy and reliability as well as reducing the cost of flow angle systems. It is a significant extension of our previous work [77], where only the filters that require direct flow angle measurements are implemented and tested on one UAV platform (Phastball). In this chapter, four AOA and AOS estimation filters are designed, implemented, and evaluated on two UAV platforms (Phastball and KHawk 55”), includ-

ing two new filters (1 EKF and 1 CF) for inertial flow angle estimation without using direct flow angle measurements and two existing filters (1 EKF and 1 CF [77]) for noise removal of direct flow angle measurements. All filters are formed with minimal inputs and states to ensure the ease of implementation, simplicity of tuning, and computational efficiency. Especially, the proposed inertial flow angle estimation filters can work as an independent and redundant unit on small UAVs to improve UAV safety and flight performance as well as facilitate studies on wind estimation and turbulence sensing. In addition, GPS measurements are not required for filters designed in this chapter, which is convenient for small UAVs that operate under GPS degraded or denied environments. The major contributions of this chapter can be summarized as follows:

1. To reduce the dependency in direct flow measurement systems, two novel filters (a CF and an EKF based designs) are proposed and evaluated on a T-tail UAV (Phastball) and a flying wing UAV (KHawk 55"), where inertial AOA and AOS are estimated without using direct flow angle measurements and GPS measurements;
2. Flight test evaluation of all four filters are conducted on two different UAV platforms under nominal flight conditions and aggressive maneuvers. Filter formulation and tuning procedures are discussed and compared in detail.

The organization of this chapter can be summarized as follows. The problem of AOA and AOS estimation is formulated in Sec. 3.2. Then, four fusion algorithms are introduced in detail in Sec. 3.3. Simulation and flight test results are presented in Sec. 3.4 and Sec. 3.5, respectively. Finally, conclusions are made in Sec. 3.6.

3.2 Problem Formulation

Angle of attack (AOA or α) is defined as the angle between a reference line on the aircraft and the flight direction [78], shown in Fig. 3.1, where V is the airspeed and $[u, v, w]$ are airspeed projections in aircraft body-axis. The reference line is usually chosen as the chord line of an airfoil [78] and an AOA relative to this line is called the geometric angle of attack [79]. Similarly, sideslip angle

(AOS or β) is defined as the angle between the x-z plane in the body frame of the aircraft and the incoming flow [80].

AOA and AOS can be directly measured using air flow sensors installed on an aircraft. Typical air flow sensors are flow vanes and multi-hole Pitot-tubes. A flow vane, also known as a pivoted vane, is a mass-balanced wind vane that can align itself with the direction of the incoming air flow [19]. The angle between a flow vane and the reference line on the aircraft can then be measured by a potentiometer. Multi-hole Pitot-tubes can measure flow angles by sensing the pressure difference from different holes [19]. There also exist other direct measurement methods. Differential pressure probes can be used to measure AOA when calibration and normalization is properly done [81]. Distributed flush air data systems are another solution [20]. It is also possible to measure flow angles by using optical sensors [21]. It is worth mentioning that direct flow measurements are usually corrupted by noises.

AOA and AOS can also be estimated, or reconstructed using measurements mainly from inertial sensors, which are called inertial AOA and AOS. A typical method for inertial AOA and AOS reconstruction is to combine measurements from the Pitot-tube (V_{pitot}), accelerometers (a_x, a_y, a_z), and gyroscopes (p, q, r). Inertial AOA/AOS and measured AOA/AOS usually match with each other in a calm atmosphere. However, they may show non-trivial difference in dynamic flow fields due to effects caused by local turbulence [63, 82].

This chapter exploits the AOA/AOS measurement and estimation methods. Two types of filters are designed, implemented, and evaluated for AOA/AOS estimation. Direct AOA/AOS measurements from mechanical vanes or a multi-hole Pitot-tube are used as the ground truth for validation purpose. Based on sensor and aircraft model availability, filters studied in this chapter can be categorized into two types:

1. For aircraft with low quality AOA/AOS sensors such as custom-made flow vanes, a CF and an EKF are developed for the noise rejection with the help of inertial measurements and Pitot-tube measured airspeed;
2. For aircraft without direct flow angle sensors, a simple model aided CF and a simple model

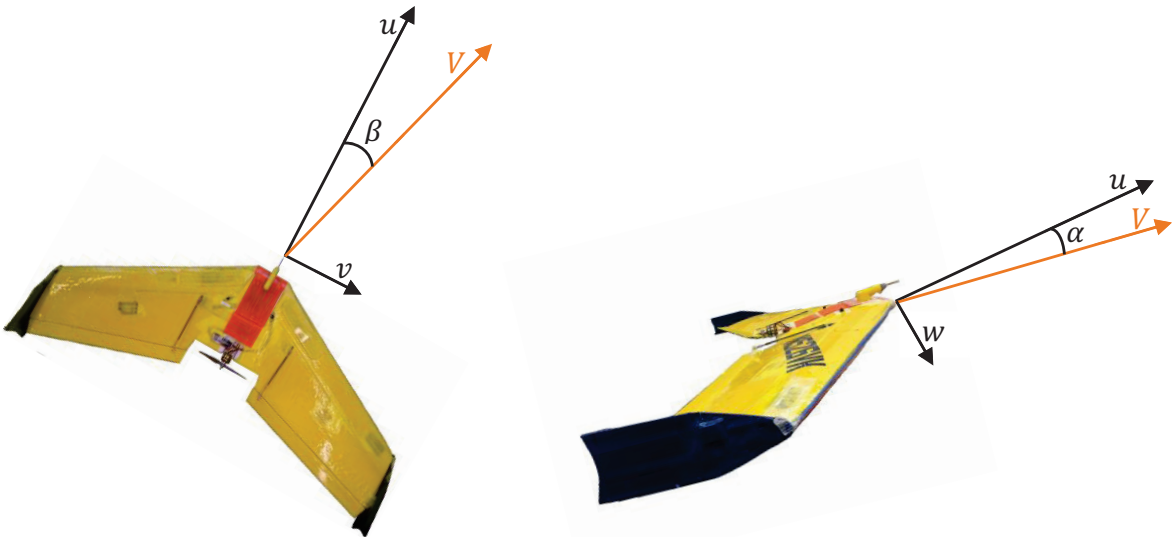

Figure 3.1: Definition of AOA and AOS.

aided EKF are designed for inertial AOA/AOS estimation with the help of inertial measurements, Pitot-tube measured airspeed, and pre-identified aircraft lift and side force coefficients.

3.3 Sensor Fusion Algorithms

In this section, algorithms used for AOA and AOS estimation are presented. To ensure the ease of implementation, simplicity of tuning, and computational efficiency, all filters are designed in the most compact form for the estimation of both AOA and AOS.

3.3.1 Extended Kalman Filter for AOA and AOS Estimation

EKF is one of the most commonly used algorithms for combining measurements from multiple noisy sensors [83, 84]. Given corrupted measurements from GPS (optional), IMU, and flow sensors, one approach is to estimate the body-frame velocity components (u, v, w) first and then calculate AOA and AOS based on the estimated velocity components. The other approach is directly using AOA and AOS (α, β) as EKF states. In this chapter, both EKF formulations are implemented and evaluated.

3.3.1.1 EKF: Filtering of Direct Flow Angle Measurements

This filter was proposed in our former work [77], which can filter direct AOA/AOS measurements without relying on GPS measurements. In this approach, IMU measurements $[a_x, a_y, a_z, p, q, r]$, airspeed measurement $[V_{pitot}]$, flow vane measurements $[\alpha_m, \beta_m]$, and aircraft attitude $[\phi, \theta]$ are assumed to be available. $[u, v, w]$ are used as systems states for the EKF. The propagation equation of this EKF is derived from equations of translational motion of an aircraft [52],

$$\begin{bmatrix} \dot{u} \\ \dot{v} \\ \dot{w} \end{bmatrix} = \begin{bmatrix} -qw + rv - g\sin\theta + a_x \\ -ru + pw + g\cos\theta\sin\phi + a_y \\ -pv + qu + g\cos\theta\cos\phi + a_z \end{bmatrix}. \tag{3.1}$$

The update equation is given by the relation between $[u, v, w]$ and $[V, \alpha, \beta]$ as follows

$$\begin{bmatrix} V \\ \alpha \\ \beta \end{bmatrix} = \begin{bmatrix} \sqrt{u^2 + v^2 + w^2} \\ \tan^{-1}(\frac{w}{u}) \\ \sin^{-1}(\frac{v}{V}) \end{bmatrix}. \tag{3.2}$$

The noises are considered for both the system inputs and observations. For such a model, the state **x**, input **u**, non-linear measurement function **h**, and measurement **z** vectors are given by

$$\mathbf{x} = [u \;\; v \;\; w]^T, \tag{3.3a}$$

$$\mathbf{u} = [a_x \;\; a_y \;\; a_z \;\; p \;\; q \;\; r \;\; \phi \;\; \theta]^T, \tag{3.3b}$$

$$\mathbf{h}(\mathbf{x}, \mathbf{u}, \mathbf{0}) = [\sqrt{u^2 + v^2 + w^2} \;\; \tan^{-1}(\frac{w}{u}) \;\; \sin^{-1}(\frac{v}{V})]^T, \tag{3.3c}$$

$$\mathbf{z} = \mathbf{h}(\mathbf{x}, \mathbf{u}, \mathbf{v}) = [V_m \;\; \alpha_m \;\; \beta_m]^T, \tag{3.3d}$$

where m denotes measured data and **v** is the measurement noise vector.

3.3.1.2 EKF: Inertial AOA/AOS Estimation

In this approach, IMU measurements $[a_x, a_y, a_z, p, q, r]$, airspeed measurement $[V_{pitot}]$, aircraft attitude $[\phi, \theta]$, control surface deflections $[\delta_e, \delta_a, \delta_r]$, aircraft lift coefficients $[C_{L_0}, C_{L_\alpha}, C_{L_q}, C_{L_{\delta_e}}]$, and side force coefficients $[C_{Y_0}, C_{Y_\beta}, C_{Y_p}, C_{Y_r}, C_{Y_{\delta_a}}, C_{Y_{\delta_r}}]$ are assumed to be available. $[\alpha, \beta]$ are used as systems states for the EKF. The propagation equations of this EKF, shown in Eqs. (3.4) and (3.5), are derived by differentiating Eqs. (3.2) and substituting Eqs. (3.1).

$$\dot{\alpha} = q + \frac{g(\cos\phi\cos\theta\cos\alpha + \sin\theta\sin\alpha) - a_x\sin\alpha + a_z\cos\alpha}{V\cos\beta} - (p\cos\alpha + r\sin\alpha)\tan\beta, \quad (3.4)$$

$$\dot{\beta} = \frac{1}{V}[-a_x\cos\alpha\sin\beta + a_y\cos\beta - a_z\sin\alpha\sin\beta + g(\sin\theta\cos\alpha\sin\beta + \cos\theta\sin\phi\cos\beta - \cos\theta\cos\phi\sin\alpha\sin\beta)] + p\sin\alpha - r\cos\alpha. \quad (3.5)$$

The update equations are shown in Eqs. (3.6) and (3.7), which can be derived from aircraft lift and side force equations. Detailed derivations can be found in Eqs. (3.8)-(3.10).

$$C_{L_0} + \frac{C_{L_q}q\bar{c}}{2V} + C_{L_{\delta_e}}\delta_e = \frac{m(a_x\sin\alpha - a_z\cos\alpha)}{\bar{q}S} - C_{L_\alpha}\alpha, \quad (3.6)$$

$$\frac{1}{C_{Y_\beta}}(\frac{ma_y}{\bar{q}S} - C_{Y_0} - \frac{C_{Y_p}pb}{2V} - \frac{C_{Y_r}rb}{2V} - C_{Y_{\delta_a}}\delta_a - C_{Y_{\delta_r}}\delta_r) = \beta, \quad (3.7)$$

where b is the wingspan, $\bar{c}$ is the mean chord length, S is the wing area, and $\bar{q}$ is the dynamic pressure.

According to the aircraft force equation, lift can be expressed as the projection of thrust and body-axis accelerations. Note that the thrust projection is much smaller than the lift during normal flight conditions, therefore, it can be removed for simplification.

$$L = m(a_x\sin\alpha - a_z\cos\alpha) - T\sin\alpha \approx m(a_x\sin\alpha - a_z\cos\alpha). \quad (3.8)$$

Lift can also be approximated as

$$L = C_L \bar{q} S \approx (C_{L_0} + C_{L_\alpha}\alpha + C_{L_{\delta_e}}\delta_e + C_{L_q} q\bar{c}/(2V))\bar{q}S. \tag{3.9}$$

By substituting lift from Eq. (3.9) in Eq. (3.8) and moving terms that contain α to the right side of equation, Eq. (3.6) is derived.

Similarly, Eq. (3.7) can be derived by correlating side force equations, shown in Eq. (3.10), and moving terms that contain β to the right side of equation.

$$Y = ma_y = C_Y \bar{q} S \approx (C_{Y_0} + C_{Y_\beta}\beta + \frac{C_{Y_p} pb}{2V} + \frac{C_{Y_r} rb}{2V} + C_{Y_{\delta_a}}\delta_a + C_{Y_{\delta_r}}\delta_r)\bar{q}S. \tag{3.10}$$

The main philosophy behind the update equations is that the lift and side forces of the aircraft can be estimated from the accelerometer readings, and the long-term error is quite small around the trim point during steady state wings-level flight.

The state **x**, input **u**, non-linear measurement function **h**, and measurement **z** vectors for this filter are given by

$$\mathbf{x} = [\alpha \;\; \beta]^T, \tag{3.11a}$$

$$\mathbf{u} = [a_x \;\; a_y \;\; a_z \;\; p \;\; q \;\; r \;\; \phi \;\; \theta \;\; V]^T, \tag{3.11b}$$

$$\mathbf{h}(\mathbf{x}, \mathbf{u}, \mathbf{0}) \;\; = \;\; \begin{bmatrix} m(a_x \sin\alpha - a_z \cos\alpha)/(\bar{q}S) - C_{L_\alpha}\alpha \\ \beta \end{bmatrix}, \tag{3.11c}$$

$$\mathbf{z} = \mathbf{h}(\mathbf{x}, \mathbf{u}, \mathbf{v}) \;\; = \;\; \begin{bmatrix} C_{L_0} + \frac{C_{L_q} q\bar{c}}{2V} + C_{L_{\delta_e}}\delta_e \\ \frac{1}{C_{Y_\beta}}(\frac{ma_y}{\bar{q}S} - C_{Y_0} - \frac{C_{Y_p} pb}{2V} - \frac{C_{Y_r} rb}{2V} - C_{Y_{\delta_a}}\delta_a - C_{Y_{\delta_r}}\delta_r) \end{bmatrix}. \tag{3.11d}$$

This chapter follows the EKF process described in Chapter 2 Sec. 2.4.3.1. The EKF tuning process is discussed in Sec. 3.5, which includes the selection of initial covariance $\mathbf{P}_0$, process

noise covariance **Q**, and measurement noise covariance **R**.

3.3.2 Complementary Filter for AOA and AOS Estimation

The complementary filter is another approach to reconstruct AOA and AOS. The CF generally consists of two parts, a second-order low pass filter and a second-order high pass filter, which can increase the system's bandwidth.

3.3.2.1 CF: Filtering of Direct Flow Angle Measurements

This filter was mainly used on manned aircraft to filter out the noise from flow vane or conventional probe measurements [67, 68]. In this approach, IMU measurements $[a_x, a_y, a_z, p, q, r]$, airspeed measurement $[V_{pitot}]$, flow vane measurements $[\alpha_m, \beta_m]$, and aircraft attitude $[\phi, \theta]$ are assumed to be available.

AOA and AOS can be reconstructed by the combinations of the high-frequency portions of $\dot{\alpha}/\dot{\beta}$ and the low-frequency portions of flow vane measurements α_m/β_m, shown in Eqs. (3.12) and (3.13) [67, 68]

$$\alpha_{cf\_filtered} = \underbrace{\frac{s}{s^2 + 2\zeta_{cf}\omega_{n_{cf}}s + {\omega_{n_{cf}}}^2}\dot{\alpha}}_{\text{High Frequency Contribution}} + \underbrace{\frac{2\zeta_{cf}\omega_{n_{cf}}s + {\omega_{n_{cf}}}^2}{s^2 + 2\zeta_{cf}\omega_{n_{cf}}s + {\omega_{n_{cf}}}^2}\alpha_m}_{\text{Low Frequency Contribution}}, \tag{3.12}$$

$$\beta_{cf\_filtered} = \underbrace{\frac{s}{s^2 + 2\zeta_{cf}\omega_{n_{cf}}s + {\omega_{n_{cf}}}^2}\dot{\beta}}_{\text{High Frequency Contribution}} + \underbrace{\frac{2\zeta_{cf}\omega_{n_{cf}}s + {\omega_{n_{cf}}}^2}{s^2 + 2\zeta_{cf}\omega_{n_{cf}}s + {\omega_{n_{cf}}}^2}\beta_m}_{\text{Low Frequency Contribution}}, \tag{3.13}$$

where ζ_{cf} is the filter damping ratio and $\omega_{n_{cf}}$ is the break frequency of the complementary filter. $\dot{\alpha}$ and $\dot{\beta}$ are calculated from Eqs. (3.4) and (3.5). α_m and β_m are measurements from mechanical vanes which usually contain high frequency noise.

3.3.2.2 CF: Inertial AOA/AOS Estimation

This filter is similar to [73], however, given the fact that the low-cost GPS receivers on most UAVs cannot provide accurate flight path angle under dynamic maneuvers, alternative measurements and equations are used. In this approach, IMU measurements $[a_x, a_y, a_z, p, q, r]$, airspeed measurement $[V_{pitot}]$, aircraft attitude $[\alpha, \beta]$, control surface deflections $[\delta_e, \delta_a, \delta_r]$, aircraft lift coefficients $[C_{L_0}, C_{L_\alpha}, C_{L_q}, C_{L_{\delta_e}}]$, and side force coefficients $[C_{Y_0}, C_{Y_\beta}, C_{Y_p}, C_{Y_r}, C_{Y_{\delta_a}}, C_{Y_{\delta_r}}]$ are assumed to be available.

Reconstructed AOA and AOS can be calculated by Eqs. (3.14) and (3.15).

$$\alpha_{cf\_inertial} = \underbrace{\frac{s}{s^2 + 2\zeta_{cf}\omega_{n_{cf}}s + {\omega_{n_{cf}}}^2}\dot{\alpha}}_{\text{High Frequency Contribution}} + \underbrace{\frac{2\zeta_{cf}\omega_{n_{cf}}s + {\omega_{n_{cf}}}^2}{s^2 + 2\zeta_{cf}\omega_{n_{cf}}s + {\omega_{n_{cf}}}^2}\alpha_{long}}_{\text{Low Frequency Contribution}}, \tag{3.14}$$

$$\beta_{cf\_inertial} = \underbrace{\frac{s}{s^2 + 2\zeta_{cf}\omega_{n_{cf}}s + {\omega_{n_{cf}}}^2}\dot{\beta}}_{\text{High Frequency Contribution}} + \underbrace{\frac{2\zeta_{cf}\omega_{n_{cf}}s + {\omega_{n_{cf}}}^2}{s^2 + 2\zeta_{cf}\omega_{n_{cf}}s + {\omega_{n_{cf}}}^2}\beta_{long}}_{\text{Low Frequency Contribution}}. \tag{3.15}$$

$\dot{\alpha}$ and $\dot{\beta}$ are calculated by using Eqs. (3.4) and (3.5). α_{long} and β_{long} are calculated based from Eqs. (3.6) and (3.7) by moving α and β to the left side of equation, shown in Eqs. (3.16) and (3.17).

$$\alpha_{long} = \frac{m(a_x \sin\alpha - a_z \cos\alpha)/(\bar{q}S) - C_{L_0} - C_{L_q} q\bar{c}/(2V) - C_{L_{\delta_e}}\delta_e}{C_{L_\alpha}}, \tag{3.16}$$

$$\beta_{long} = \frac{1}{C_{Y_\beta}}\left(\frac{ma_y}{\bar{q}S} - C_{Y_0} - \frac{C_{Y_p}pb}{2V} - \frac{C_{Y_r}rb}{2V} - C_{Y_{\delta_a}}\delta_a - C_{Y_{\delta_r}}\delta_r\right). \tag{3.17}$$

The AOA and AOS reconstructed from this complementary filter are combinations of the high-frequency portions of $\dot{\alpha}/\dot{\beta}$ and the low-frequency portions of $\alpha_{long}/\beta_{long}$. Note that in implementation the α on the right side of Eq. (3.16) is approximated by $\alpha_{cf\_inertial}$ estimated from the previous time step.

3.4 Simulation Results

Simulation results are focused in this section for the validation of fusion algorithms described in Section 3.3. The WVU Phastball UAV simulator was used, which is based on MATLAB Flight Dynamics and Control (FDC) toolbox. More details can be found in [85].

During the simulation, elevator and aileron doublet inputs were used to excite changes in α and β. The input commands and aircraft states are shown in Fig. 3.2. Gaussian noises were added to measured aircraft states based on noise characteristics from real sensors [86]. It can be observed from Fig. 3.2 that there is an elevator doublet at around 10 seconds and an aileron doublet at around 12 seconds. AOA and AOS induced by doublet maneuvers are shown in Fig. 3.3 and Fig. 3.4, including noisy measurements, ground truth, and estimation results.

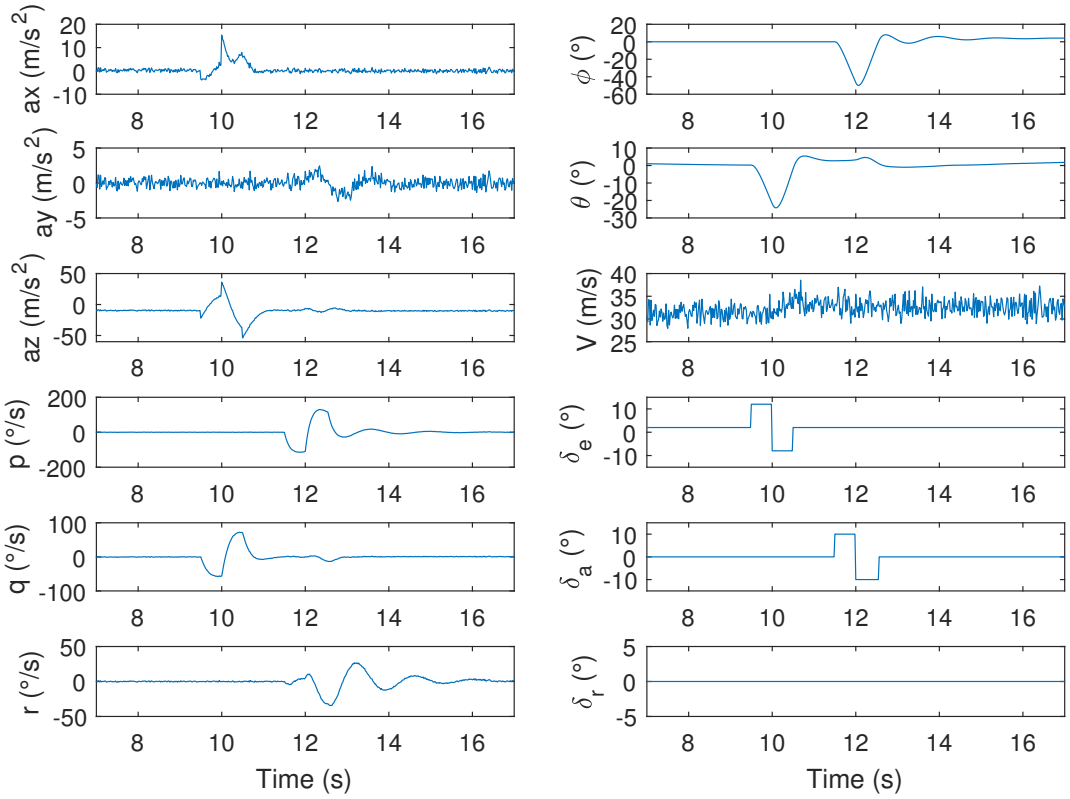

Figure 3.2: Aircraft states during doublet maneuvers.

The means and standard deviations of the absolute estimation errors using different algorithms

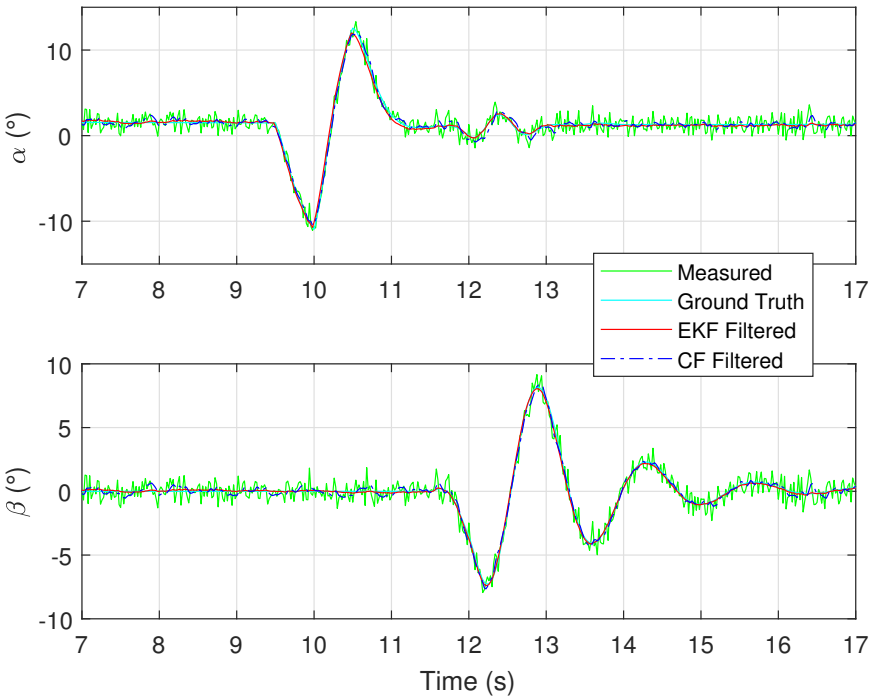

Figure 3.3: Filtered α/β vs. ground truth during doublet maneuvers.

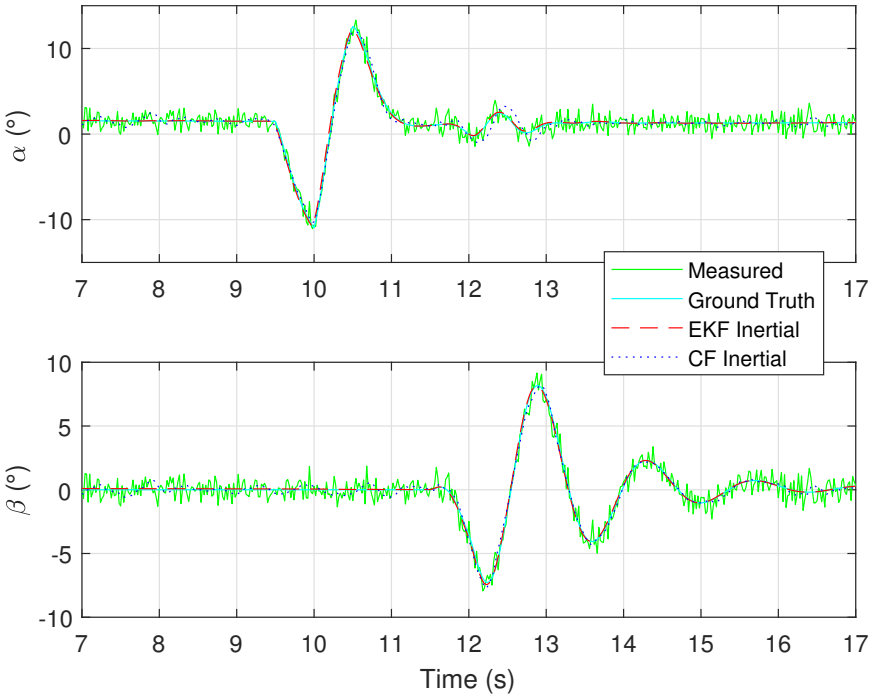

Figure 3.4: Estimated inertial α/β vs. ground truth during doublet maneuvers.

are calculated and provided in Table 3.1. The statistics table shows that all four filters can estimate AOA and AOS accurately. EKFs perform better than CF because all sensor noises are considered in the equations. Inertial AOA and AOS methods show better performance than AOA/AOS filtering methods. This is because in simulation, aircraft lift and side force coefficients are perfectly known and no turbulence is considered. It is worth mentioning that EKFs require more tuning efforts compared with CFs, given the fact that there are only two parameters to tune for CFs and more than ten parameters to tune for EKFs. CFs are also more computationally efficient than EKF. Detailed tuning strategies for both CFs and EKFs will be explained in the following section.

Table 3.1: Simulated AOA/AOS estimation results during doublet maneuvers (7s - 17s)

Method	AOA mean error (°)	AOA error std. (°)	AOS mean error (°)	AOS error std. (°)
CF Filtered	0.2733	0.2108	0.1945	0.1518
EKF Filtered	0.1790	0.1748	0.0872	0.0771
CF Inertial	0.2531	0.2034	0.1896	0.1344
EKF Inertial	0.0961	0.1684	0.0744	0.0721

3.5 UAV Flight Test Evaluation

3.5.1 Experimental Platforms

A Phastball UAV with flow vanes and a KHawk 55" UAV with a 5-hole Pitot-tube, shown in Fig. 3.5 and Fig. 3.6, are used for flight evaluation of designed filters. General specifications of the UAVs are shown in Table 3.2.

Custom designed avionics were installed on a Phastball UAV to collect data from sensors including GPS, IMU, range sensor, etc. An ADIS-16405 MEMS (micro-electro-mechanical systems) IMU was used to measure the rotation rates and the linear accelerations. An EKF was running on an 800 MHz general-purpose computer (PC104) to provide real time attitude estimation, with a typical error of less than 2 degrees for pitch and roll angles under dynamic circumstances [87]. Flight data were also collected from two angle of attack vanes and one sideslip vane attached to

Table 3.2: Specifications of Phastball and KHawk 55" UAVs

UAV Parameters	Phastball	KHawk 55"
Take-off Weight	11.2 kg	2.5 kg
Max Payload	3.2 kg	0.5 kg
Wingspan	2.4 m	1.4 m
Mean Chord Length	0.33 m	0.38 m
Wing Area	0.73 m^2	0.5 m^2
Control Surfaces	Ailerons/Elevators/Rudder	Elevons
Engine	Electric Ducted Fans	Pusher Motor
Endurance	$\sim$ 5 minutes	$\sim$ 45 minutes
Cruise Speed	30 m/s	20 m/s
Take-off	Asphalt Runway	Bungee

potentiometers with a 10 Volts analog to digital converter at 16-bit resolution, shown in Fig. 3.5. A Pitot-tube was mounted on the nose boom of the aircraft along the longitudinal axis. The signals were sampled at 50 Hz.

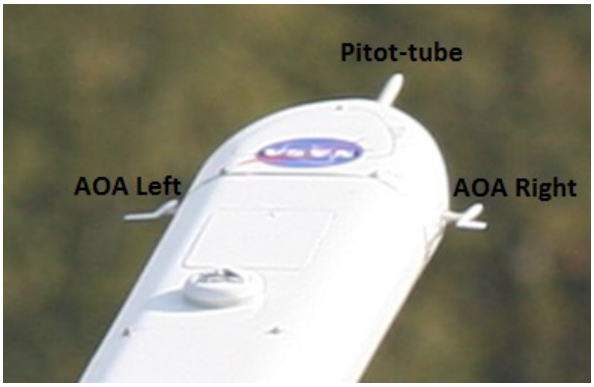

(a)

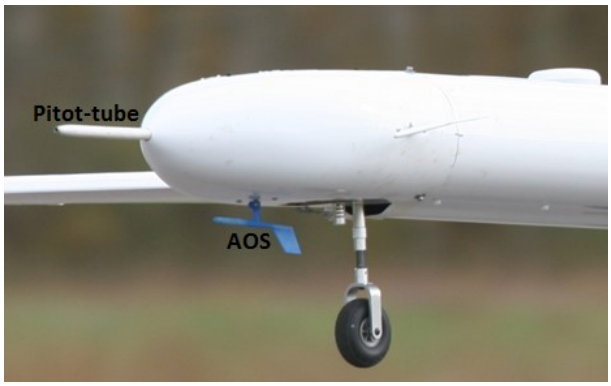

(b)

(c)

Figure 3.5: Phastball UAV platform.

The KHawk 55” UAV supports both manual remote controlled mode and autonomous mode. The airborne avionics includes a Microstrain GX3-25 IMU, a u-blox GPS receiver, a 900 MHz data modem, a Gumstix computer, an open source Paparazzi autopilot, and a manufacturer calibrated Aeroprobe 5-hole air data system (ADS). The 5-hole Pitot-tube setup is shown in the right of Fig. 3.6. All sensor data are logged onboard the aircraft including inertial data (100 Hz), GPS data (4 Hz), and air data (100 Hz). The Microstrain GX3-25 IMU on KHawk 55” UAV can provide attitude estimates with a static accuracy of ± 0.5 degrees and a typical dynamic accuracy of ± 2 degrees for attitude estimation, based on the manufacturer [88]. It is worth mentioning that the Aeroprobe 5-hole Pitot-tube has an airspeed range of 8 to 45 m/s and AOA/AOS range of -20 to 20 degrees. In other words, the Aeroprobe Pitot-tube will not report a valid measurement when operating outside of the calibrated range.

Figure 3.6: KHawk 55” UAV platform.

The lift and side force coefficients of Phastball and KHawk 55” are shown in Table 3.3. The Phastball coefficients were identified from previous flight tests [89], shown in the top of Table 3.3. The flight data were collected during nominal flight conditions with elevator, aileron, and rudder doublet maneuvers. The KHawk 55” coefficients were identified from flight tests using the least squares method [90], shown in the bottom of Table 3.3.

Table 3.3: Lift and side force coefficients of Phastball (top) and KHawk 55" (bottom) UAVs

C_{L_0}	$C_{L_\alpha}(rad^{-1})$	$C_{L_q}(s/rad)$	$C_{L_{\delta_e}}(rad^{-1})$	C_{Y_0}	$C_{Y_\beta}(rad^{-1})$	$C_{Y_p}(s/rad)$	$C_{Y_r}(s/rad)$	$C_{Y_{\delta_a}}(rad^{-1})$	$C_{Y_{\delta_r}}(rad^{-1})$
0.1	3.309	41.937	1.787	0	-0.271	0	0.058	0	0.045
0.0563	1.8789	0.1796	0.8297	0.0037	-0.25	0.0065	0.0123	0.0351	NA

3.5.2 Filter Implementation and Tuning for Flight Test

This section summarizes and discusses the filter implementation and tuning process for flight test data.

During the filter implementation process, the locations of sensors and characteristics of sensors need to be carefully considered. For example, if the IMU is not installed at the center of gravity of an aircraft, lever arm and calibration might be required for all IMU measurements [52]. Sensor characteristics including the IMU and airspeed sensor are also critical. IMU measurements are known to have bias errors, which need to be removed to achieve better estimation results. In this chapter, the IMU biases are assumed to be provided by navigation systems, which is the case for many commercial, custom-made, and open source autopilots and IMUs. For example, the Phastball UAV has a 15-state EKF running on board for the estimation of aircraft attitude and accelerometer/gyroscope biases [84]. The Microstrain GX3-25 IMU used on KHawk 55" also provides real-time IMU bias estimates [91]. With the availability of this information, biases can be removed from IMU measurements before passing them to the AOA/AOS estimation filters.

Also note that for different types of Pitot-tubes with varying nose shapes and impact openings, the conversion equation from differential pressure to airspeed may be different due to effects from inclination angles [92]. Many Pitot-tubes used on small UAVs are small-bore cylindrical tubes, which are insensitive to inclination angles with a range of ± 12 degrees [92]. Therefore, the following equation is used in this chapter.

$$V_{pitot} = V. \tag{3.18}$$

Pitot-tubes are usually mounted along the longitudinal axis of an aircraft. Thus, for Pitot-tubes

that are sensitive to inclination angles, only the projection of the true airspeed in the body x-axis can be measured. The simple output equation can be used [46]

$$V_{pitot} = u, \tag{3.19}$$

instead of V in Eq. (3.2). The true airspeed V needs to be expressed using Pitot-tube airspeed V_{pitot}, given as:

$$V = \frac{V_{pitot}}{\cos\alpha\cos\beta}. \tag{3.20}$$

The tuning of CF is relatively simple with only two parameters, ζ_{cf} and $\omega_{n_{cf}}$, to tune. These two parameters determine the frequency response and bandwidth of the filter. The CF damping ratio ζ_{cf} is selected as 0.7, considering typical dynamic responses of a second order system. The filter frequency $\omega_{n_{cf}}$ is selected as 10 rad/s, which is close to the short period frequency of small UAVs used in this chapter.

The tuning process of the EKF for flight tests can be tedious since more parameters are involved. In this chapter, some of the process noises and measurement noises with physical meanings are determined through experiments, while others are manually tuned. For example, IMU measurement noises are determined from ground tests [86]. By doing this, the EKF tuning load is significantly reduced. Detailed EKF tuning parameters used for Phastball and KHawk 55" are shown in Table 3.4. Note that the process noise covariance $\mathbf{Q}$ (corresponding to the input vector $\mathbf{u}$), and measurement noise covariance $\mathbf{R}$ (corresponding to the observation vector $\mathbf{z}$) are assumed to be diagonal. The initial covariance $\mathbf{P}_0$ (corresponding to the state vector $\mathbf{x}$) is assumed to be an identity matrix in this chapter.

3.5.3 Results of Flight Test Evaluation

Based on the availability of sensors and aircraft model parameters, corresponding filters are evaluated on both the Phastball and KHawk 55" UAV platforms.

All four fusion algorithms are compared using the Phastball UAV's flight data, where IMU

Table 3.4: EKF tuning parameters for Phastball and KHawk 55" UAVs

Phastball AOA/AOS Filtering EKF		Phastball Inertial EKF		KHawk 55" Inertial EKF	
Process Noise **Q**	Measurement Noise **R**	Process Noise **Q**	Measurement Noise **R**	Process Noise **Q**	Measurement Noise **R**
$0.02889^2\ (m/s^2)^2$	$1\ (m/s)^2$	$0.02889^2\ (m/s^2)^2$	$10^{-7}\ (rad)^2$	$0.01366^2\ (m/s^2)^2$	$10^{-7}\ (rad)^2$
$0.02899^2\ (m/s^2)^2$	$4\times10^{-4}\ (rad)^2$	$0.02899^2\ (m/s^2)^2$	$10^{-5}\ (rad)^2$	$0.01819^2\ (m/s^2)^2$	$10^{-7}\ (rad)^2$
$0.02471^2\ (m/s^2)^2$	$4\times10^{-4}\ (rad)^2$	$0.02471^2\ (m/s^2)^2$		$0.02007^2\ (m/s^2)^2$	
$0.00376^2\ (rad/s)^2$		$0.00376^2\ (rad/s)^2$		$0.00251^2\ (rad/s)^2$	
$0.00468^2\ (rad/s)^2$		$0.00468^2\ (rad/s)^2$		$0.00309^2\ (rad/s)^2$	
$0.00413^2\ (rad/s)^2$		$0.00413^2\ (rad/s)^2$		$0.00266^2\ (rad/s)^2$	
$10^{-7}\ (rad)^2$		$10^{-7}\ (rad)^2$		$10^{-7}\ (rad)^2$	
$10^{-7}\ (rad)^2$		$10^{-7}\ (rad)^2$		$10^{-7}\ (rad)^2$	
		$1\ (m/s)^2$		$0.25\ (m/s)^2$	

measurements $[a_x, a_y, a_z]$ $[p, q, r]$, airspeed measurement $[V_{pitot}]$, flow vane measurements $[\alpha, \beta]$, aircraft attitude $[\phi, \theta]$, aircraft lift coefficients $[C_{L_0}, C_{L_\alpha}, C_{L_q}, C_{L_{\delta_e}}]$, and side force coefficients $[C_{Y_0}, C_{Y_\beta}, C_{Y_p}, C_{Y_r}, C_{Y_{\delta_a}}, C_{Y_{\delta_r}}]$ are available.

The CF filtered AOA and AOS are compared with flow vane measurements, shown in Fig. 3.7. The enlarged results for doublet maneuvers are shown in Fig. 3.8. It can be observed that the CF filtered out high frequency noise from raw flow angle measurements. On manned aircraft, noisy flow vane measurements are typically filtered by a CF and then used for stall warnings or control purposes [67, 71]. Similar approaches can be used on UAVs. The EKF filtered AOA and AOS are shown in Fig. 3.9 and Fig. 3.10 (enlarged). It can be observed that the EKF also filters out high frequency noise in flow angle measurements.

Inertial AOA and AOS estimation using the CF and EKF are further presented in Figs. 3.11-3.14. Inertial AOA and AOS are especially useful for cases where direct flow angle measurements are not available, such as low cost UAVs and hypersonic aircraft. They can also be used for the detection of turbulence encounters when compared with direct flow angle measurements [63, 82].

Statistical analysis of estimation results from two inertial filters are provided in Table 3.5. The flow vane measurements are used as the ground truth for comparison. It can be seen from the table that the inertial EKF has similar performance compared with the inertial CF for AOA/AOS estimation.

As for KHawk 55" UAV, IMU measurements $[a_x, a_y, a_z, p, q, r]$, airspeed measurement $[V_{pitot}]$, aircraft attitude $[\phi, \theta]$, aircraft lift coefficients $[C_{L_0}, C_{L_\alpha}, C_{L_q}, C_{L_{\delta_e}}]$, and side force coefficients

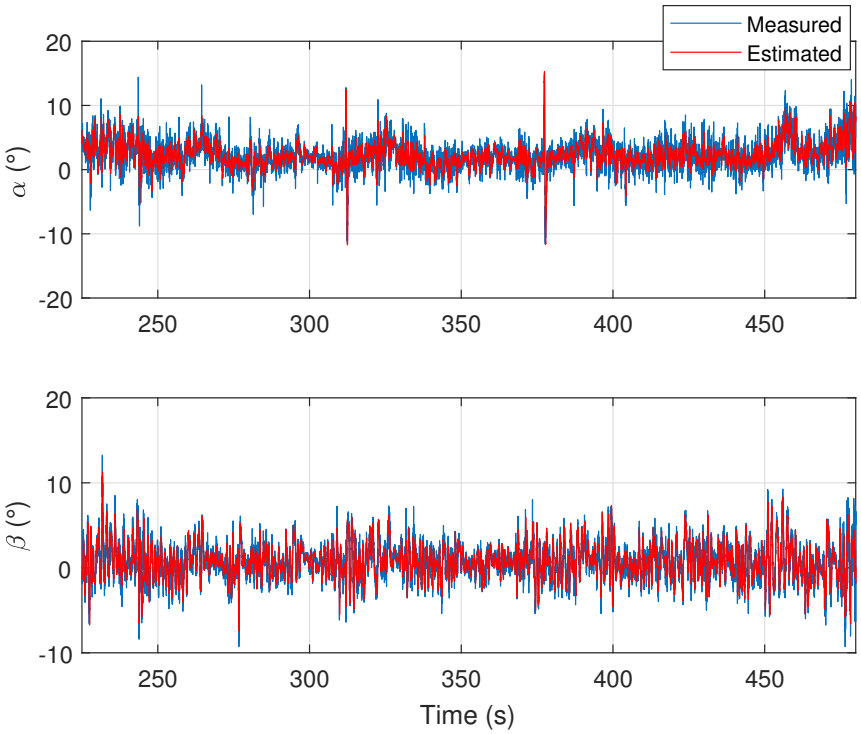

Figure 3.7: Phastball CF filtered results vs. flow vane measurements.

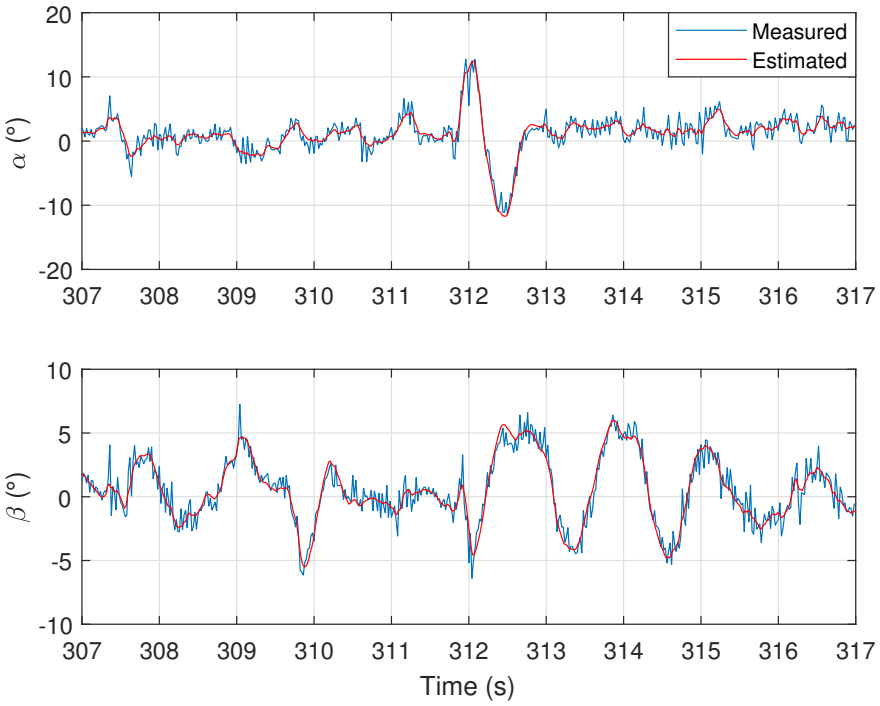

Figure 3.8: Phastball CF filtered results vs. flow vane measurements (enlarged).

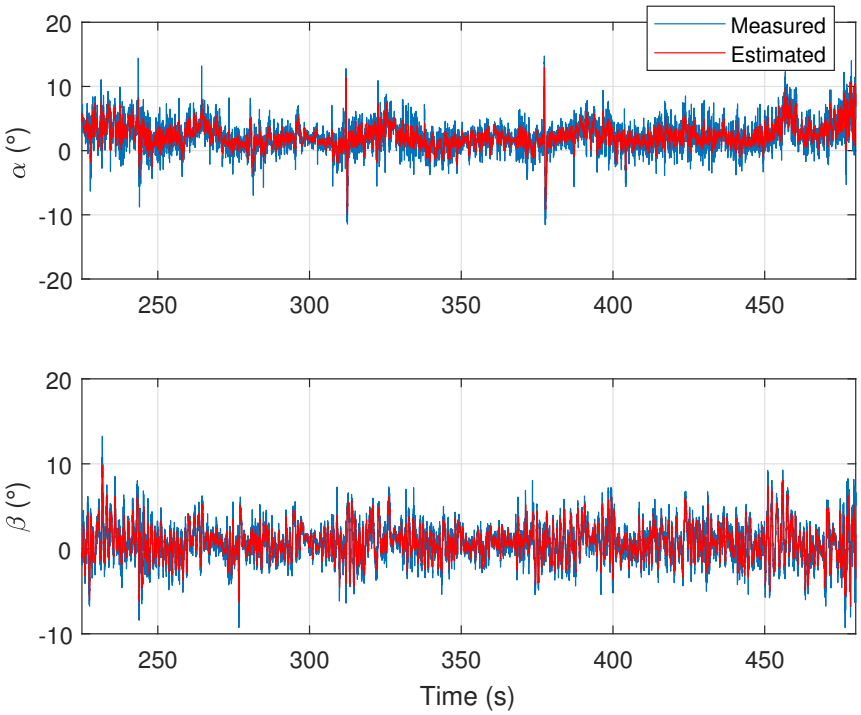

Figure 3.9: Phastball EKF filtered results vs. flow vane measurements.

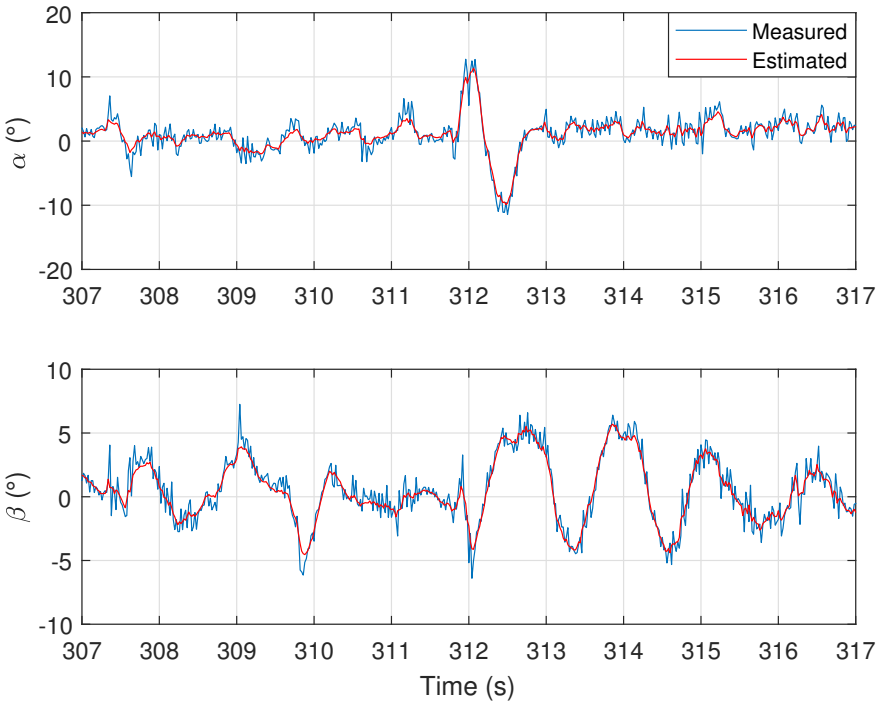

Figure 3.10: Phastball EKF filtered results vs. flow vane measurements (enlarged).

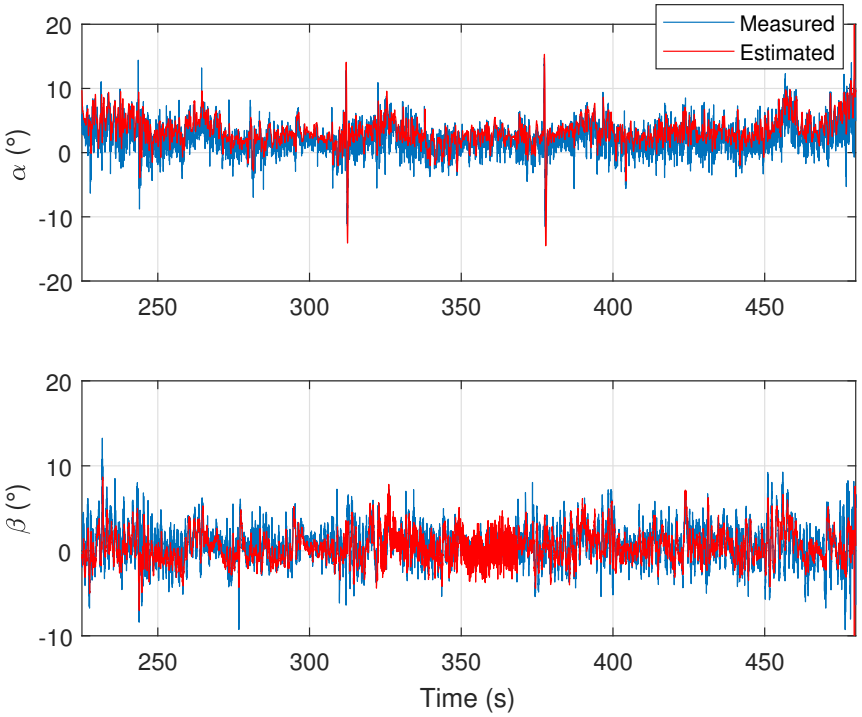

Figure 3.11: Phastball CF inertial results vs. flow vane measurements.

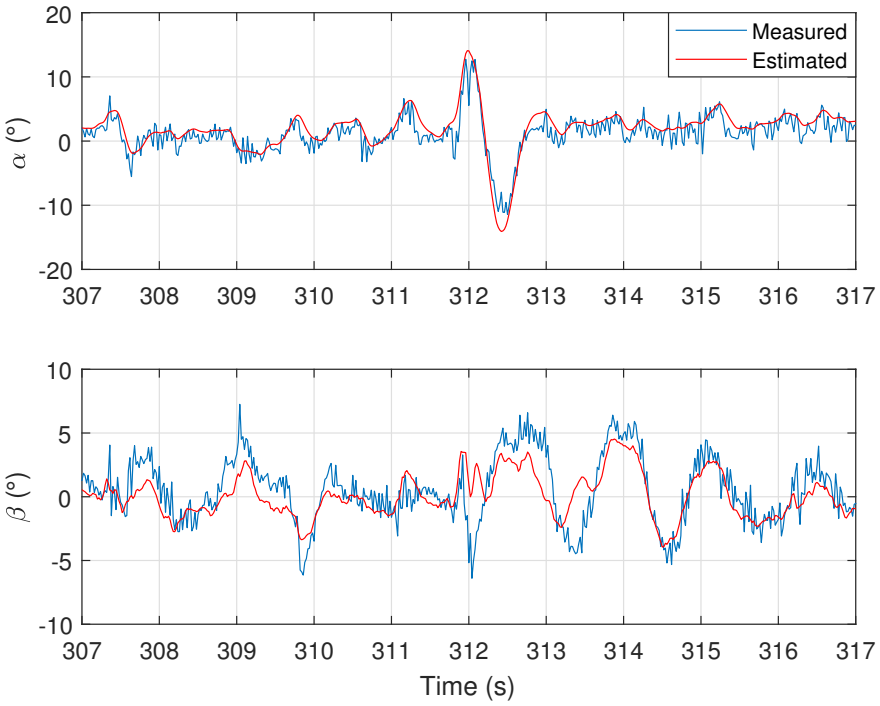

Figure 3.12: Phastball CF inertial results vs. flow vane measurements (enlarged).

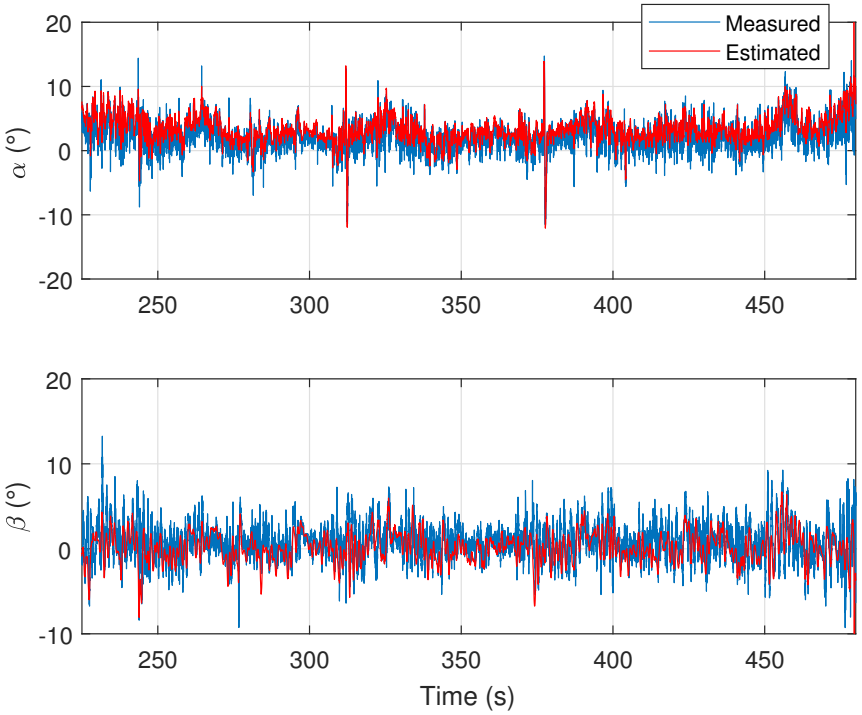

Figure 3.13: Phastball EKF inertial results vs. flow vane measurements.

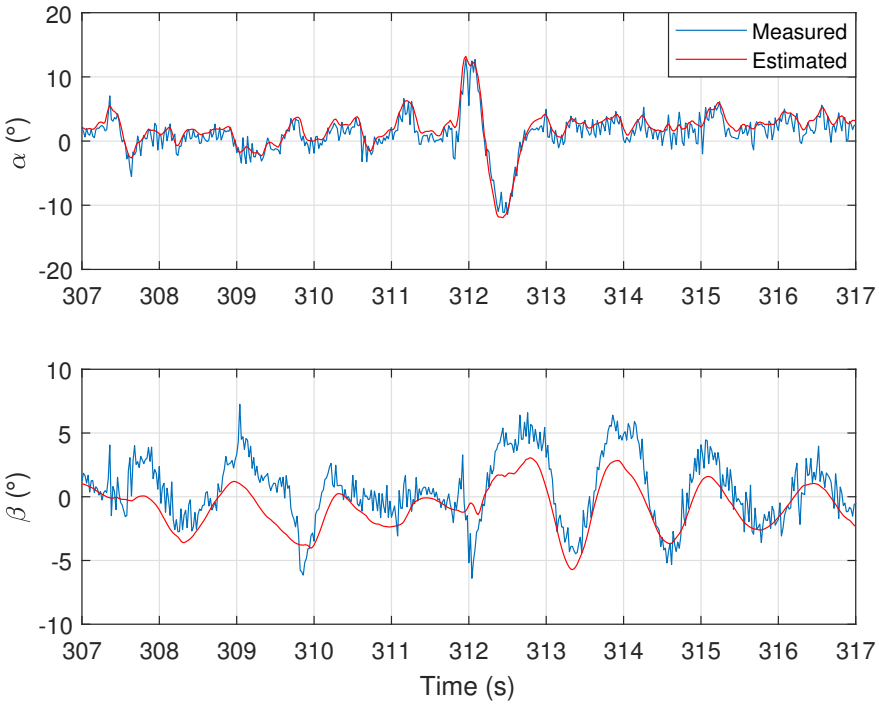

Figure 3.14: Phastball EKF inertial results vs. flow vane measurements (enlarged).

Table 3.5: Statistical analysis of filter estimation results using Phastball data

Method	AOA mean error (°)	AOA error std. (°)	AOS mean error (°)	AOS error std. (°)
CF Inertial	1.2031	0.9653	1.4859	1.4953
EKF Inertial	1.4137	1.4144	1.1394	1.6624

$[C_{Y_0}, C_{Y_\beta}, C_{Y_p}, C_{Y_r}, C_{Y_{\delta_a}}, C_{Y_{\delta_r}}]$ are available. Only two inertial AOA/AOS estimation filters are evaluated because the 5-hole Pitot-tube has been calibrated by the manufacturer. Flight data were collected during the flight test with aggressive elevator sinusoidal inputs and aileron doublets. The aircraft was close to stall several times during the flight test. Estimated AOA/AOS and 5-Hole Pitot-tube measured AOA/AOS are shown in Figs. 3.15-3.18.

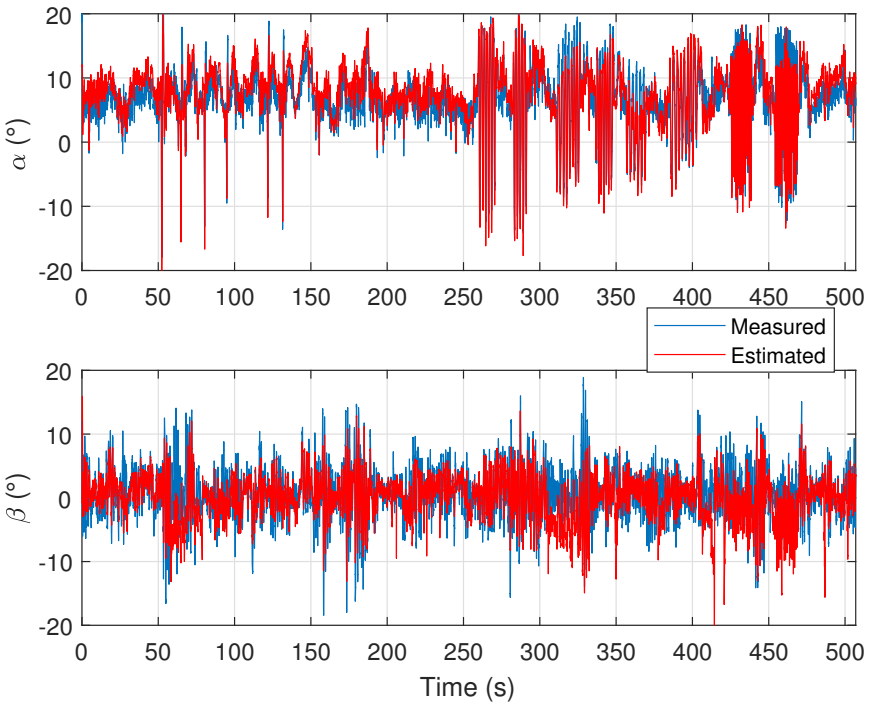

Figure 3.15: KHawk 55" CF inertial results vs. 5-hole measurements.

Statistical analysis of estimation results are provided in Table 3.6. The AOA and AOS measured by the 5-hole Pitot-tube are used as ground truth for comparison. It can be observed from the table that the CF has similar performance compared with the EKF for inertial AOA/AOS estimation.

In summary, all four filters are effective for flow angle estimation. Two direct flow angle

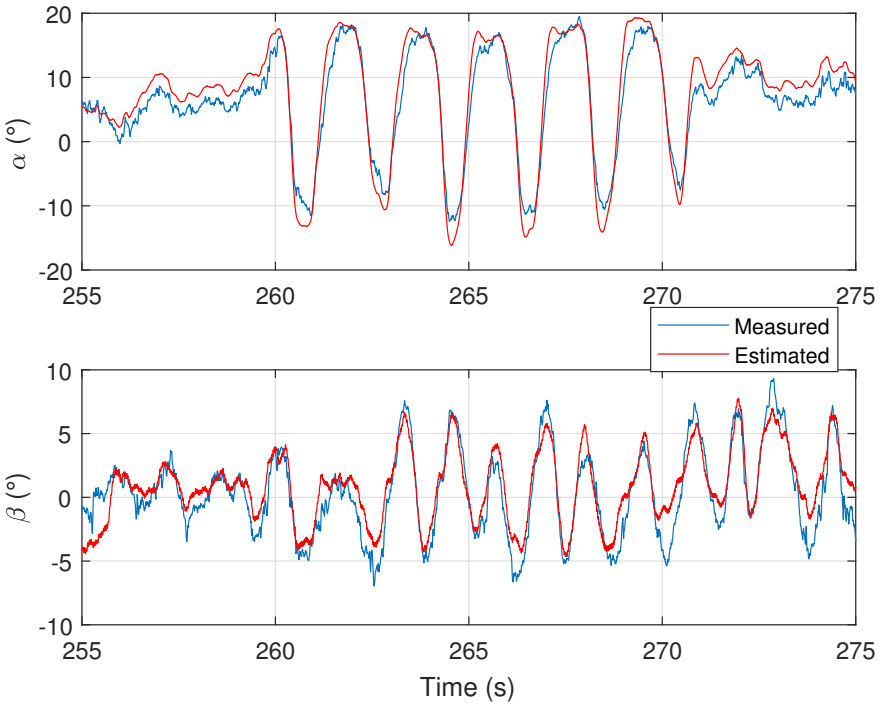

Figure 3.16: KHawk 55” CF inertial results vs. 5-hole measurements (enlarged).

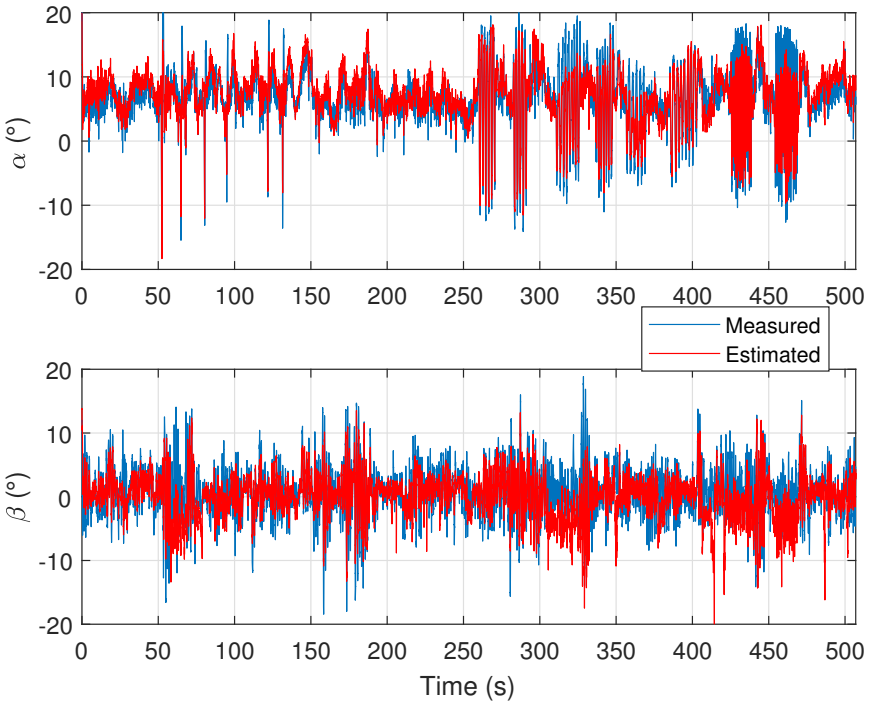

Figure 3.17: KHawk 55” EKF inertial results vs. 5-hole measurements.

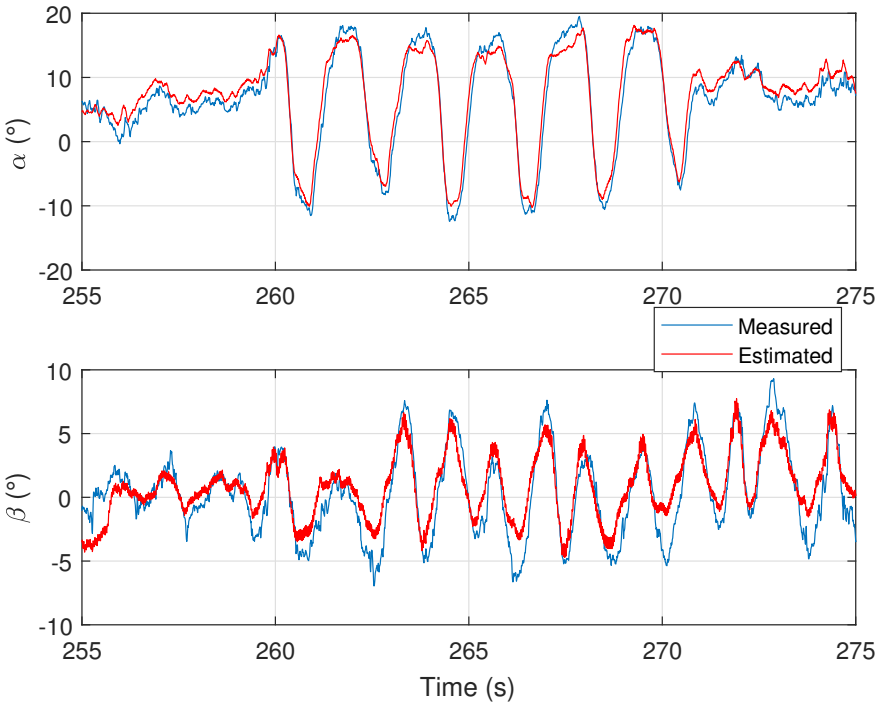

Figure 3.18: KHawk 55" EKF inertial results vs. 5-hole measurements (enlarged).

Table 3.6: Statistical analysis of filter estimation results using KHawk55" data

Method	AOA mean error (°)	AOA error std. (°)	AOS mean error (°)	AOS error std. (°)
CF Inertial	1.9640	1.2042	2.0204	2.1768
EKF Inertial	1.8805	1.3643	2.0384	2.1030

filtering methods are able to increase the reliability of the direct flow angle measurement system. Two inertial filters can work independently or work as a backup for direct flow angle measurement systems. The tuning strategies used in this chapter work desirably across platforms. The estimation errors from inertial flow angle estimation filters may be caused by sensor alignment errors and uncorrected local flow effects such as upwash and sidewash.

The following suggestions are made based on flight test results. If there are low quality direct flow angle measurements available on UAVs and their major applications are for stall warning or flight control, the flow angle filtering CF is recommended since it is the easiest to implement among the four filters and requires far less tuning than the flow angle filtering EKF. However, if the major

applications are for sensor fault detection or dynamic wind estimation, the flow angle filtering EKF is recommended given its flexibility and robustness [46,93]. When direct flow angle measurements are not available on UAVs, the inertial CF and inertial EKF can be implemented. Similar to the flow angle filtering filters, the inertial CF is recommended for stall warning and flight control, whereas the inertial EKF is recommended for sensor fault detection or prevailing wind estimation. There are also many other applications if a UAV has redundant flow angle information, i.e. direct flow angle measurements and inertial flow angle estimates. Such a UAV platform can be used in areas such as turbulence detection/modeling and aircraft structure damage assessment [63, 82].

3.6 Conclusions & Future Work

Four AOA/AOS (flow angle) estimation filters are designed and evaluated on two different UAV platforms, which include a new CF and a new EKF for inertial AOA/AOS estimation as well as a CF and an EKF for the filtering of direct flow angle measurements. Thorough implementation and tuning process of the filters are introduced in the chapter. Detailed analysis and recommendations for different applications are also provided. Simulation results show that all four filters can estimate flow angles accurately compared with the ground truth. For flight test data, the proposed inertial CF and EKF show good performance in estimating flow angles (the root mean square errors are less than 1.5 degrees under nominal flight conditions and around 2 degrees under aggressive maneuvers) compared with direct flow angle measurements from the mechanical vanes or 5-hole Pitot-tube. It can also be observed that the inertial CF has similar performance with the inertial EKF, while taking less tuning efforts and computational resources. The advantage of the inertial EKF lies in its flexibility in the formulation, which can be easily modified for estimation of other states such as 3D wind. The two flow angle filtering methods show their effectiveness in rejecting high frequency noise when direct flow angle measurements are available. In the future, more cases on the estimation of AOA and AOS will be studied under different dynamic flow fields, such as wake vortices generated by aircraft and turbulence caused by fire. This will greatly help the understanding of the interaction among aircraft, dynamics flow fields, and flight controllers.

Chapter 4

3D Wind Estimation Using Small UAVs

Abstract

The presence of wind and turbulence in the atmospheric boundary layer (ABL) has an enormous influence on flight performance and safety of manned and unmanned aircraft. Especially, the smaller size and lighter weight of small unmanned aerial vehicles (UAVs) make them more vulnerable to wind and turbulence caused by microbursts, mountain and ocean waves, or wake vortices downstream of buildings. Therefore, it is essential to have the knowledge of the wind along the UAV trajectory and predict the wind field ahead for improved flight safety and efficiency. In this chapter, two novel extended Kalman filters (EKFs) are proposed for UAV based 3D wind estimation (including both horizontal and vertical components) without relying on direct air flow angle measurements from multi-hole probes or mechanical vanes. The proposed filters exploit the characteristics of 3D wind by utilizing the random walk process (the proposed 9-state EKF) and the sinusoidal wave model (the proposed 12-state EKF). Both simulation and UAV flight test data are used to validate the proposed filters. Simulation results show that both EKFs can estimate the 3D wind accurately. Additionally, with the help of sinusoidal wave model, the proposed 12-state EKF demonstrates its potential of estimating and predicting unsteady 3D winds with sinusoidal patterns under certain circumstances. Furthermore, flight test results show that both filters can estimate 3D wind accurately when compared with mean wind collected by a 3D sonic anemometer on the ground.

4.1 Introduction

It is predicted that seven million unmanned aerial vehicles (UAVs) will be operating in the national airspace in 2020 by the FAA [94]. These include big autonomous air taxis, medium UAVs for long range road/railway health monitoring, and small UAVs for package delivery or photography. In fact, most of these UAVs will be operating in the atmospheric boundary layer (ABL), which is full of different scales of gusts and turbulence [1, 95]. Compared with manned aircraft, small UAVs are more vulnerable to strong wind and turbulence due to their smaller sizes and lighter weights [96–98]. Extreme weather and complex terrain will have considerable influence on flight performance and safety of these UAVs. On the one hand, the presence of dynamic wind, such as building wake vortices and storm/fire generated turbulence, creates many challenges in the control of UAVs. On the other hand, small UAVs can potentially extract energy from certain types of spatio-temporal wind fields such as thermal wind, wake vortex, or general gusts [51, 55, 99, 100] if the wind can be sensed or predicted accurately. To enable safe and efficient integration of small UAVs into the next generation national airspace, accurate estimation and prediction of the wind magnitude, frequency, and spatial pattern along or ahead of the UAV trajectory are indispensable, especially for beyond visual line of sight (BVLOS) operations.

Many researchers in the guidance, navigation, and control (GNC) and meteorological communities have worked on the problem of wind estimation using passenger/cargo aircraft, general aviation aircraft, and small UAVs. Lee presented an unscented Kalman filter (UKF) based wind estimator for KC-135R in simulation using conventional autopilot sensors [101]. Hong solved the 3D wind estimation problem for general aviation aircraft in an optimal control manner in simulation [26]. With the emergence of small UAVs in recent years, more researchers started to use them as effective validation tools for wind estimation algorithms due to their low risk and low cost. Langelaan showed in simulation that 3D wind can be calculated directly using wind triangulation [32]. Reineman successfully demonstrated the measurement of vertical winds above the ocean waves, using a military grade UAV equipped with a customized multi-hole probe [33]. Although 3D wind fields can be directly calculated using a high fidelity inertial measurement unit

and a multi-hole probe, this approach is not suitable for most small UAVs due to budget and size limits. Instead, different types of stochastic filters have been developed for wind estimation using low-cost micro-electro-mechanical systems (MEMS) sensors. Cho presented a simple extended Kalman filter (EKF) for the estimation of 2D horizontal wind using only a conventional Pitot-tube and a GPS receiver [37]. Johansen proposed a Kalman filter based cascaded structure to estimate wind velocities using kinematic relationships [38]. Lie took use of the full aircraft dynamic model to estimate horizontal wind without relying on airspeed measurement [36]. Many researchers have achieved reasonable estimation of mean horizontal wind using UAV flight data. However, less work can be found in the literature on 3D wind estimation using low cost UAVs. Rhudy developed an UKF that could estimate aircraft attitude and 3D wind using the airspeed measurement and mechanical vane measurements of angle of attack (AOA/α) and angle of sideslip (AOS/β) [45] and later showed that the similar structure could be used to estimate wind without using airspeed measurement [102]. Brossard proposed a multiplicative Kalman filter for 3D wind estimation, which was tightly coupled with navigation [39]. As can be seen from the existing literature, for the problem of wind estimation, especially 3D wind estimation, high quality IMU and GPS, direct flow angle measurements, or sophisticated aircraft dynamic models are required, which may not be available for most low-cost UAVs. In addition, most literature use the random walk process to model the wind dynamics and use wind triangular rules as the main measurement equation in a typical Kalman filter setting. Note that the random walk wind model has been shown to work for the estimation of prevailing wind, or the mean wind. However, as the wind field can be divided into three broad categories, i.e. mean wind, waves, and turbulence [1], the random walk process may not be a good representation of intrinsic characteristics of real world wind, especially for turbulent or gusty environments such as wind waves above the ocean surface or in the atmospheric boundary layer. Due to the unpredictable nature of the random walk process, filters based on it may not be suitable for wind prediction. This is especially important for applications that require accurate downwind estimation, as observations and measurements have shown that the downwind may contain significant sinusoidal wave patterns for certain terrain and weather conditions [103, 104].

This chapter presents two novel EKFs (a 9-state EKF and a 12-state EKF) for the estimation of 3D wind using a small UAV. The major contributions of this chapter can be summarized as follows:

1. A new 9-state EKF is proposed to estimate 3D wind effectively without relying on direct flow angle measurements. The main novelty of the 9-state EKF comes from its accurate estimation of vertical wind using estimated inertial AOA and AOS. In addition, the proposed filter can robustly track slowly evolving 3D wind and can be easily integrated into existing autopilots on small UAVs that do not have flow angle sensors such as a multi-hole Pitot-tube, or flow angle vanes;

2. A new 12-state EKF is proposed to combine the sinusoidal wave model with the typical random walk process to model wind dynamics. To the best knowledge of the authors, this is the first time that the sinusoidal wave model is used for UAV based wind estimation problem. The introduction of sinusoidal wave model makes it possible for the proposed EKF to estimate both the wind magnitude and its dominant frequency for applications such as energy harvesting, gust analysis, and aircraft structure certification [105–107];

3. Simulation and flight test validations are performed using the KHawk 55" UAV platform. In simulation, both proposed filters show good performance with generated sinusoidal wave plus Dryden turbulence. Furthermore, the effectiveness of both filters for 3D wind estimation is also shown through the comparison between UAV flight experiment results and ground wind measurements from a weather station.

The organization of this chapter can be summarized as follows. The problem of 3D wind and turbulence estimation is introduced in Sec. 4.2 along with the two proposed EKFs. The simulation results are presented in Sec. 4.3. The UAV platform and experimental setup are described in Sec. 4.4. The flight test results are presented in 4.5. Conclusions are made in Sec. 4.6.

4.2 3D Wind and Turbulence Estimation Filters

For the problem of wind estimation using an aircraft, the most important equation is the wind triangulation equation 4.1, depicted in Fig. 4.1, where $\boldsymbol{V_g}$ $[V_n, V_e, V_d]$ is the ground speed expressed in the north-east-down (NED) inertial frame, $\boldsymbol{V}$ $[u, v, w]$ is the airspeed expressed in the body frame, $\boldsymbol{V}_{\mathrm{w}}$ $[\mathrm{w}_n, \mathrm{w}_e, \mathrm{w}_d]$ is the wind speed expressed in the NED frame, and $\boldsymbol{R_b^n}$ is the rotation matrix from body frame to the NED frame. When high quality measurements are available from GPS $[V_n, V_e, V_d]$, inertial measurement unit (IMU) $[a_x, a_y, a_z, p, q, r]$, and air data system $[V, \alpha, \beta]$, 3D wind can be directly calculated using the wind triangulation equation [33]. However, those measurements, especially flow angle measurements, are often either corrupted with noises, biases, or simply not available for small UAVs due to their payload and budget constraints. Therefore, estimation filters are often used for the problem of UAV based wind estimation. Instead of relying on direct flow angle measurements, we proposed an aircraft model aided EKF to estimate inertial flow angles in former research [108], which is based mostly on inertial measurements of aircraft responses. In this chapter, two inertial flow angle based EKFs (a 9-state EKF and a 12-state EKF) are proposed for 3D wind and turbulence estimation. The system diagram of both wind estimation filters is shown in Fig. 4.2. Details of these proposed filters will be introduced in the following sections.

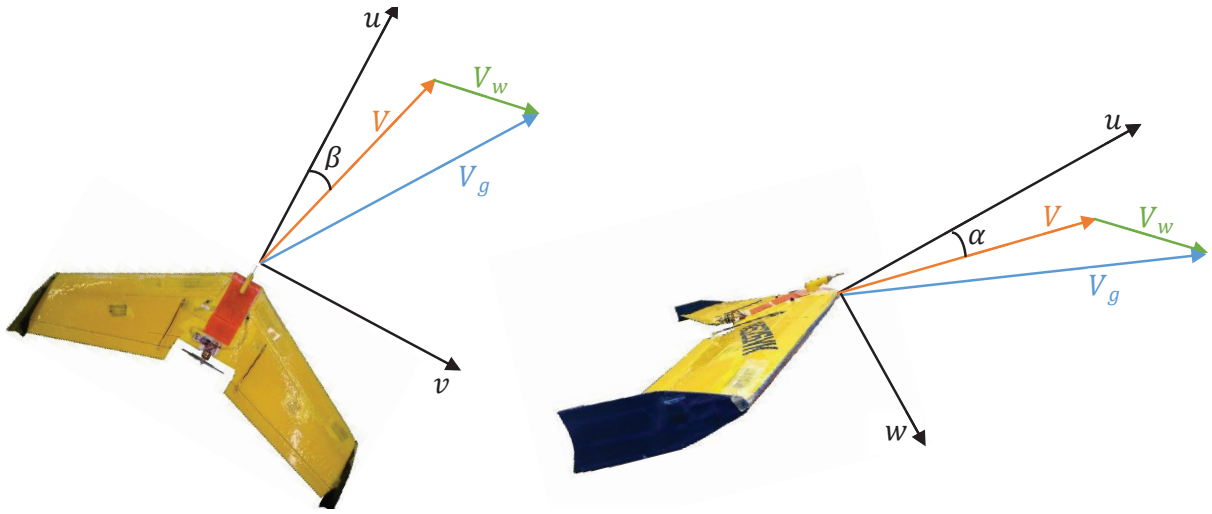

Figure 4.1: Wind triangulation.

$$\begin{bmatrix} V_n \\ V_e \\ V_d \end{bmatrix} = \boldsymbol{R}_{\boldsymbol{b}}^{\boldsymbol{n}}(\phi,\theta,\psi) \begin{bmatrix} u \\ v \\ w \end{bmatrix} + \begin{bmatrix} \mathrm{w}_n \\ \mathrm{w}_e \\ \mathrm{w}_d \end{bmatrix}. \tag{4.1}$$

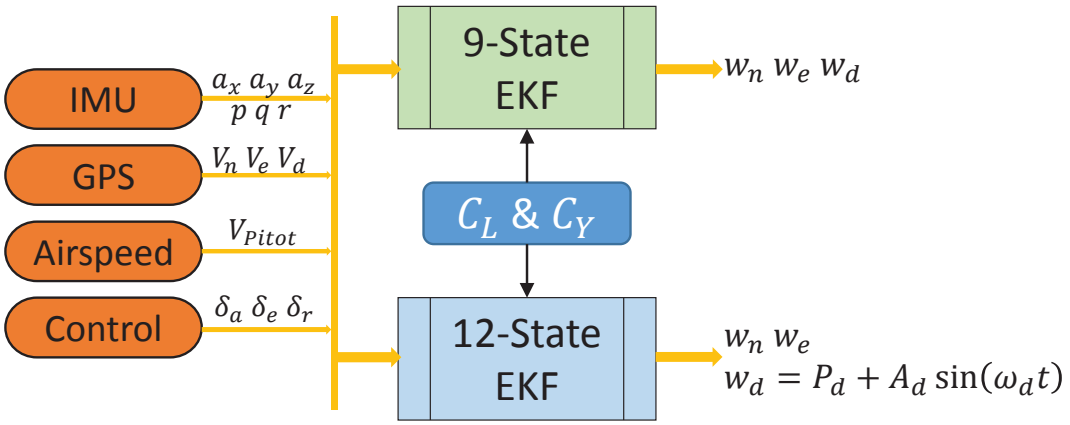

Figure 4.2: System diagram of wind estimation filters.

4.2.1 9-State EKF with Random Walk Process as Wind Model

A 9-state EKF is proposed in this chapter, which considers the simultaneous estimation of aircraft body frame air speed components $[u,v,w]$, Euler angles $[\phi,\theta,\psi]$, and wind velocity components $[\mathrm{w}_n,\mathrm{w}_e,\mathrm{w}_d]$ in the NED frame, shown in Fig. 4.2. The random walk process is used to model wind dynamics. This filter requires the knowledge of GPS ground velocities $[V_n,V_e,V_d]$, accelerations $[a_x,a_y,a_z]$ and rotation rates $[p,q,r]$ from the IMU, air speed measurement $[V_{pitot}]$, control surface deflections $[\delta_e,\delta_a,\delta_r]$, aircraft lift coefficients $[C_{L_0},C_{L_\alpha},C_{L_q},C_{L_{\delta_e}}]$, and side force coefficients $[C_{Y_0},C_{Y_\beta},C_{Y_p},C_{Y_r},C_{Y_{\delta_a}},C_{Y_{\delta_r}}]$.

The propagation equation of this EKF consists of three parts, as shown in Eq. (4.2), where the first three equations are derived from aircraft translational motion [4], three equations in the middle are derived from aircraft rotational motion [4], and the last three equations are wind dynamics modeled as random walk processes [46]. Note that the wind is modeled by random walk process

such that $[\dot{\mathrm{w}}_n \;\; \dot{\mathrm{w}}_e \;\; \dot{\mathrm{w}}_d]^T$ is equal to $[0 \;\; 0 \;\; 0]^T$ plus zero mean Gaussian noise, which is included in the process noise vector $\mathbf{w_k}$.

$$\dot{\mathbf{x}} = \begin{bmatrix} \dot{u} \\ \dot{v} \\ \dot{w} \\ \dot{\phi} \\ \dot{\theta} \\ \dot{\psi} \\ \dot{\mathrm{w}}_n \\ \dot{\mathrm{w}}_e \\ \dot{\mathrm{w}}_d \end{bmatrix} = \begin{bmatrix} -qw + rv - g\sin\theta + a_x \\ -ru + pw + g\cos\theta\sin\phi + a_y \\ -pv + qu + g\cos\theta\cos\phi + a_z \\ p + \tan\theta(q\sin\phi + r\cos\phi) \\ q\cos\phi - r\sin\phi \\ (q\sin\phi + r\cos\phi)/\cos\theta \\ 0 \\ 0 \\ 0 \end{bmatrix} + \mathbf{w_k}. \tag{4.2}$$

$$\mathbf{y} = \begin{bmatrix} V_n \\ V_e \\ V_d \\ V_{pitot} \\ C_{L_0} + \frac{C_{L_q} q\bar{c}}{2V} + C_{L_{\delta_e}}\delta_e \\ \frac{1}{C_{Y_\beta}}(\frac{ma_y}{\bar{q}S} - C_{Y_0} - \frac{C_{Y_p} pb}{2V} - \frac{C_{Y_r} rb}{2V} - C_{Y_{\delta_a}}\delta_a - C_{Y_{\delta_r}}\delta_r) \end{bmatrix} \tag{4.3}$$

$$= \begin{bmatrix} u\cos\psi\cos\theta + v(-\sin\psi\cos\phi + \cos\psi\sin\theta\sin\phi) + w(\sin\psi\sin\phi + \cos\psi\sin\theta\cos\phi) + \mathrm{w}_n \\ u\sin\psi\cos\theta + v(\cos\psi\cos\phi + \sin\psi\sin\theta\sin\phi) + w(-\cos\psi\sin\phi + \sin\psi\sin\theta\cos\phi) + \mathrm{w}_e \\ -u\sin\theta + v\cos\theta\sin\phi + w\cos\theta\cos\phi + \mathrm{w}_d \\ \sqrt{u^2+v^2+w^2} \\ \frac{m(a_x\frac{w}{\sqrt{u^2+w^2}} - a_z\frac{u}{\sqrt{u^2+w^2}}) - T\frac{w}{\sqrt{u^2+w^2}}}{\frac{\rho(u^2+v^2+w^2)S}{2}} - C_{L_\alpha}\tan^{-1}(\frac{w}{u}) \\ \sin^{-1}(v/\sqrt{u^2+v^2+w^2}) \end{bmatrix} + \mathbf{v_k}.$$

The measurements from the Pitot-tube and GPS as well as aircraft lift and side force are used in the update equation. The update equation is a combination of the wind triangle equation, calcula-

tion of air triplets from the body frame air speed components, and aircraft lift/side force equations given by Eq. (4.3).

The last two elements of the update equation are derived from aircraft lift and side force equations. Detailed derivations can be found in Eqs. (4.4)-(4.8) [108].

Lift can be expressed as the projection of thrust and body-axis accelerations in the stability frame, shown in Eq. (4.4) or by using Taylor expansion with coefficients, shown in Eq. (4.5). Note that the thrust projection is much smaller than the lift during normal flight conditions, therefore, it can be removed for simplification.

$$L = m(a_x \sin\alpha - a_z \cos\alpha) - T\sin\alpha \approx m(a_x \sin\alpha - a_z \cos\alpha), \tag{4.4}$$

$$L = C_L \bar{q} S \approx (C_{L_0} + C_{L_\alpha}\alpha + C_{L_{\delta_e}}\delta_e + C_{L_q} q\bar{c}/(2V))\bar{q}S. \tag{4.5}$$

Eq. (4.6) can be derived by substituting lift from Eq. (4.5) in Eq. (4.4) and moving α related terms to the right side of the equation.

$$C_{L_0} + \frac{C_{L_q} q\bar{c}}{2V} + C_{L_{\delta_e}}\delta_e = \frac{m(a_x \sin\alpha - a_z \cos\alpha)}{\bar{q}S} - C_{L_\alpha}\alpha. \tag{4.6}$$

Similarly, by correlating side force equations, shown in Eq. (4.7), and moving β related terms to the right side of the equation, Eq. (4.8) can be derived .

$$Y = ma_y = C_Y \bar{q} S \approx (C_{Y_0} + C_{Y_\beta}\beta + \frac{C_{Y_p} pb}{2V} + \frac{C_{Y_r} rb}{2V} + C_{Y_{\delta_a}}\delta_a + C_{Y_{\delta_r}}\delta_r)\bar{q}S, \tag{4.7}$$

$$\frac{1}{C_{Y_\beta}}(\frac{ma_y}{\bar{q}S} - C_{Y_0} - \frac{C_{Y_p} pb}{2V} - \frac{C_{Y_r} rb}{2V} - C_{Y_{\delta_a}}\delta_a - C_{Y_{\delta_r}}\delta_r) = \beta. \tag{4.8}$$

where b is the wingspan, $\bar{c}$ is the mean chord length, S is the wing area, and $\bar{q}$ is the dynamic pressure.

Note that in the update equation, all terms that contain $[V, \alpha, \beta]$ are implicitly expressed by

$[u, v, w]$ using the relation shown in Eq. (4.9).

$$\begin{bmatrix} V \\ \alpha \\ \beta \end{bmatrix} = \begin{bmatrix} \sqrt{u^2+v^2+w^2} \\ \tan^{-1}(\frac{w}{u}) \\ \sin^{-1}(\frac{v}{V}) \end{bmatrix}. \tag{4.9}$$

4.2.2 12-state EKF with Sinusoidal Wave Model

Similar to most of existing literature, the 9-state EKF introduced in the former section models wind dynamics as a random walk process. As discussed in the introduction section, this method may not be a good representation of real world wind under certain circumstances, especially when sinusoidal waves are dominant. To better describe and estimate the wind under turbulent and gusty conditions, improved wind dynamic models are favored. One widely used idealized gust model is one-minus-cosine gust model. The one-minus-cosine model is used to describe an individual gust, or so called a discrete gust. For the more general case, the continuous gust, or stationary Gaussian random process is preferred [5].

A stationary Gaussian random process can be generated by the superposition of an infinite number of sinusoidal components using Eq. (4.10) [5], where $\Phi(\omega_k)$ is the power spectral density function and Ψ_k is the random phase angle. Although stationary Gaussian random process is well represented by Eq. (4.10), it is challenging to include an infinite number of sinusoidal components in wind estimation filters. To integrate this model into the wind estimation filter structure, a simplification must be made.

$$V_{\mathrm{w}}(t) = \sum_{k=1}^{\infty} \sqrt{\Phi(\omega_k)\Delta\omega}\cos(\omega_k t + \Psi_k). \tag{4.10}$$

Compared with the 9-state EKF, the 12-state EKF proposed in this chapter uses a sinusoidal wave model for downwind dynamics and the same random walk processes for north and east winds, with the objective to estimate the vertical sinusoidal waves more accurately. In fact, observations and measurements have shown that the downwind may contain significant sinusoidal

wave patterns [103, 104] and it is the most important wind component for both UAV flight safety and energy harvesting due to its significant influence on aircraft AOA and stability [106, 109]. The sinusoidal wave model used in the 12-state EKF is a simplified model of the stationary Gaussian random process, as shown in Eq. (4.11), where P_d is the prevailing component of downwind, A_d is the magnitude of the sinusoidal wave component in downwind, ω_d is the angular velocity of the sinusoidal wave experienced by the aircraft, and t represents the time. Compared with the stationary Gaussian random process, the sinusoidal wave model only represents the dominant frequency of the wind and its magnitude at a specific time. The random phase term is ignored in the sinusoidal wave model for simplicity reasons. Although the sinusoidal wave model is a greatly simplified version of the stationary Gaussian random process, it still does a much better job representing the wave component in the wind than the typical random walk process.

$$\mathrm{w}_d = P_d + A_d \sin(\omega_d t). \tag{4.11}$$

To eliminate t from the equation, an intermediate variable Ω_d is introduced [9], where

$$\Omega_d = \omega_d t. \tag{4.12}$$

Then, by assuming P_d, A_d and ω_d as random walking processes, the sinusoidal wave model can be implemented to replace the downwind component in the 9-state EKF with P_d, A_d, Ω_d, and ω_d as new states. Apart from the wind states, other parts of the propagation equation remain the same as the 9-state EKF. Finally, the propagation equation of the proposed 12-state EKF is given by Eq. (4.13). Note that the wind derivatives are not included in the first three equations as they

are treated as noises and are implicitly contained in the process noise vector $\mathbf{w_k}$.

$$\dot{\mathbf{x}} = \begin{bmatrix} \dot{u} \\ \dot{v} \\ \dot{w} \\ \dot{\phi} \\ \dot{\theta} \\ \dot{\psi} \\ \dot{\mathrm{w}}_n \\ \dot{\mathrm{w}}_e \\ \dot{P}_d \\ \dot{A}_d \\ \dot{\Omega}_d \\ \dot{\omega}_d \end{bmatrix} = \begin{bmatrix} -qw + rv - g\sin\theta + a_x \\ -ru + pw + g\cos\theta\sin\phi + a_y \\ -pv + qu + g\cos\theta\cos\phi + a_z \\ p + \tan\theta(q\sin\phi + r\cos\phi) \\ q\cos\phi - r\sin\phi \\ (q\sin\phi + r\cos\phi)/\cos\theta \\ 0 \\ 0 \\ 0 \\ 0 \\ \omega_d \\ 0 \end{bmatrix} + \mathbf{w_k}. \tag{4.13}$$

The update equation of the proposed 12-state EKF is the same as the update equation of the proposed 9-state EKF, which is shown in Eq. (4.3).

4.3 Simulation Results

A 6-DOF UAV simulator is first used to validate the proposed EKFs without using direct flow angle measurements. During the simulation, the aircraft is commanded to follow a circle with a 100-meter radius. Realistic Gaussian noises are added to all sensor measurements.

In the simulation, the north and east winds are assumed to be prevailing wind, while the down-wind follows the sinusoidal pattern since the vertical gust has a bigger impact on aircraft flight performance among the three wind components. Dryden gusts are also added to simulate 3D wind

in a more realistic way. Equations used to generate the simulated wind are shown in Eq. (4.14).

$$\begin{cases} w_n = 4 + \textit{Dryden Gust}, \\ w_e = 3 + \textit{Dryden Gust}, \\ w_d = 1 + A_d \sin(\omega_d)t + \textit{Dryden Gust}. \end{cases} \tag{4.14}$$

where w_n, w_e, and w_d are in m/s. $A_d \in [0,3]$ in m/s and $\omega_d \in [\frac{\pi}{50}, \frac{\pi}{5}]$ in rad/s are chosen to be ramp signals while $t \in [0,200]$ seconds. The magnitude and frequency of the sinusoidal wave are chosen to be ramp signals such that enough excitation is created to make the states observable.

Table 4.1: EKF initial conditions and tuning parameters for simulation

9-state EKF			12-state EKF		
Initial States	Process Noise	Measurement Noise	Initial States	Process Noise	Measurement Noise
$\mathbf{x_0}$	$\mathbf{Q}$	$\mathbf{R}$	$\mathbf{x_0}$	$\mathbf{Q}$	$\mathbf{R}$
30 (m/s)	0.3 $(m/s^2)^2$	0.1 $(m/s)^2$	30 (m/s)	0.3 $(m/s^2)^2$	0.1 $(m/s)^2$
0 (m/s)	0.34 $(m/s^2)^2$	0.1 $(m/s)^2$	0 (m/s)	0.34 $(m/s^2)^2$	0.1 $(m/s)^2$
0 (m/s)	0.32 $(m/s^2)^2$	0.25 $(m/s)^2$	0 (m/s)	0.32 $(m/s^2)^2$	0.25 $(m/s)^2$
0 (rad)	0.0085^2 $(rad/s)^2$	2.5 $(m/s)^2$	0 (rad)	0.0085^2 $(rad/s)^2$	2.5 $(m/s)^2$
0 (rad)	0.0089^2 $(rad/s)^2$	10^{-4} $(rad)^2$	0 (rad)	0.0089^2 $(rad/s)^2$	10^{-4} $(rad)^2$
$\pi/2$ (rad)	0.0089^2 $(rad/s)^2$	10^{-3} $(rad)^2$	$\pi/2$ (rad)	0.0089^2 $(rad/s)^2$	10^{-3} $(rad)^2$
0 (m/s)	1 $(m/s)^2$		0 (m/s)	10^{-2} $(m/s)^2$	
0 (m/s)	1 $(m/s)^2$		0 (m/s)	10^{-2} $(m/s)^2$	
0 (m/s)	1 $(m/s)^2$		0 (m/s)	10^{-5} $(m/s)^2$	
			0 (m/s)	10^{-5} $(m/s)^2$	
			$\pi/2$ (rad)	10^{-7} $(rad/s)^2$	
			0 (rad/s)		

In the simulation test, the initial covariance $\mathbf{P}_0$ (corresponding to the state vector $\mathbf{x}$) is assumed to be an identity matrix. Other initial conditions and tuning parameters are shown in Table 4.1, where the process noise covariance $\mathbf{Q}$ and measurement noise covariance $\mathbf{R}$ are assumed to be diagonal. Throughout simulations, it is observed that the process noise $\mathbf{Q}$, especially those process noises directly related to the wind speed have a strong correlation with the turbulence level. Both filters are relatively less sensitive to the initial states compared with the process and measurement noises related to airspeed and inertial flow angles.

The simulation results of the 9-state EKF are shown in Fig. 4.3 and Fig. 4.4 along with the

wind truth. As shown in Fig. 4.3, the proposed 9-state EKF is able to estimate 3D wind effectively. However, the performance of the 9-state EKF is getting worse with increasing downwind frequency experienced by the UAV, shown in Fig. 4.4. This is because it is increasingly difficult for the random walk process to capture fast-changing sinusoidal waves.

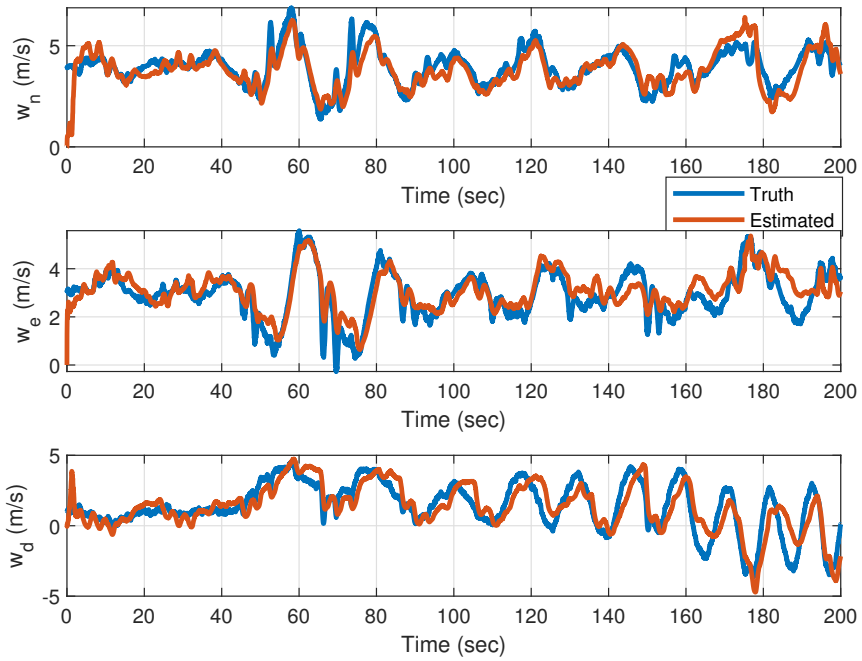

Figure 4.3: Estimated 3D wind using 9-state EKF vs. simulation truth.

The simulation results of the 12-state EKF are further shown in Fig. 4.5 - 4.9. Similar to the 9-state EKF, the proposed 12-state EKF can estimate 3D wind accurately, shown in Fig. 4.5. The enlarged downwind estimation results shown in Fig. 4.6 reveals that the 12-state EKF can estimate sinusoidal waves in the downwind more accurately than the 9-state EKF. The reason is that sinusoidal wave model is incorporated in the 12-state EKF so that the filter has a better knowledge of the dynamics of the flow field. As shown in Fig. 4.7 - 4.9, the 12-state EKF can estimate the prevailing component as well as the changing magnitude and frequency of the sinusoidal wave along the downwind direction. This is useful since it can be used to predict the wind field ahead of the UAV.

To further evaluate the estimation results for both filters, error analysis is performed, shown

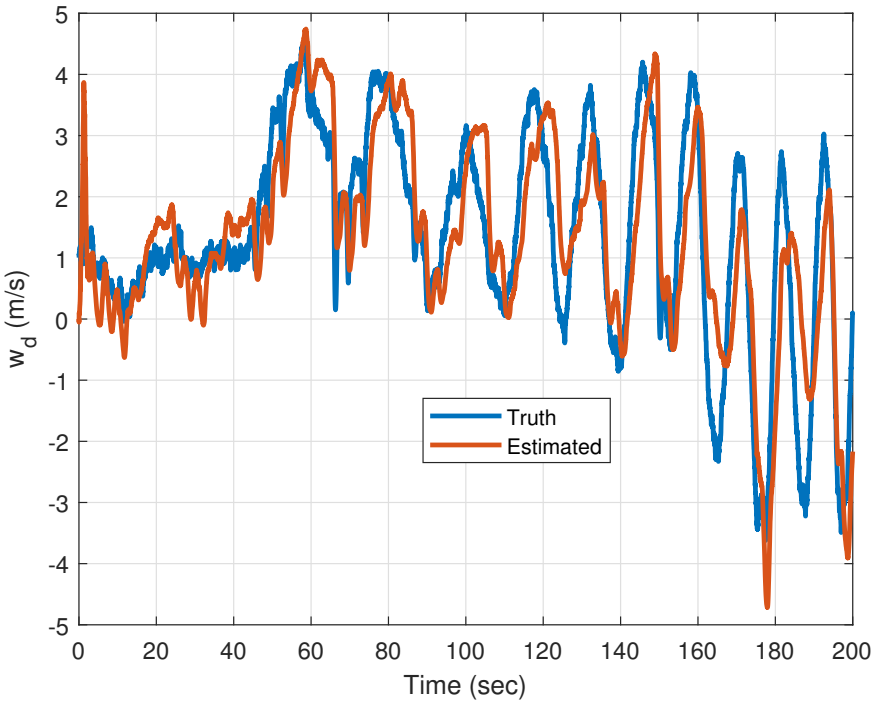

Figure 4.4: Estimated downwind using 9-state EKF vs. simulation truth.

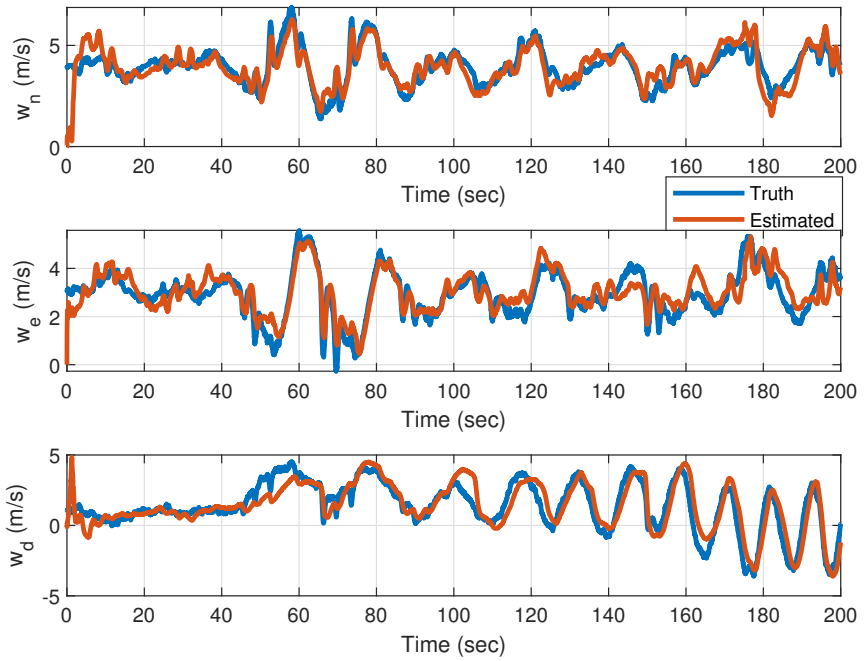

Figure 4.5: Estimated 3D wind using 12-state EKF vs. simulation truth.

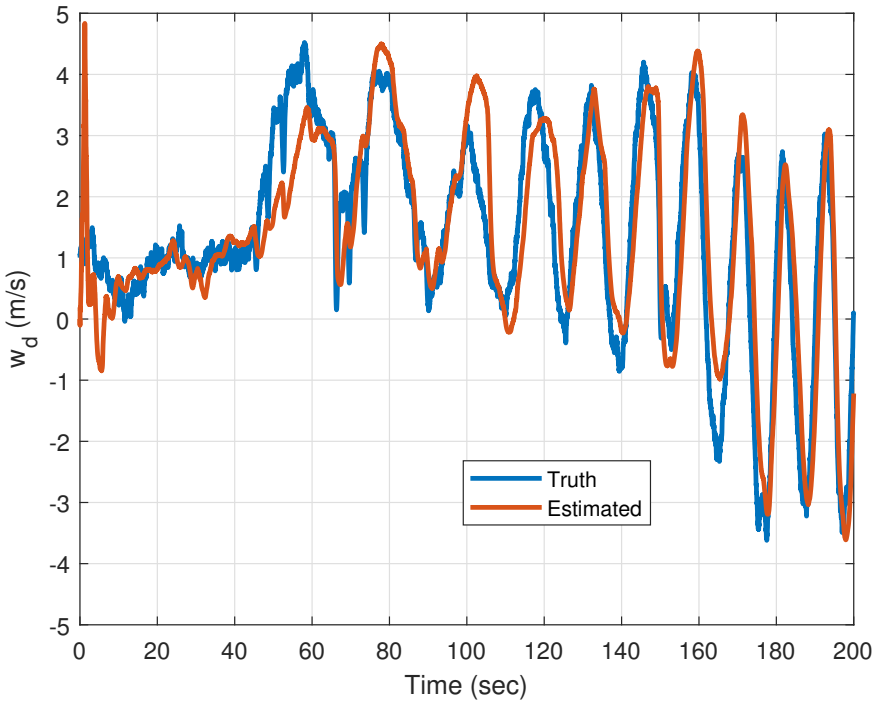

Figure 4.6: Estimated downwind using 12-state EKF vs. simulation truth.

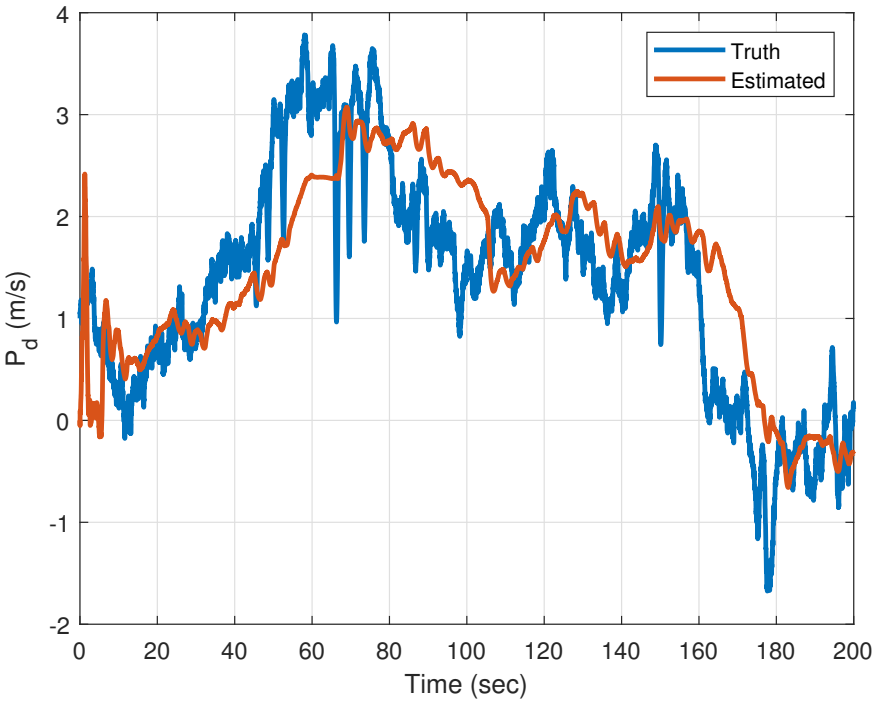

Figure 4.7: Estimated prevailing component of downwind using 12-state EKF vs. simulation truth.

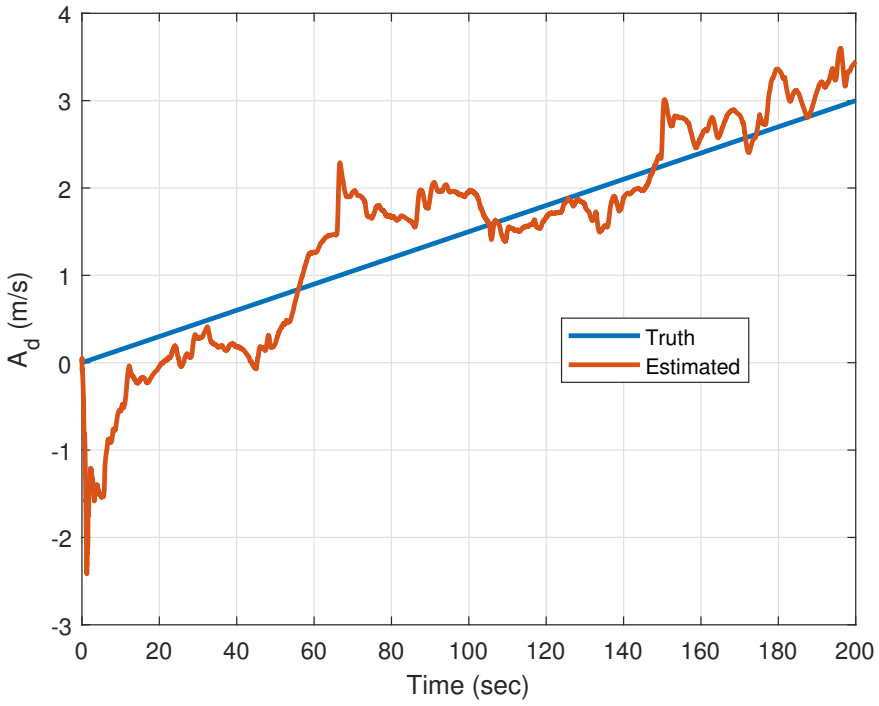

Figure 4.8: Estimated sinusoidal wave magnitude of downwind using 12-state EKF vs. simulation truth.

in Table 4.2. Note that errors are calculated for the time periods after all states are converged (approximately from 60 to 200 seconds). It can be observed that while the two proposed filters have similar performance on north/east wind estimation, the 12-state EKF can estimate the downwind more accurately than the 9-state EKF, as shown in Fig. 4.4 and Fig. 4.6.

Table 4.2: error analysis of estimation results for simulation

	9-state EKF			12-state EKF		
	w_n	w_e	w_d	w_n	w_e	w_d
Mean Error (m/s)	0.4882	0.5454	1.1274	0.4082	0.4058	0.6525
Error Standard Deviation (m/s)	0.3521	0.3304	0.7128	0.3998	0.3048	0.5447

One interesting observation during the tuning process is that when all wind initial states in the 12-state EKF are set to be zeros, the sinusoidal wave model is essentially "switched off". Fig. 4.10 demonstrates such a case by setting the initial state marked in red in Table 4.1 to zero. On one hand, this special characteristic enables the ability of the 12-state EKF to switch between sinusoidal wave

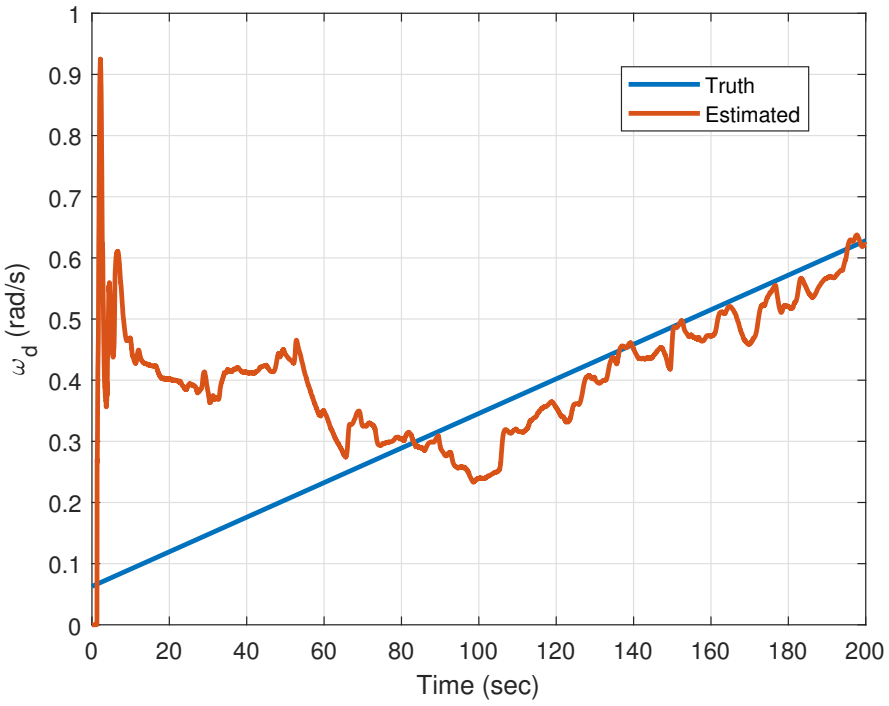

Figure 4.9: Estimated sinusoidal wave frequency of downwind using 12-state EKF vs. simulation truth.

estimation mode and prevailing wind estimation mode smoothly. On the other hand, it indicates that the sinusoidal waves cannot be robustly observed without proper excitation.

4.4 UAV Platform and Experimental Setup

KHawk 55" UAV, shown in Fig. 3.6, was used for data collection and filter validation. The sensor noise characteristics of KHawk 55" are used in simulation validations. General specifications of the UAV are shown in Table 3.2. The KHawk 55" UAV supports both manual remote controlled mode and autonomous mode. The airborne avionics includes a Microstrain GX3-25 IMU, a u-blox GPS receiver, a 900 MHz data modem, a Gumstix computer, an open source Paparazzi autopilot, and an Eagle Tree V3 airspeed sensor. All sensor data are logged onboard the aircraft including inertial data (100 Hz), GPS data (4 Hz), and airspeed data (50 Hz). Noise characteristics of these sensors were determined through ground and flight tests and used in simulations.

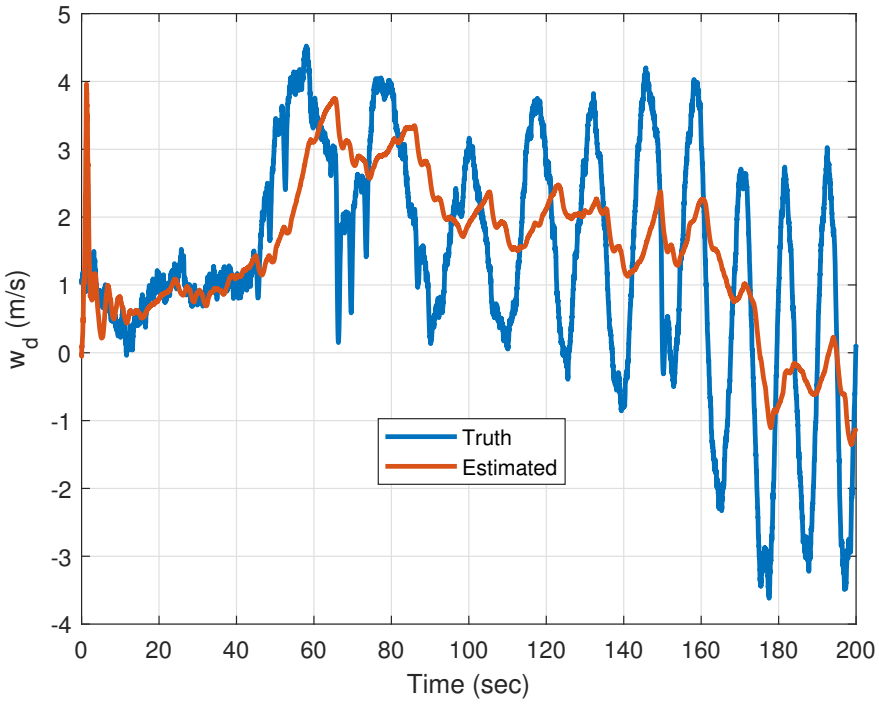

Figure 4.10: Estimated downwind using 12-state EKF vs. simulation truth (sinusoidal wave off).

The lift coefficients (C_L) and side force coefficients (C_Y) of KHawk 55" were identified through flight tests by using the least square method [90]. The identified coefficients are shown in Table 3.3.

In order to validate wind estimation results, the UAV was flown at the field, where a ground weather station is installed, shown in Fig. 4.11. The Campbell Scientific CSAT3 wind anemometer is mounted at 3 meters off the ground, which can provide 3D wind measurements at 20 Hz.

4.5 Flight Test Results

To validate the proposed filters under the real world scenario, a flight test was performed on 04/07/2017. The flight test was conducted in the airspace close to a ground weather station which can provide 3D wind measurements at 20 Hz. During the flight test, the KHawk 55" UAV was manually controlled by the safety pilot. The flight trajectory and the location of the weather station are shown in Fig. 4.12.

Figure 4.11: US-KLS AmeriFlux weather station.

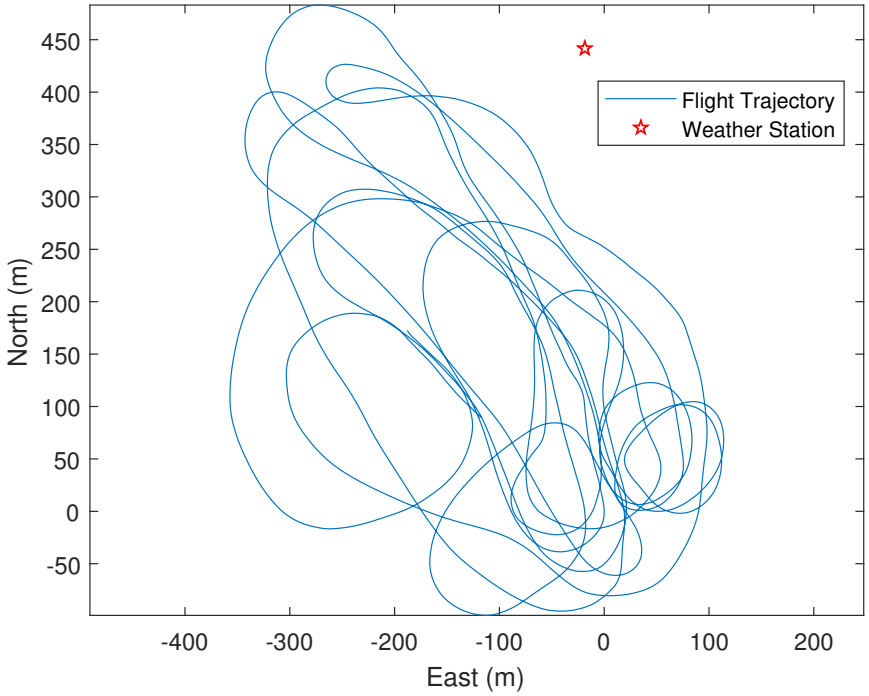

Figure 4.12: Flight trajectory.

Both 9-state EKF and 12-state EKF are implemented to estimate 3D wind $[w_n, w_e, w_d]$ in the NED frame. Because the downwind during the flight test does not contain significant sinusoidal

patterns, sinusoidal wave model is "switched off" by setting wind related initial states to zeros as discussed in previous section. Measurement noises and process noises with physical meanings are determined through experiments, while others are manually tuned. Similar to the simulation, the initial covariance $\mathbf{P}_0$ is assumed to be an identity matrix. Other parameters are shown in Table 4.3. Compared with the simulation results, the wind is less turbulent during the flight test, which results in significantly lower process noises of the filters.

Table 4.3: EKF initial conditions and tuning parameters for flight test

9-state EKF			12-state EKF		
Initial States	Process Noise	Measurement Noise	Initial States	Process Noise	Measurement Noise
$\mathbf{x_0}$	$\mathbf{Q}$	$\mathbf{R}$	$\mathbf{x_0}$	$\mathbf{Q}$	$\mathbf{R}$
15 (m/s)	0.0293 $(m/s^2)^2$	0.3633^2 $(m/s)^2$	15 (m/s)	0.0293 $(m/s^2)^2$	0.3633^2 $(m/s)^2$
0 (m/s)	0.0333 $(m/s^2)^2$	0.3215^2 $(m/s)^2$	0 (m/s)	0.0333 $(m/s^2)^2$	0.3215^2 $(m/s)^2$
0 (m/s)	0.0331 $(m/s^2)^2$	0.7698 $(m/s)^2$	0 (m/s)	0.0331 $(m/s^2)^2$	0.7698 $(m/s)^2$
0 (rad)	0.0041^2 $(rad/s)^2$	0.025^2 $(m/s)^2$	0 (rad)	0.0041^2 $(rad/s)^2$	0.025^2 $(m/s)^2$
0 (rad)	0.0045^2 $(rad/s)^2$	10^{-7} $(rad)^2$	0 (rad)	0.0045^2 $(rad/s)^2$	10^{-7} $(rad)^2$
0 (rad)	0.0045^2 $(rad/s)^2$	10^{-7} $(rad)^2$	0 (rad)	0.0045^2 $(rad/s)^2$	10^{-7} $(rad)^2$
0 (m/s)	10^{-4} $(m/s)^2$		0 (m/s)	10^{-9} $(m/s)^2$	
0 (m/s)	10^{-4} $(m/s)^2$		0 (m/s)	10^{-9} $(m/s)^2$	
0 (m/s)	10^{-4} $(m/s)^2$		0 (m/s)	10^{-9} $(m/s)^2$	
			0 (m/s)	10^{-7} $(m/s)^2$	
			0 (rad)	10^{-7} $(rad/s)^2$	
			0 (rad/s)		

The 3D wind estimates using 9-state EKF and 12-state EKF are shown in Fig. 4.13 and Fig. 4.14, respectively. Weather station measurements after smoothing with a 20-second moving average filter are shown as the ground truth for comparison purposes. As can be seen from Fig. 4.13, it takes the 9-state EKF roughly 50 seconds to converge. Once converged, the estimation results show a good match with measurements from weather station for the mean value. However, the proposed filter does not capture certain variances in the wind as it does in the simulation. This result comes as expected given the spatio-temporal characteristics of the wind since the wind anemometer and the UAV are not located at the same position. Similar to the 9-state EKF, the 12-state EKF is only able to capture the prevailing wind, as the sinusoidal wave model is "switched off". However, the 12-state EKF is expected to provide more accurate estimates under the wind conditions where sinu-

soidal patterns are dominant such as above the ocean surface and in the boundary layer [103, 104]. Error statistics for both filters are shown in Table 4.4.

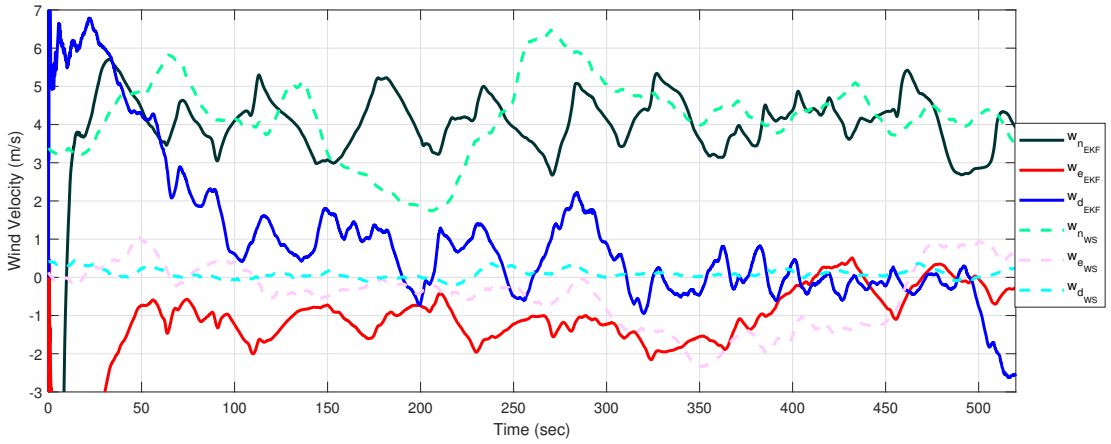

Figure 4.13: Estimated 3D wind using 9-state EKF vs. weather station measurements.

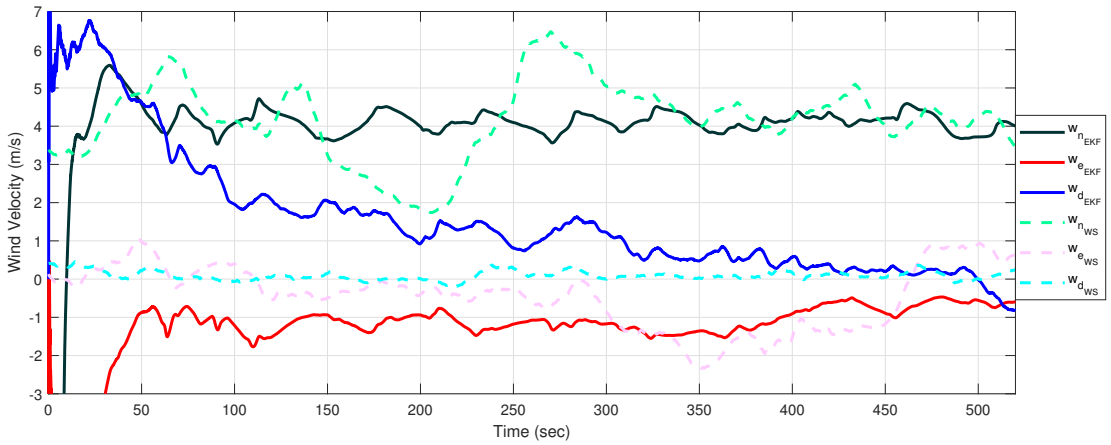

Figure 4.14: Estimated 3D wind using 12-state EKF vs. weather station measurements.

Table 4.4: error analysis of estimation results for flight test

	9-state EKF			12-state EKF		
	w_n	w_e	w_d	w_n	w_e	w_d
Mean Error (m/s)	0.8806	0.6939	0.8430	0.7815	0.8167	1.0427
Error Standard Deviation (m/s)	0.8016	0.4155	0.7046	0.6983	0.4812	0.8546

4.6 Conclusions

In this chapter, two novel EKFs (a 9-state EKF and a 12-state EKF) are proposed for the problem of 3D wind estimation. These two filters can be applied on small UAVs without direct flow angle measurements. Both filters are validated through simulations and flight tests. Results have shown that the proposed 9-state EKF provides a robust way to estimate the 3D prevailing wind while the 12-state EKF has the potential to estimate both prevailing wind and sinusoidal wave, which makes it desirable for UAV operations over ocean wave or forest fire. For the future works, the observability of proposed filters will be studied. More complex wind models such as the multi-sine model will be tested. Additionally, flight test in unsteady flow field will be conducted where sinusoidal patterns are dominant such as above the ocean surface.

Chapter 5

Wake Encounter Simulation and Flight Validation with UAV Close Formation Flight

Abstract

In this chapter, HawkWakeSim, a novel UAV wake encounter simulation platform, is presented with coupled modeling of aerodynamics and flight dynamics. Unlike conventional aircraft simulation models where aerodynamic coefficients are identified from flight test data, HawkWakeSim uses results from computational fluid dynamics calculations and updates the aerodynamic coefficients at each time step, which eliminates the errors from linearization. Several wake encounter scenarios with different lateral encounter angles and following clearances are simulated and investigated. The aircraft responses in one of the simulated scenarios are compared with experimental data obtained from a UAV close formation flight. Results from HawkWakeSim match the overall trend of flight test results, which show its effectiveness. Additionally, aircraft responses during wake encounters under different control configurations are simulated and analyzed.

5.1 Introduction

Aircraft wake encounters have been one major limiting factor for traffic management at major airports. In the near future, unmanned passenger and cargo aircraft will probably share the same airport as manned aircraft, which will greatly increase the chances of UAV wake encounters. On the one hand, wake vortices can be dangerous, because flying into the wake vortices generated

by another aircraft, especially a bigger aircraft, can potentially cause the loss of control of the following aircraft. This is why a minimum separation distance between two airplanes is enforced by FAA [110]. On the other hand, aircraft can benefit from wake vortex interactions by flying at a sweet spot, where the energy consumption of the following aircraft is significantly reduced compared with the leader aircraft [111, 112]. Both cases require an accurate and reliable wake simulator that can provide a reasonable estimate of aircraft responses while flying through the wake vortices at the near, mid, or far field. Previous researches on wake encounters are mainly focused on simulations and wind tunnel tests [113–115]. Only few groups successfully validated simulation results with experimental results using manned aircraft [63, 116, 117]. With the development of onboard avionics hardware as well as autonomous flight control algorithms, it is possible to achieve close formation flight with small UAVs. These new experimental platforms have great potentials to facilitate understandings of wake aircraft interactions.

In previous attempts of wake encounter simulation, several researchers used look up tables or databases generated from computational fluid dynamics (CFD) models [118] or flight test data [116, 119], while other researchers focused on computational methods [114, 115]. The problem with look up tables or databases is that the simulation results are valid only when the following two conditions are satisfied. First, the aircraft used in the simulation must have been included in the databases. Second, the aircraft has to be simulated under certain flight conditions. As for computational methods, different types of airplanes flying at different conditions can be easily simulated. There are several existing approaches for the simulation of wake induced effects. Dogan interpreted wake induced velocity as wind and directly used it as the input of flight dynamics simulator [114]. Saban used one-lifting line vortex lattice method and developed a simulator to study the aerodynamic interaction between airplanes during formation flight. However, the aircraft geometry is relatively simple and aircraft responses are not the main focus [115]. Fischenberg calculated wake induced forces and moments by using strip model and combined them with other forces and moments. The aircraft model used in the chapter is based on aerodynamic coefficients identified from flight test data around the trim point [63].

The objective of this chapter is to develop a trustable UAV simulation platform for wake detection, wake model validation, and eventually wake encounter alleviation or fuel saving. In order to simulate UAV wake encounters, aerodynamics simulator and flight dynamics simulator are incorporated. For wake encounter simulation and experiment, two Phastball UAVs were used, which were designed and built at West Virginia University (WVU). The air flow sensors installed on the nose cone of the fuselage were used as the major indicators of wake encounters. A variety of other sensors were also used for wake encounter detection.

The main contributions of this chapter are the introduction of HawkWakeSim, a novel wake encounter simulator with coupled aerodynamics and flight dynamics simulations, and the cross validation of the developed simulator using flight test data during UAV close formation flight. Unlike traditional aircraft simulation models where aerodynamic coefficients are identified from flight test data, HawkWakeSim uses results from CFD calculation and updates the aerodynamic coefficients at each step, which eliminates the errors from linearization. Another advantage of the proposed simulator is that different wind models (such as wake vortex, gust, and thermal) can be easily added in the CFD calculation, thus wind induced forces and moments are included in the aerodynamic coefficients. A good match can be observed from angle of attack (AOA) and angle of sideslip (AOS) reconstructed by HawkWakeSim and data measured during flight tests.

The organization of this chapter can be summarized as follows. The simulation and experimental platforms are first introduced in Sec. 5.2 and Sec. 5.3, respectively. Then, simulation results and flight test validation are presented in detail in Sec. 5.4 and Sec. 5.5. Finally, conclusions are made in Sec. 5.6.

5.2 HawkWakeSim: A UAV Wake Encounter Simulation Platform

HawkWakeSim is developed under MATLAB Simulink, which is an integration of flight dynamics and aerodynamics programs, shown in Fig. 5.3. Flight dynamics simulator can calculate forces, moments, as well as dynamics of the aircraft given the aerodynamics coefficients and initial conditions of the aircraft. The flight dynamic simulator used in this research is developed based on

the one introduced in Beard's book [4]. The simulator consists of two parts, a block that calculates forces and moments and a block that calculates the kinematics and dynamics of the aircraft. The block for forces and moments calculation contains gravitational forces, aerodynamic forces and moments, and propulsion forces and moments. Atmospheric disturbances are not considered in this block since they are handled by the aerodynamics calculation and included in aerodynamic coefficients. As for the kinematics and dynamics block, twelve non-linear ordinary differential equations describing the aircraft dynamics (also known as equations of motion) are implemented. The twelve states of the equations of motion are $[p_n, p_e, p_d]$, $[u, v, w]$, $[\phi, \theta, \psi]$, and $[p, q, r]$.

For aerodynamic calculations, a customized Tornado software is used. Tornado software is an open source aerodynamic software implemented in MATLAB using vortex lattice method [120]. It can calculate the aerodynamic coefficients given the aircraft geometry and flight conditions. In order to calculate the effects of wake vortex, the Tornado software is modified so that it takes atmospheric disturbances into account. Burnham-Hallock model is used as the wake vortex model for the aerodynamic calculations, shown in Eq. (5.1), where Γ_0 is the initial wake vortex strength, $r_c = 0.052 b_0$ is the vortex core radius, r is the radial distance to the vortex filament center line. Γ_0 can be calculated by Eq. (5.2), where W is the aircraft weight, ρ is the air density, S is the wing area, b is the wingspan, and V is the airspeed. The wake vortex decay is modeled by following Sarpkaya decay model [13] as shown in Eq. (5.3), where Γ_i is the vortex strength at a distance d from the initial wake vortex position, ε is the turbulence constant, $b_0 = 0.8b$ is the vortex span, and ω_0 is wake vortex descent speed [121].

$$\mathrm{w}_\theta(r) = \frac{\Gamma_0}{2\pi r} \frac{r^2}{r^2 + r_c^2}, \tag{5.1}$$

$$\Gamma_0 = \frac{W}{\rho S b V}, \tag{5.2}$$

$$\Gamma_i = \Gamma_0 \exp\left(\frac{-0.45 d \left(\varepsilon \Gamma_0\right)^{0.25}}{\rho V b_0} \right), \tag{5.3a}$$

$$w_\theta(r) = \frac{\Gamma_i}{2\pi r}\frac{r^2}{r^2 + r_c^2}, \tag{5.3b}$$

$$\omega_0 = \frac{\Gamma_0}{2\pi b_0}. \tag{5.3c}$$

Phastball UAV CAD model and mesh model used in Tornado software are shown in Fig. 5.1 and Fig. 5.2 [122], respectively. Details regarding the wake vortex model and vortex lattice method verification can be found in [122, 123].

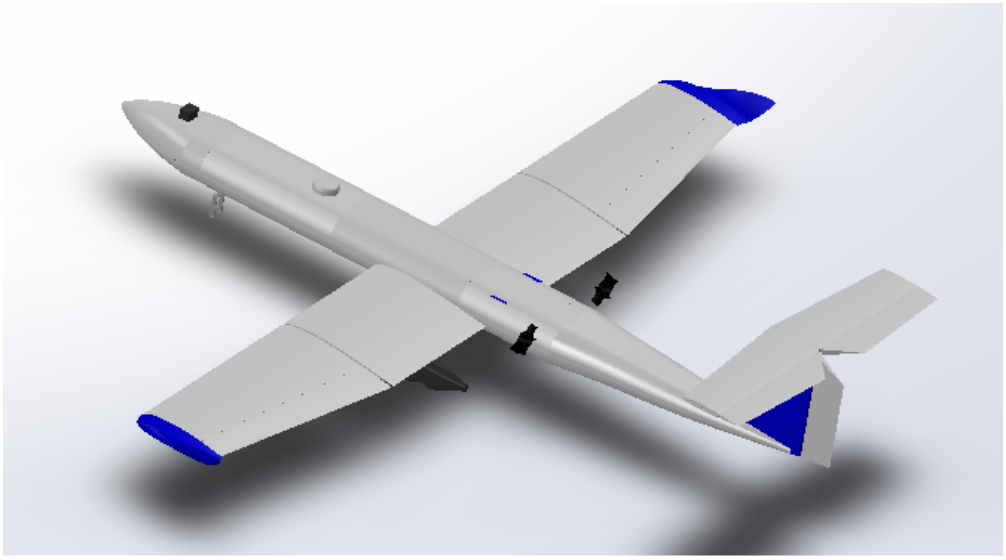

Figure 5.1: Phastball CAD model [122].

HawkWakeSim can simulate different wake encounter scenarios including different leader aircraft and visualize wake induced oscillations. It is also capable of simulating wake encounters during leader-follower close formation flight. The system diagram for HawkWakeSim is provided in Fig. 5.4, which illustrates how the aerodynamic simulator is integrated with the flight dynamics simulator.

Wake encounter simulation results presented in this chapter are generated through the implementation of a virtual leader aircraft, which is designed to fly at wings-level steady state. Meanwhile, the following aircraft is trimmed to fly at similar nominal situations with a different heading angle in order to simulate a lateral cut through, also known as lateral wake crossing. At each time step of the simulation, aerodynamic coefficients of the following aircraft, such as lift and

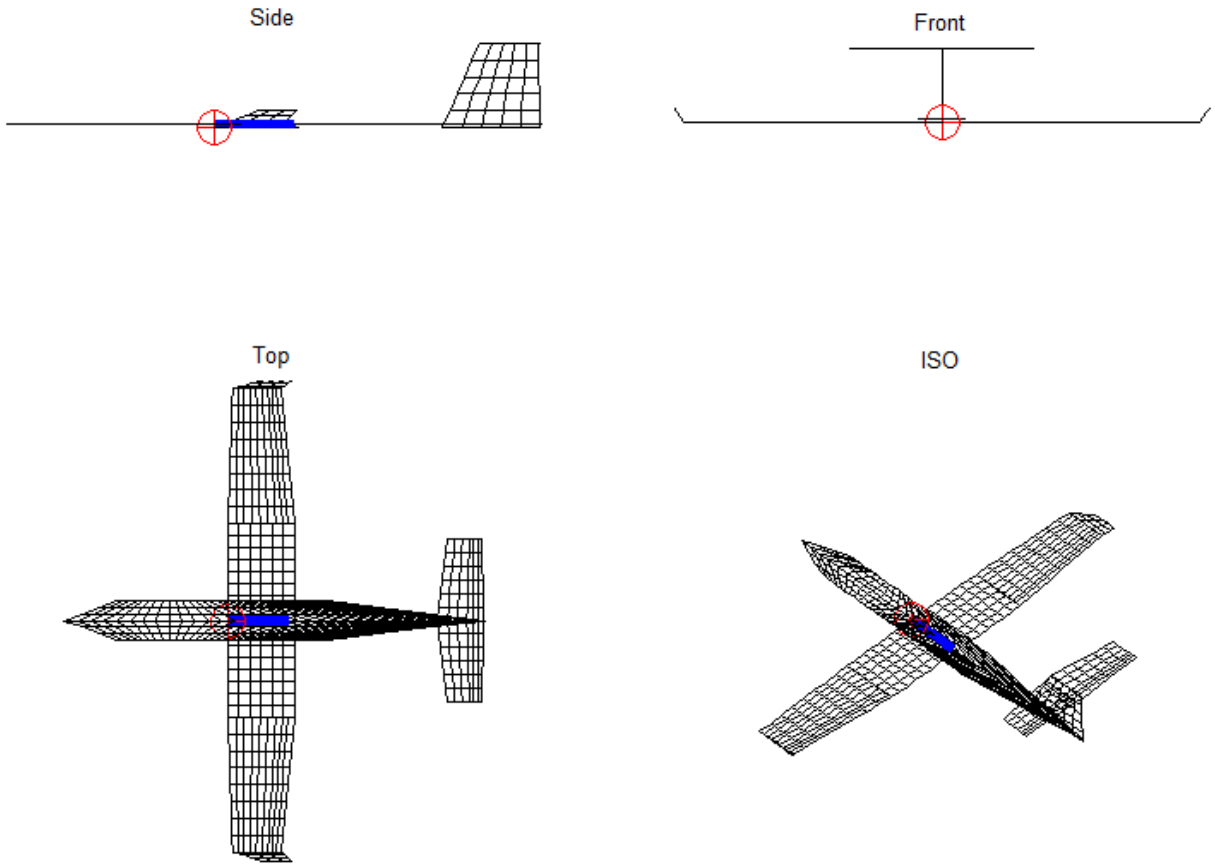

Figure 5.2: Phastball mesh model [122].

rolling moment coefficients are first updated in the flight dynamics simulator. These coefficients are calculated in the aerodynamics simulator at given conditions. Then, the states of the following aircraft, including airspeed triplets $[V, \alpha, \beta]$, attitudes $[\phi, \theta, \psi]$, positions $[p_n, p_e, p_d]$, accelerations $[a_x, a_y, a_z]$, rotation rates $[p, q, r]$, are updated based on forces and moments calculated from the flight dynamics simulator. In order to achieve the seamless integration of aerodynamics and flight dynamics simulation in MATLAB Simulink, Tornado software is modified so that it can run automatically during simulations. At the same time, two blocks are generated to serve as the bridge between aerodynamics and flight dynamics simulations. The first block is named as "Aerodynamics_Calculation", which is shown at the right part of Fig. 5.3. The inputs of this function are aircraft states, including airspeed, angle of attack, sideslip angle, rotation rates, and parameters used for wake vortex strength related calculation, such as longitudinal, lateral, and vertical distances be-

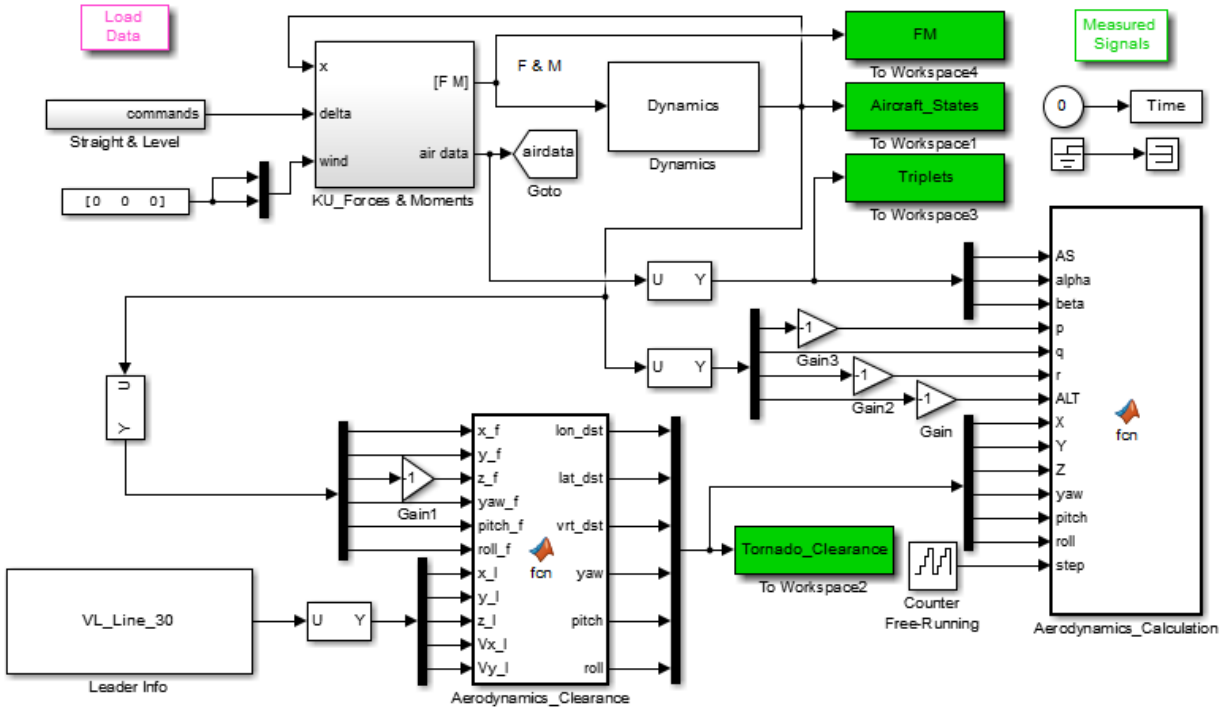

Figure 5.3: HawkWakeSim MATLAB Simulink model.

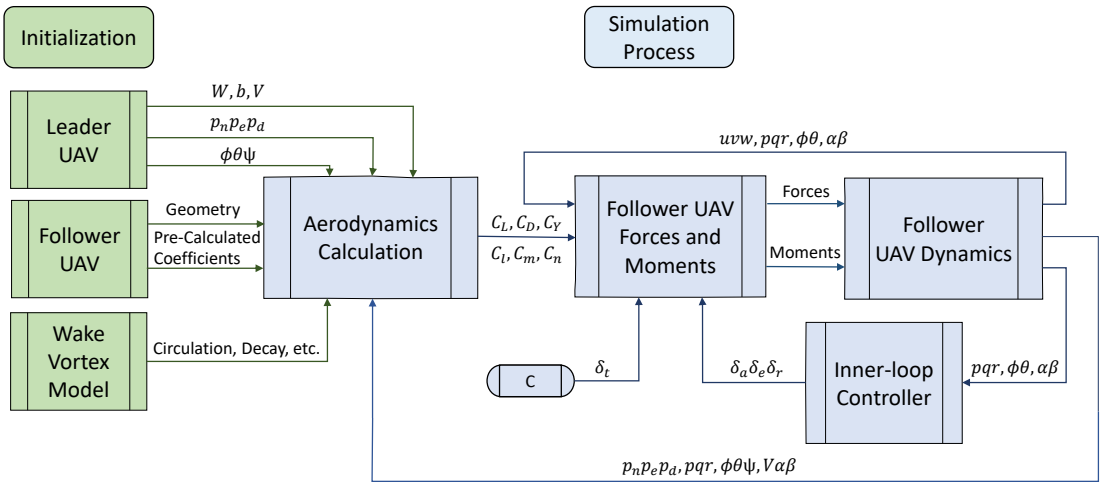

Figure 5.4: System diagram for HawkWakeSim.

tween the leader and follower, and relative orientation between the leader and the follower. These wake vortex strength related parameters are calculated by the second block, which is named as "Aerodynamics_Clearance". Once all these inputs are received, the "Aerodynamics_Calculation" function calls aerodynamics simulation program and feeds all the information. In other words, the wake induced oscillations are considered in the aerodynamic coefficients calculated in the aerodynamics simulation program. These coefficients are then updated in the flight dynamics simulation for forces, moments and aircraft states calculation, which eventually turns into attitude and position update of the following aircraft under the influence of wake vortex. Currently, HawkWakeSim is set to be running at 50 Hz. The running time of each simulation step is approximately 3 seconds when using a computer with Intel Xeon CPU E3-1226 v3 3.3 GHz and 16 GB RAM under MATLAB R2016b.

5.3 Experimental Platform

Phastball UAV, shown in Fig. 3.5, is the basis for the aerodynamic and flight dynamic simulations. The wingspan of the UAV is 2.4 meters and the chord length at the root is 0.35 meters. Detailed technical specifications can be found in Chapter 3 Table 3.2. Custom designed avionics were installed to collect data from sensors including Global Positioning System (GPS), inertial measurement unit (IMU), range sensor, etc. A NovAtel OEM-V1 GPS receiver was used for the ground velocity and position measurements (1.5 meters root-mean-square horizontal position accuracy, 0.03 m/s root-mean-square velocity accuracy). An ADIS-16405 MEMS IMU was used to measure rotation rates and linear accelerations. An extended Kalman filter (EKF) was running on an 800 MHz general-purpose computer (PC104) to provide real time attitude estimation at 50 Hz, with a typical error of less than 2 degrees for pitch and roll angles under dynamic circumstances [87].

Flight data were also collected from two angle of attack vanes and one sideslip vane attached to potentiometers with 10 V A/D at a 16-bit resolution, shown in Chapter 3 Fig. 3.5. A Pitot-tube was mounted on the nose boom of the aircraft along the longitudinal axis. The signals were sampled and logged at 50 Hz.

5.4 Simulation Results

5.4.1 Open-loop UAV Wake Encounter

In this subsection, open-loop simulation results from wake encounter with a 90 degrees lateral encounter angle is presented and discussed. Both the leader and following aircraft are trimmed to maintain steady level flight with no closed-loop flight controller present. The leader aircraft is commanded to fly to the north at an altitude of 100 meters, while the following aircraft is commanded to cut through both vortex cores generated by the leader aircraft. The flight trajectory is illustrated in Fig. 5.5. The follower is designed to cut through both vortex cores at 12 meters behind the leader aircraft, which is five times of the leader aircraft's wingspan.

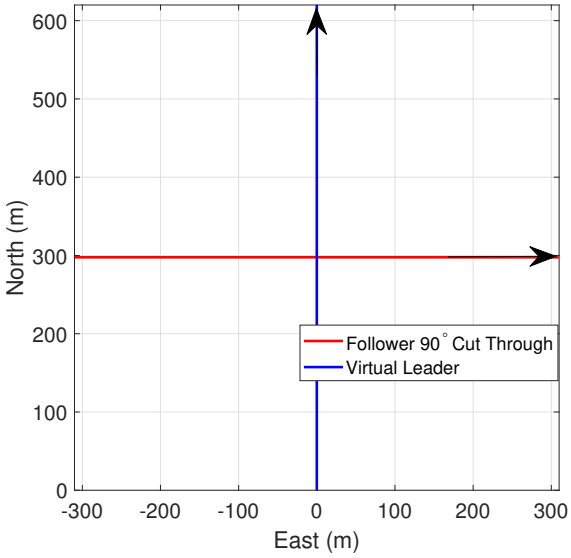

Figure 5.5: Flight trajectory of wake encounter simulation with 90 degrees lateral encounter angle.

In this simulation, both inertial and local AOA/AOS are reconstructed using inertial and local flow information. The simulated local AOA and inertial AOA are shown in Fig. 5.6. It can be observed that the wake encounter happened between 9.8 seconds to 10.2 seconds, and the inertial AOA of the following aircraft changed about 0.6 degrees during the wake encounter. However, the local AOA changed at a much larger magnitude. The AOS during 90 degrees wake encounter remains zero, thus not showing here. The difference between the inertial and local AOA/AOS is

caused by the local vortices and can be used for the identification of wake encounters [77]. Wake induced oscillations can also be observed from a_z and q, as shown in Fig. 5.7 and Fig. 5.8. It can be seen that a_z changes with a magnitude of 1.1 G and q changes with a maximum magnitude of 12 degrees/second.

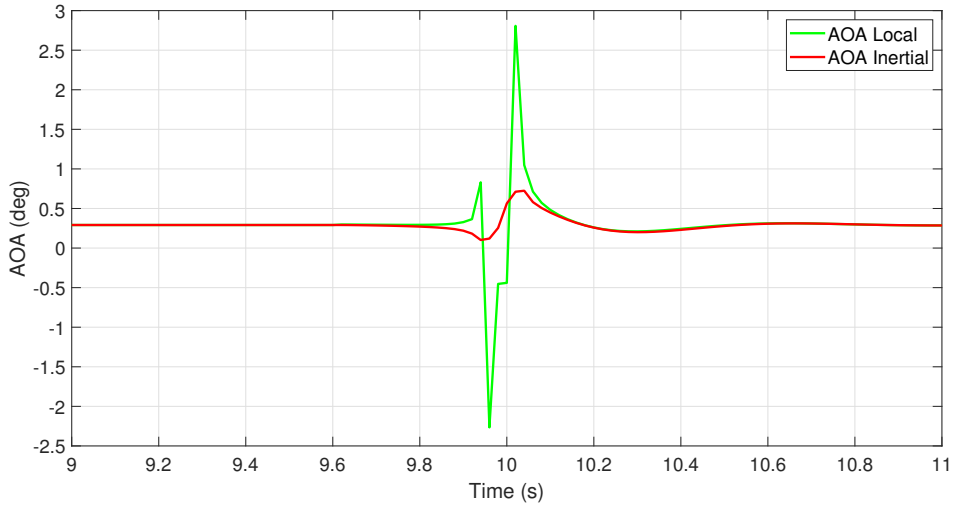

Figure 5.6: AOA of the following aircraft during wake encounter with 90 degrees lateral encounter angle.

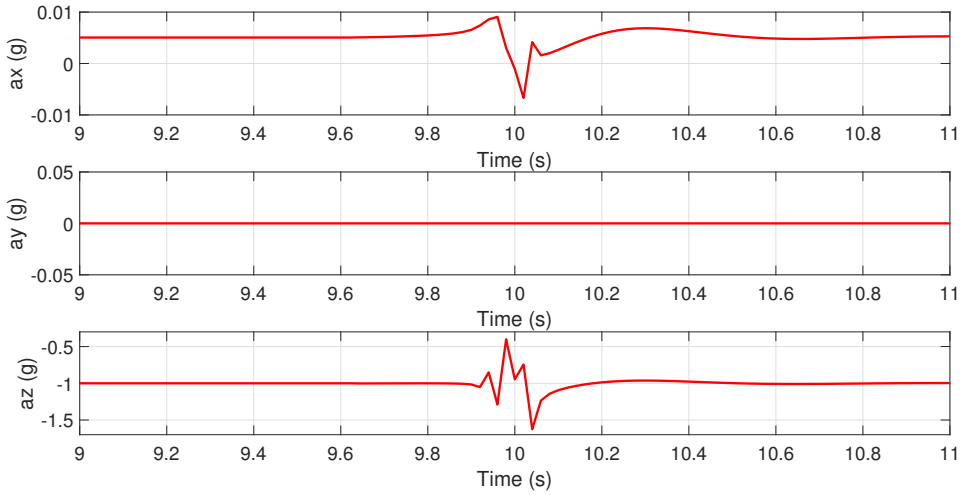

Figure 5.7: Accelerations of the following aircraft during wake encounter with 90 degrees lateral encounter angle.

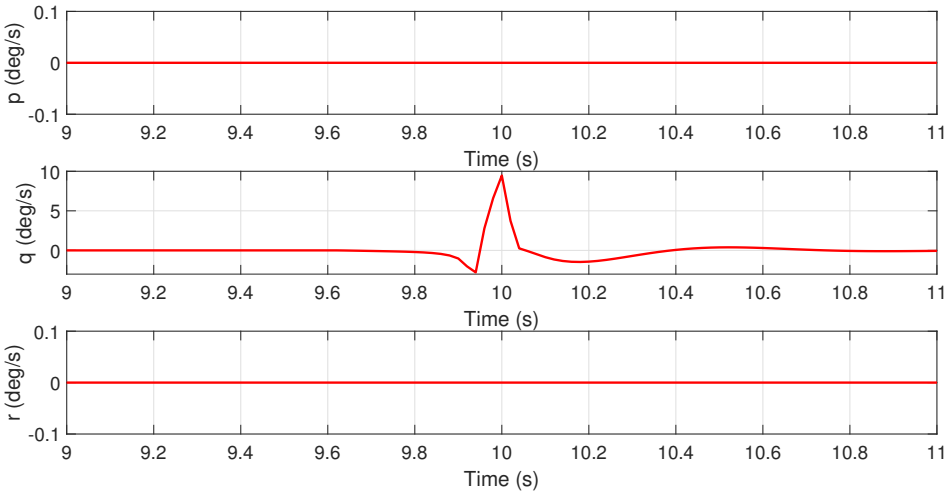

Figure 5.8: Rotation rates of the following aircraft during wake encounter with 90 degrees lateral encounter angle.

5.4.2 UAV Responses during Wake Encounter with Different Controller Configurations

One major application of wake encounter simulation is to support design of flight controllers for gust alleviation or wake surfing. In this section, wake induced aircraft oscillations during the leader-follower formation flight with different controller configurations are presented.

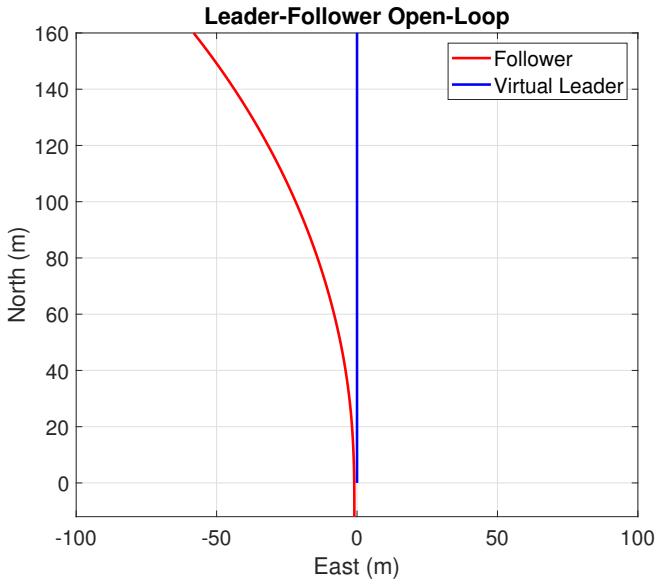

Figure 5.9: Leader-follower trajectories at trim condition: no control.

In this simulation, the following aircraft is initially placed 12 meters behind the leader and 1.2 meters at leader's left, to simulate the leader-follower formation flight. Two controller configurations are tested, including open-loop trim condition and inner-loop control case. The objective of the inner-loop controller is to fly the aircraft at zero roll and a constant pitch. The results of the open-loop case are shown in Fig. 5.9 and Fig. 5.10. It can be observed that under the influence of wake vortex generated by the leader aircraft, the following aircraft rolls to the left and drops over 15 meters altitude within 10 seconds.

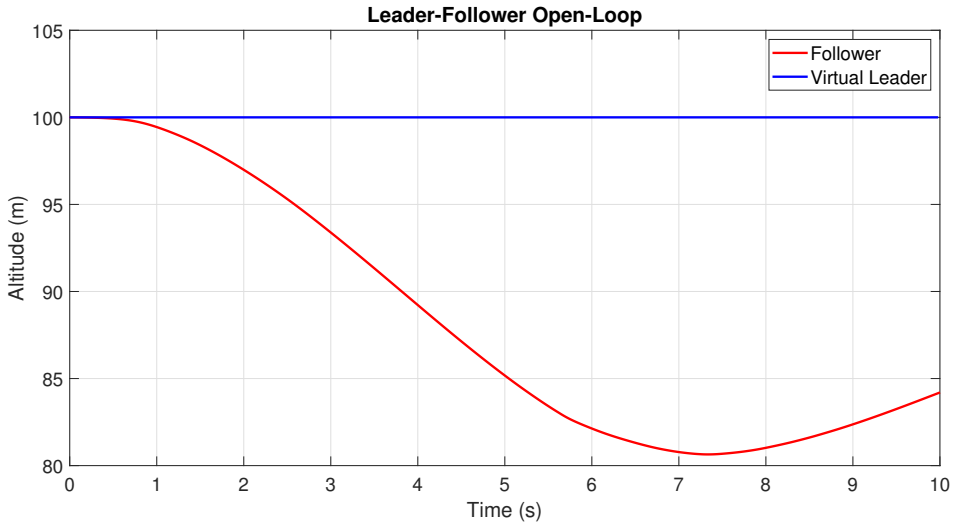

Figure 5.10: Leader-follower altitude at trim condition: no control.

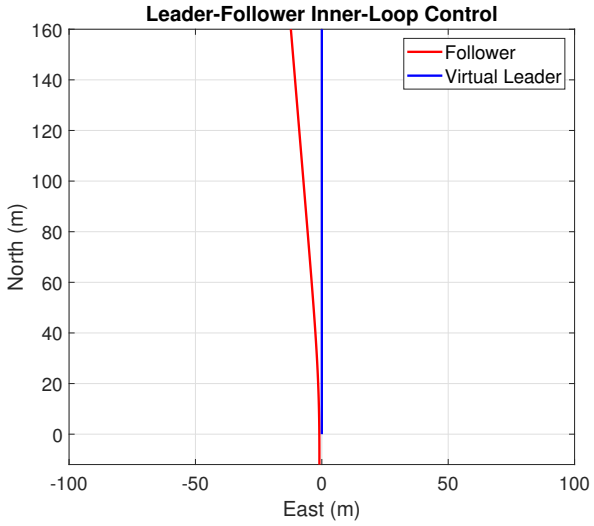

Figure 5.11: Leader-follower trajectories: inner-loop control.

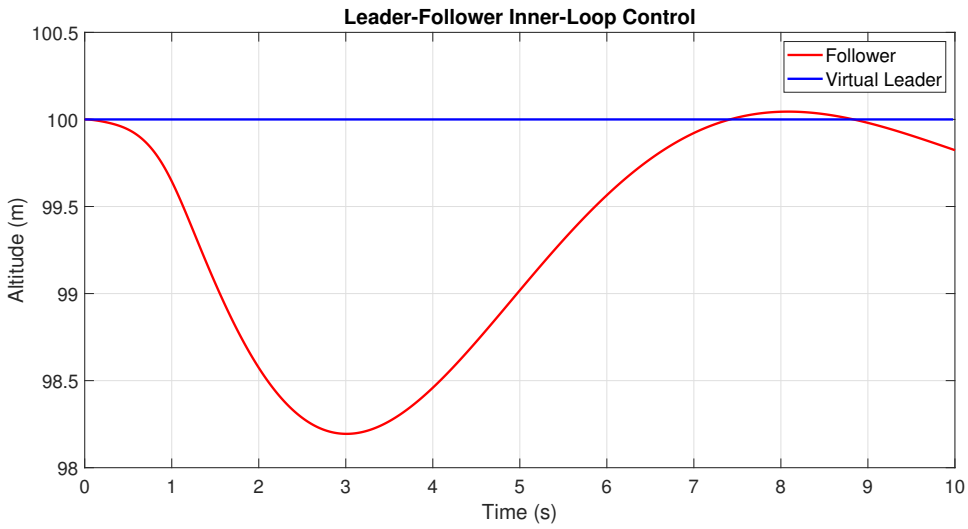

Figure 5.12: Leader-follower altitude: inner-loop control.

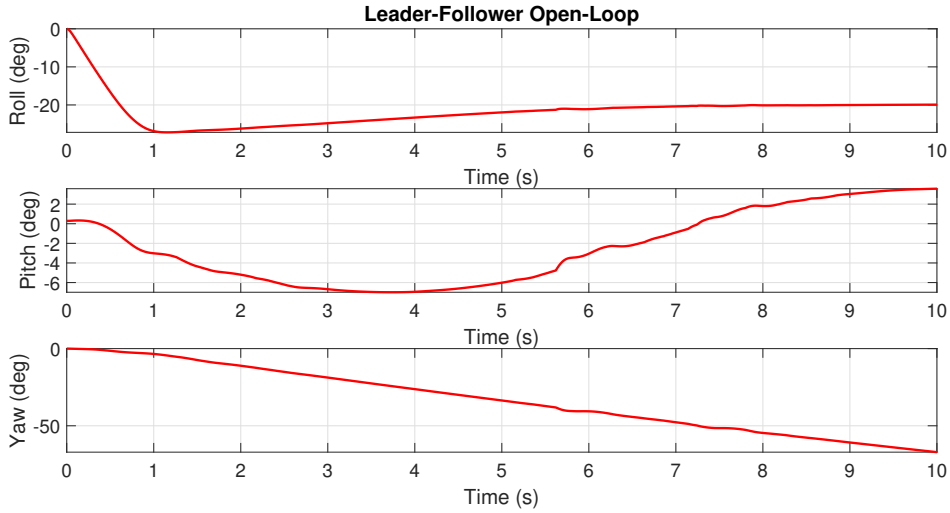

Figure 5.13: Euler angles of the following aircraft at trim condition: no control.

The performance of the following aircraft with the inner-loop controller is greatly improved compared with the open-loop case, shown in Figs. 5.11 - 5.14. Although slightly influenced by the leader's wake vortex in the beginning, the following aircraft successfully maintained its altitude and attitudes. The divergence of the flight course angle is because there is no course tracking controller within the inner-loop controller. Fig. 5.15 and Fig. 5.16 show the roll rates for both cases. Fewer changes in roll rate and quick recovery of roll angle can be observed from the inner-loop case, which shows the effectiveness of the controller for wake disturbance compensation.

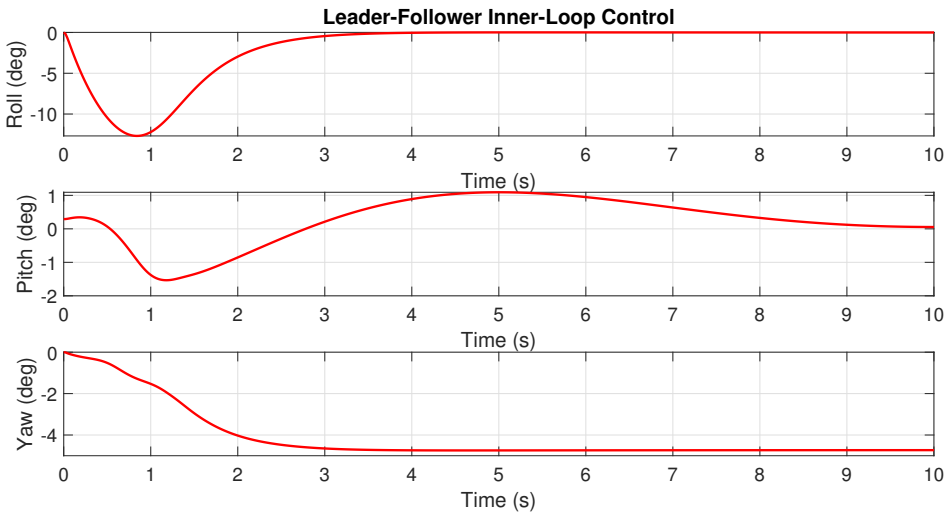

Figure 5.14: Euler angles of the following aircraft: inner-loop control.

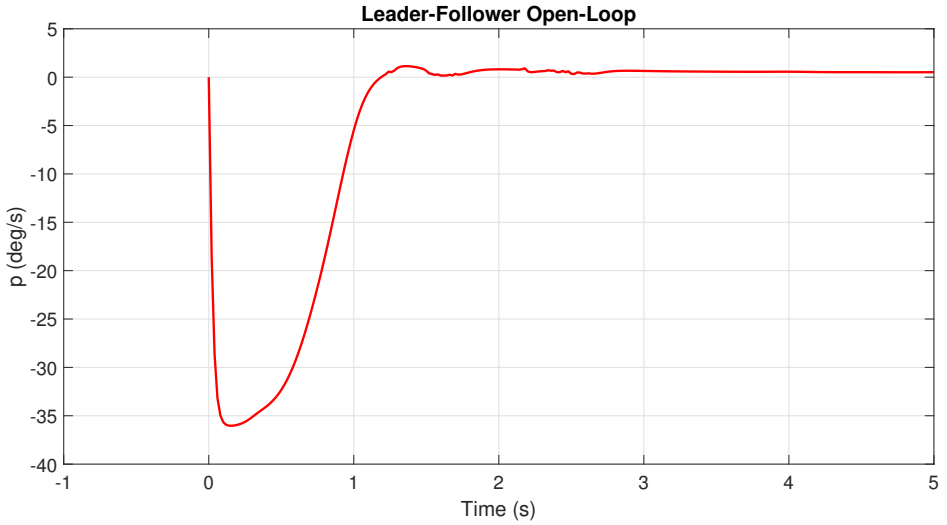

Figure 5.15: Roll rates of the following aircraft at trim condition: no control.

Control surface deflections for the inner-loop case are further shown in Fig. 5.17, which are good indications of wake strength. Note that oscillations caused by stronger wake vortices will require more control efforts to compensate. It can be seen that the major influence of the wake vortex on the following aircraft is the rolling moment as it requires 7 degrees of aileron deflection to compensate.

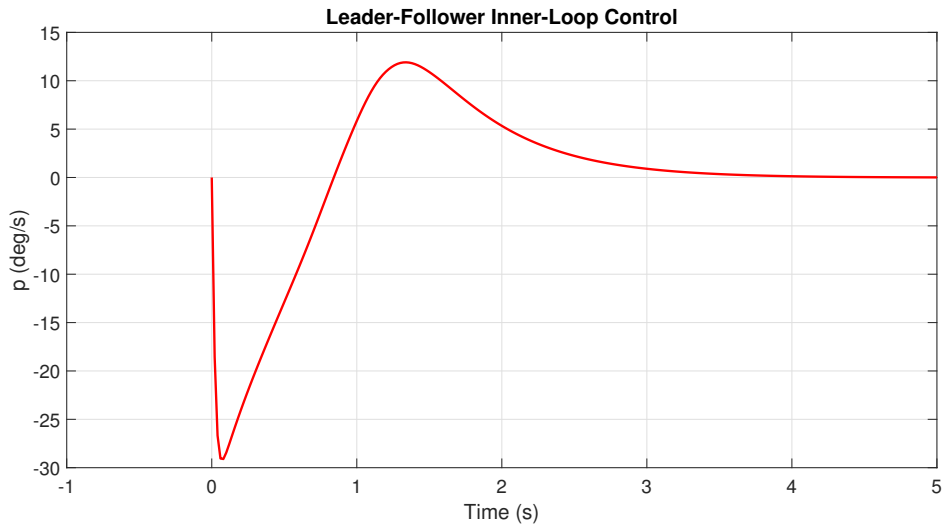

Figure 5.16: Roll rates of the following aircraft: inner-loop control.

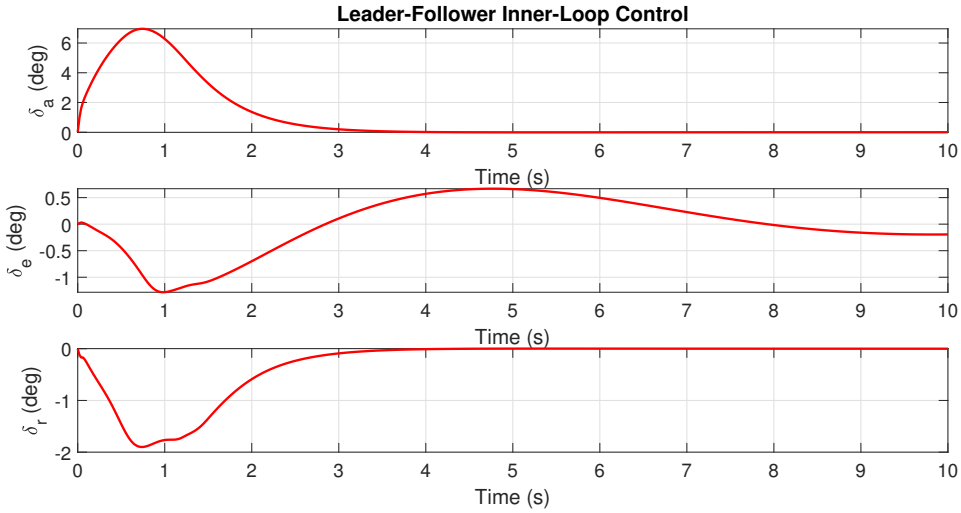

Figure 5.17: Control surface deflections of the following aircraft: inner-loop control.

5.5 Cross Validation with UAV Formation Flight Data

In this section, the simulation results generated by HawkWakeSim are compared with close formation flight results collected using two Phastball UAVs [51]. The WVU Phastball close formation flight results are discussed first. New criteria for Phastball UAV wake encounter identification are proposed based on air flow angle and inertial responses. Finally, comparison is made between HawkWakeSim results with flight test results.

5.5.1 Summary of Close Formation Flight

A total of 10 leader-follower formation flights were achieved at WVU in 2013 with different separation offsets in three flight sessions with the detail shown in Table 5.1 [51]. During all the flight tests, the leader aircraft flied in manual mode while the follower aircraft flied for about two minutes in autonomous formation tracking mode and the other two minutes in manual mode for takeoff and landing. All the formation flights are within the offsets of 5-20 wingspans. The objective for the first three formation flights was to test the controller performance. The longitudinal separation started from 20.8b for the first flight and was reduced to 12.5b for the third flight. The designed formation flight controller showed a max tracking error of 3 meters during straight legs [87]. After the confirmation of the controller performance, the longitudinal separation was further reduced to around 5b for a better chance of wake encounter during the last seven formation flights. Two different control modes were tried including fixed geometry and pilot-adjustable geometry. The latter mode allowed the pilot to change the separation offsets in real time based on observations from the ground. The wake was detected in three formation flights after the adjustment of the vertical tracking bias. A typical flight trajectory from one loop of formation flight is shown in Fig. 4.12. The trajectory includes two half circles with a turning radius of 120 meters and two straight legs with the length of about 450 m. Since the Phastball UAV has a cruise speed of 30 m/s, the maximum time for continuous wings level straight flight UAV is approximately 15 seconds.

Table 5.1: Summary of formation flight

Flight #	Desired Geometry Range (m)	Separation Adjustability	Corrections	Wake Encounter Detected
1/2/3	(50/40/30, 0, 0)	No	N/A	No
4	(24$\pm$12, $\pm$12, $\pm$12)	Yes	N/A	No
5	(12, 0, 0)	No	N/A	No
6	(24$\pm$12, $\pm$12, $\pm$12)	Yes	N/A	No
7	(12, -1.2, 0)	No	Vertical bias added	Yes
8	(12, -1.2, 0)	No	Vertical bias added	Yes
9	(24$\pm$12, $\pm$12, $\pm$12)	Yes	N/A	No
10	(12, -1.2, 0)	No	Vertical bias added	Yes

For this particular flight (the 7th flight), the follower UAV is commanded to maintain a 12

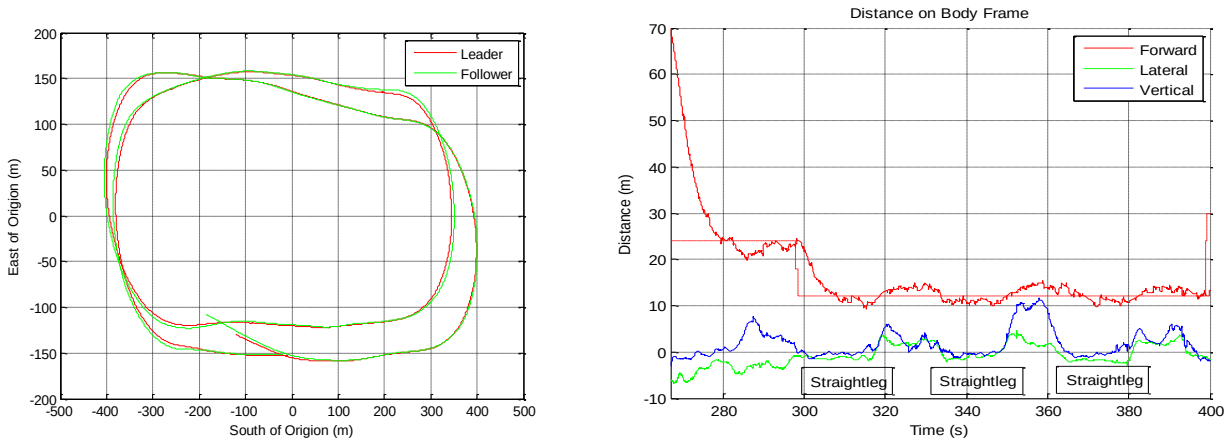

Figure 5.18: Trajectory for formation flight and tracking performance.

meter longitudinal offset from the leader's center of gravity (CG), a 1.2 meter lateral offset on the left of the leader's CG, and a zero vertical offset. The tracking performance in autonomous mode is shown in Figure 7 with the red dash line representing desired forward clearance.

5.5.2 Wake Encounter Identification

Although there have been former formation flight tests using UAVs, no prior results exist using close UAV formation for wake encounter tests. In fact, it is quite challenging to identify the wake encounter from small UAV flight data due to the limitations from onboard sensors as well as disturbances caused by ambient wind gusts. The three air flow sensors mounted on the fuselage of Phastball UAVs could be used as indications of wake encounters. However, these air flow measurements are also corrupted with sensor noises and local gust disturbances. Because only the wings-level straight flights are of interest, the difference between the left and right fuselage mounted AOA sensors is used as the major indicator of wake encounter after compensating for the measurement noise. Specifically, the wake encounter period is chosen when the difference between the two AOA sensors goes out of the 3σ range of the nominal values, where σ is the standard deviation of the difference. It can be observed from Fig. 5.19 that only several cases were detected from this flight where the AOA difference went over the 3σ blue lines. And only one of them happened during wings level straight fight. Wake effects are also observed from other sensor

measurements including gyros, AOS, accelerometers, which are shown in detail in Figs. 5.20-5.23.

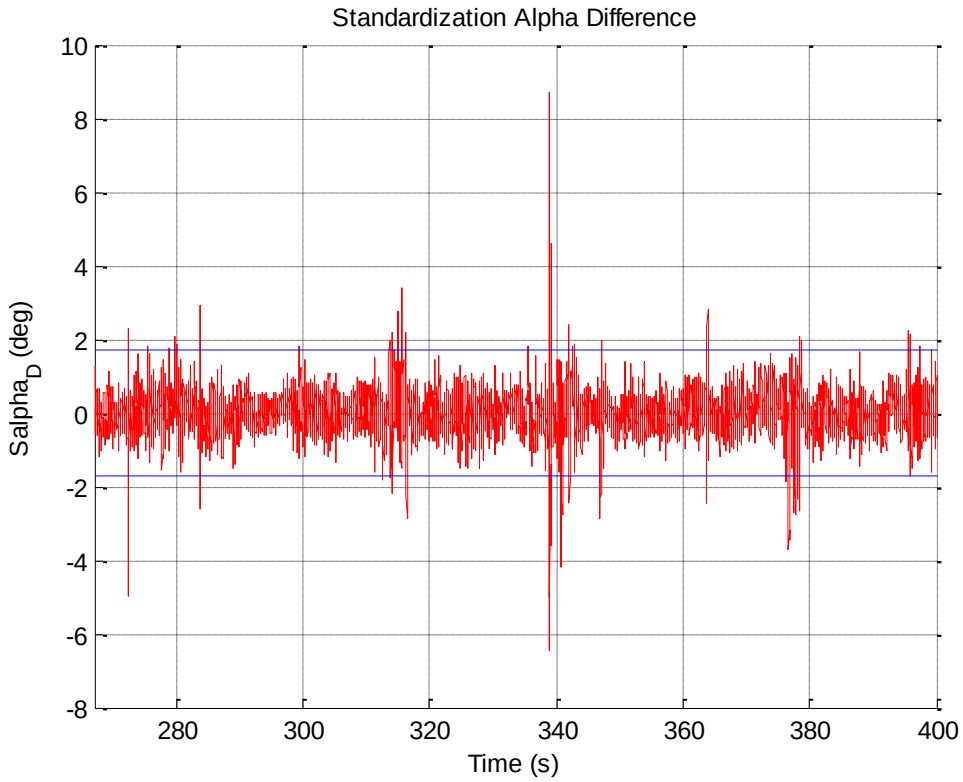

Figure 5.19: Difference between left and right AOA sensors.

The above wake encounter identification method is used for all the close formation flight data in this effort. The results are shown in Table 5.2. The four wake encounters all happened at the longitudinal offset of 10-14 meters (approximately 5 wingspans). The wake vortices of the leader hit first on the left vane during the 7th flight and hit first on the right vane during the 8th flight.

Table 5.2: Wake encounter flight summary

Flight #	Commanded Clearance (m)	Wake Hit Vane	Total Formation Flight Time	Wake Encounter Period
7	(24/12, -1.2, 0)	Left-Right Vane	267-400 sec	338.8-340 sec
8	(30/18/12, -1.2, 0)	Right-Left Vane	117-380 sec	181-181.3 sec
9	(30/12, -1.2 - 10.8, -6 - 0)	None	267-400 sec	None
10	(36/12, -1.2, 0)	Right Vane	89-334 sec	237.5-237.8
10	(36/12, -1.2, 0)	Right Vane	89-334 sec	239.3-239.7

All the detailed flight data from the first wake encounter is shown in Fig. 5.20 and Fig. 5.21,

together with all the other data during one straight leg (13 seconds). Wake encounter period is identified from wings level flight based on the difference between the left and right AOA sensors. The threshold is chosen as $\pm 3\sigma$ range of the nominal AOA difference for each flight in consideration of single AOA sensor measurements. It is interesting to point out that the wake effect can also be observed from other sensors as well. The following behaviors have been observed from Fig. 5.20 and Fig. 5.21 during the first wake encounter of Phastball UAVs.

1. Difference between left AOA and right AOA is greater than 3σ (1.7142 deg);
2. Abrupt movements of sideslip angle sensor (> 5 deg.);
3. Abrupt rolling after the wake encounter (roll oscillation and aileron corrections after wake encounter);
4. Consequent vertical motions observed from accelerometer measurements (-1.6 G).

The abrupt negative rolling during the wake encounter is due to the fact that the follower aircraft encounter the downdraft of the wake mostly from the left wing.

The second wake encounter data is shown in Fig. 5.22 and Fig. 5.23 including all the data during the straight leg. Similar behaviors have been observed from the onboard sensors.

1. Difference between left AOA and right AOA greater than 3σ (1.7142 deg);
2. Abrupt movements of sideslip angle sensor (> 5 deg);
3. Abrupt rolling after the wake encounter (-30 deg/sec roll rate);

The flight path of the follower aircraft during wake encounters has also been looked into. The first two wake encounters center around the theoretical value of the wake location. However, such results have a strong assumption on the GPS accuracy, which may not be accurate for the NovAtel GPS used in this effort. Differential GPS or post processed GPS data with cm level accuracy is needed for a thorough investigation.

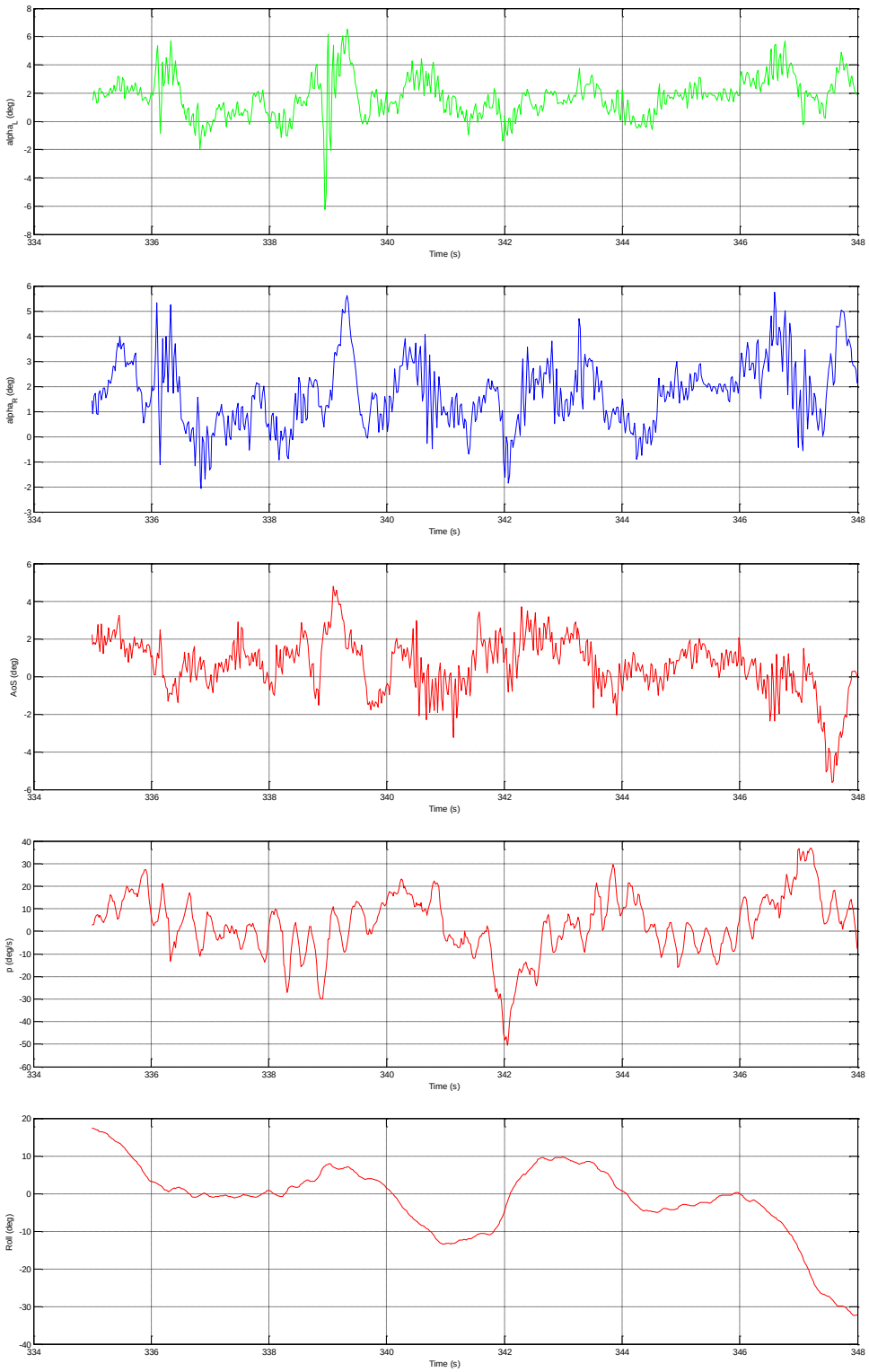

Figure 5.20: Measurements $[\alpha_L, \alpha_R, \beta, p, \phi]$ during wake encounter 1 (338.8-340 sec.).

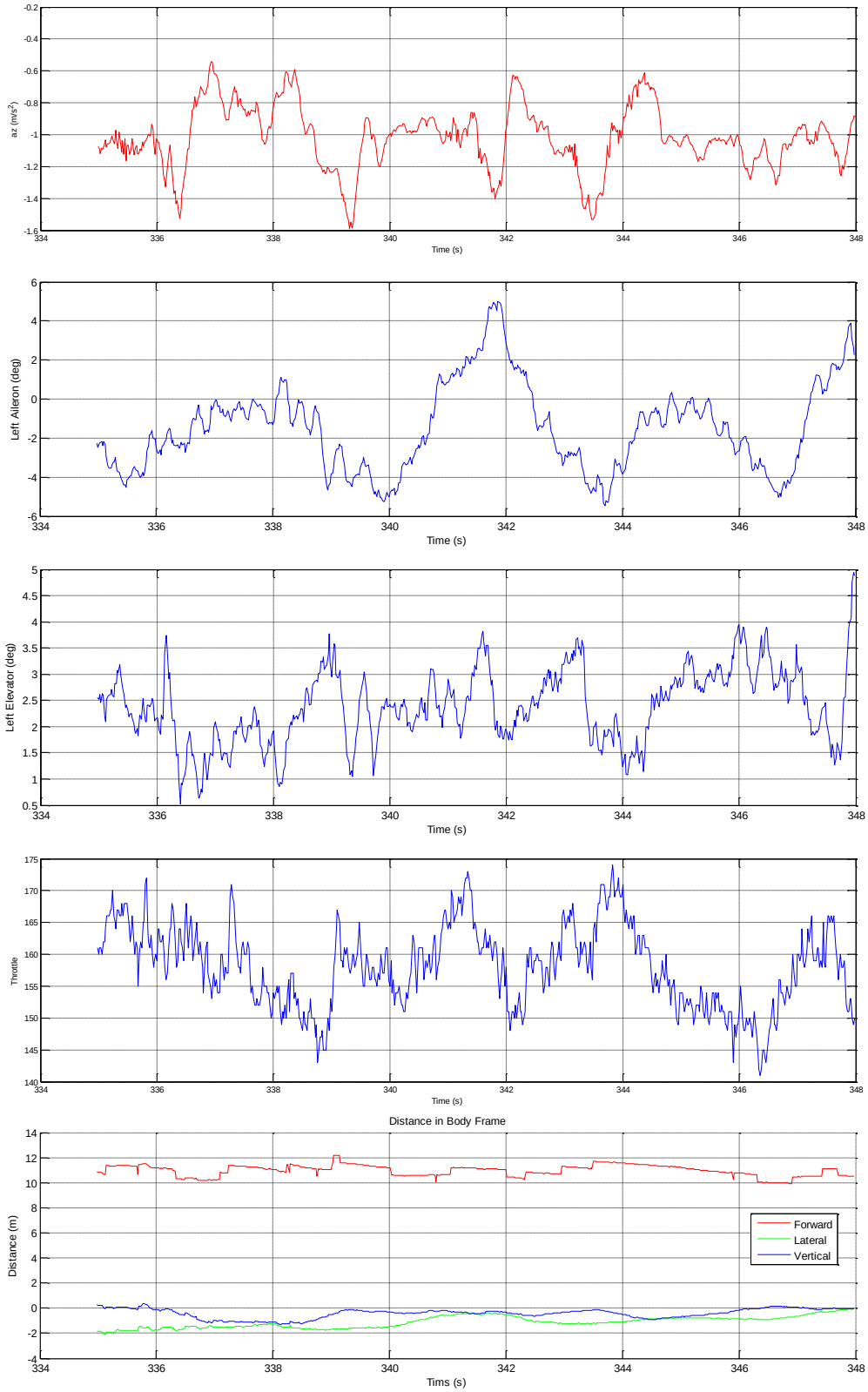

Figure 5.21: Measurements $[a_z, \delta_a, \delta_e, \delta_t, l, f, h]$ during wake encounter 1 (338.8-340 sec.).

5.5.3 Comparison between HawkWakeSim and Flight Test Results

The wake encounter period used for comparison is between 338.8 to 339.2 seconds from the 7th flight. For cross validation purpose, wake encounter with a 20 degrees lateral encounter angle is simulated to approximate the actual flight test scenario. In the simulation test, the following aircraft cut through both vortex cores generated by the leader aircraft. The flight trajectories for both simulation and flight test are shown in Fig. 5.24 and Fig. 5.25. The flight test trajectory is plotted based on onboard GPS data from both leader and following aircraft.

The wake encounter durations in both simulation and flight test are approximately the same as can be seen from the AOA changes, shown in Fig. 5.26 and Fig. 5.27. Similar to the 90 degrees encounter simulation, it can be observed from the red line in Fig. 5.26 that the inertial AOA of the following aircraft changed during the wake encounter, however, with a larger magnitude up to 1.8 degrees. This is because at a smaller lateral encounter angle, the following aircraft stays in the wake vortex field longer than those cases with bigger lateral encounter angles. The blue line in Fig. 5.27 shows the local AOA measurements from the left flow vane on the following aircraft during the flight test. The red line is inertial AOA reconstructed from flight test data using output minimization method [77]. It can be observed that local AOA goes up to 8 degrees during wake encounter in real flight, which is much bigger than inertial AOA from the simulation. This is because that the AOA measurement during the flight test is the local AOA measured by AOA vane. As described in a former section, a fair comparison can be made by adding the local wake induced AOA, as shown in green. After the correction, a similar trend of AOA movements with less magnitude difference can be observed from both simulation and flight test.

Unlike the 90 degrees wake encounter case, the AOS changes during the 20 degrees wake encounter, as can be observed in Fig. 5.28 and Fig. 5.29. However, the magnitude of the AOS in the simulation is much smaller than the measurements during flight test.

The difference in the magnitude of local AOA/AOS from simulation and flight test may be caused by the difference in cut-through trajectories, approximations employed in the CFD model, flight test data quality, or the difference of wake strength. One explanation is that the vortex model

used in the simulation might not be as strong as the real wake vortex. This difference can be reduced by tuning the parameters in the wake model, which can potentially help identify a more accurate wake model for small UAVs. One example is shown in Fig. 5.30 and Fig. 5.31, where the circulation strength of the wake vortex is increased by five times. A significant increase of local AOA and inertial AOA can be observed from Fig. 5.30. Similarly, the inertial AOS can be corrected by adding in local wake induced AOS, which is shown in Fig. 5.31. This example shows HawkWakeSim can be used to simulate wake encounters with different wake vortex strengths, in other words different leader aircraft.

Wake induced oscillations can also be observed from simulation result of a_z (with a magnitude of 0.7 G), as shown in Fig. 5.32. The major difference between 90 degrees encounter case and 20 degrees encounter case appears in the rotation rates of the following aircraft. It can be seen from Fig. 5.34 that wake induced oscillations can be observed from all three rotation rates instead of only q in the 90 degrees case. As shown in the first row of Fig. 5.34 and Fig. 5.35, the roll rate during wake encounter in the flight test match with the simulation result well, both with a magnitude around 50 degrees/second. In both simulation and experiment, wake encounters with a small lateral encounter angle (<=30 degrees) from the left of the leader aircraft will cause the following aircraft to slightly roll right and then aggressively roll left.

5.6 Conclusions and Future Work

This chapter introduces a novel UAV wake encounter simulation platform, which matches with UAV wake encounter data during close formation flight. In order to simulate UAV responses during wake encounters, both aerodynamics and flight dynamics simulations are incorporated. The capability of the developed wake encounter simulator is confirmed through the comparison of simulation results and experimental results. The simulation results match the overall trend of the flight test results. Future work will focus on the integration of formation flight controller, the validation using different leader aircraft, and the refinement of new UAV wake vortex models.

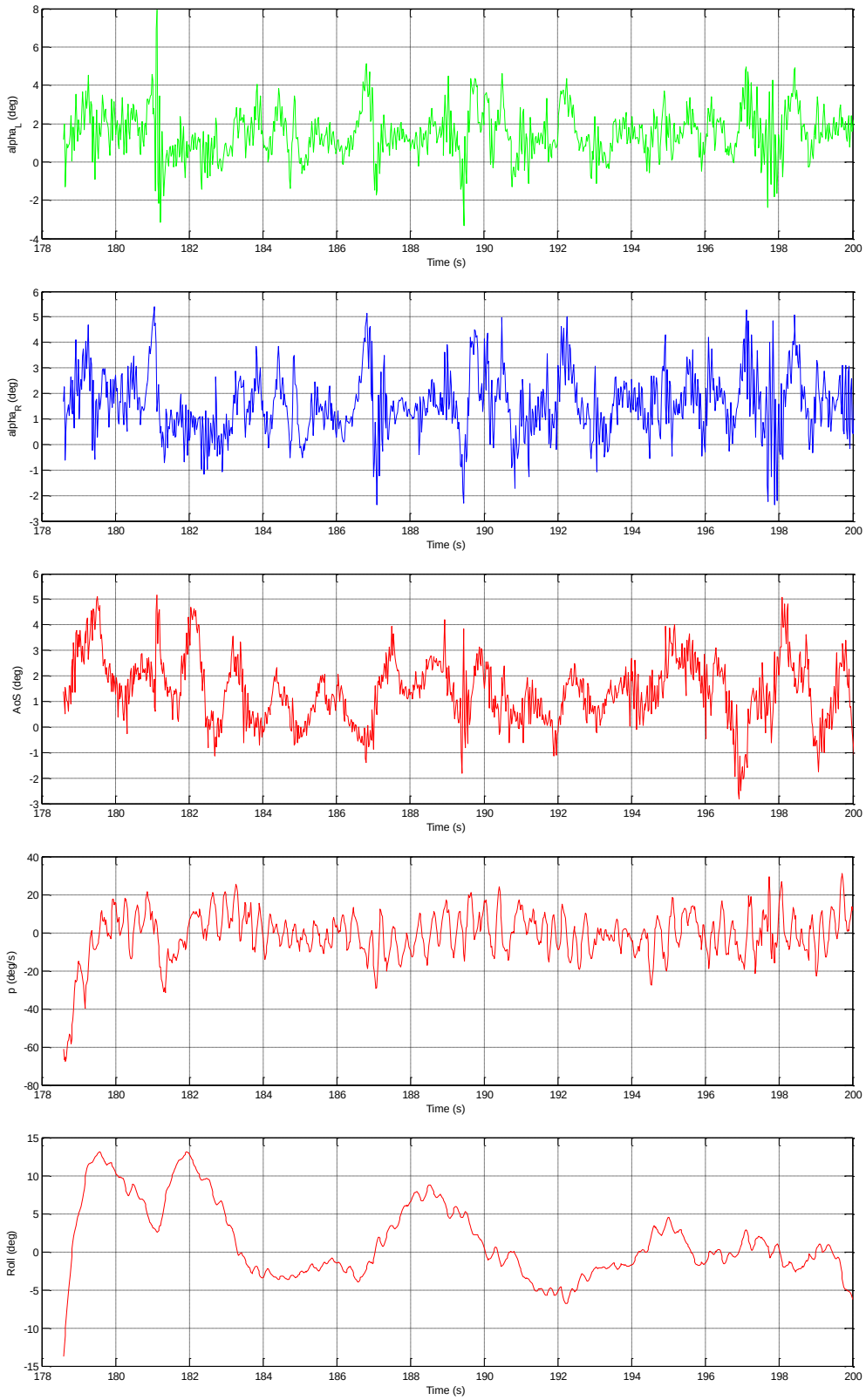

Figure 5.22: Measurements $[\alpha_L, \alpha_R, \beta, p, \phi]$ during wake encounter 2 (181-181.3 sec.).

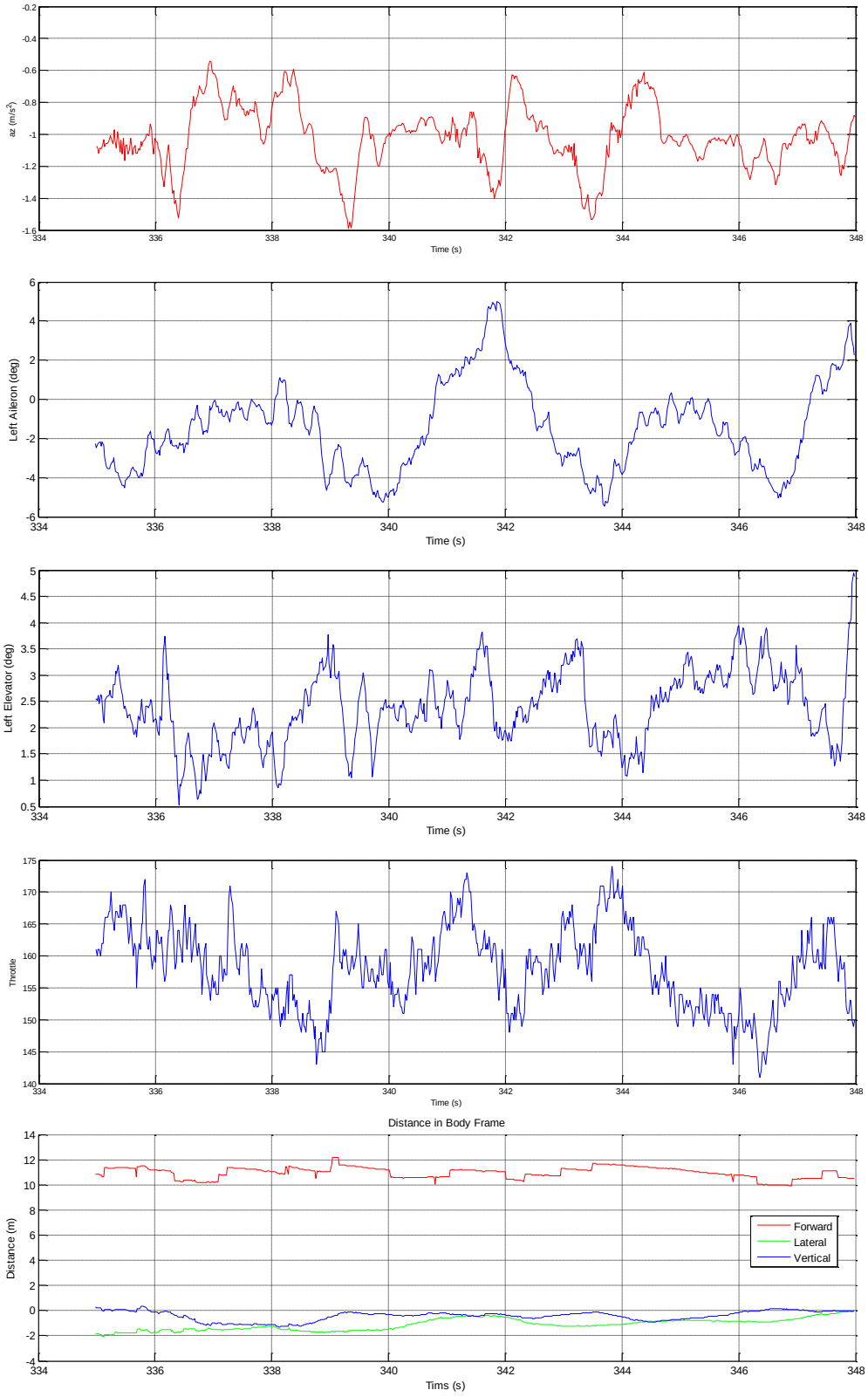

Figure 5.23: Measurements $[a_z, \delta_a, \delta_e, \delta_t, l, f, h]$ during wake encounter 2 (181-181.3 sec.).

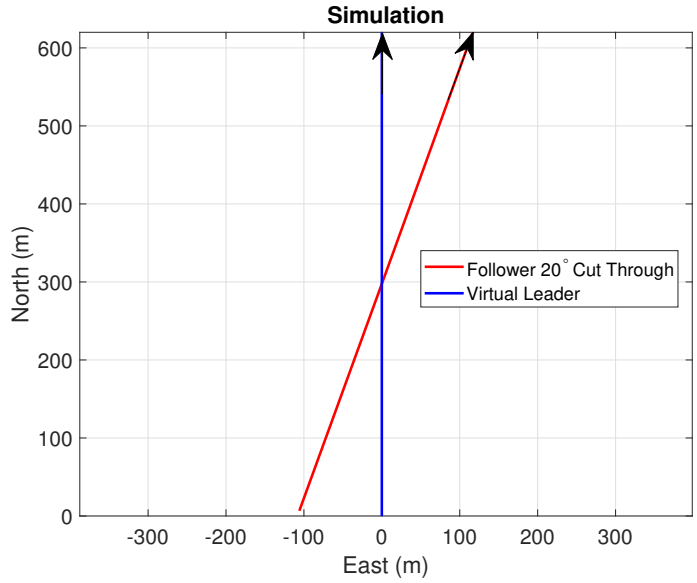

Figure 5.24: Flight trajectories of wake encounter: simulation.

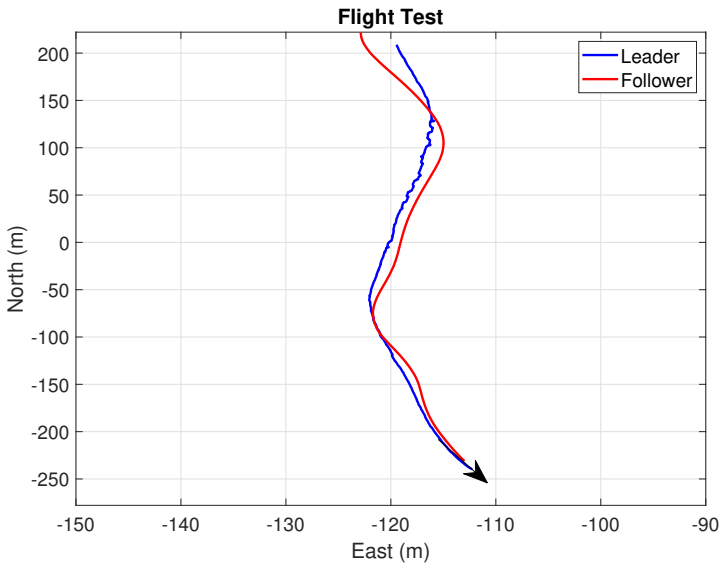

Figure 5.25: Flight trajectories of wake encounter: flight test.

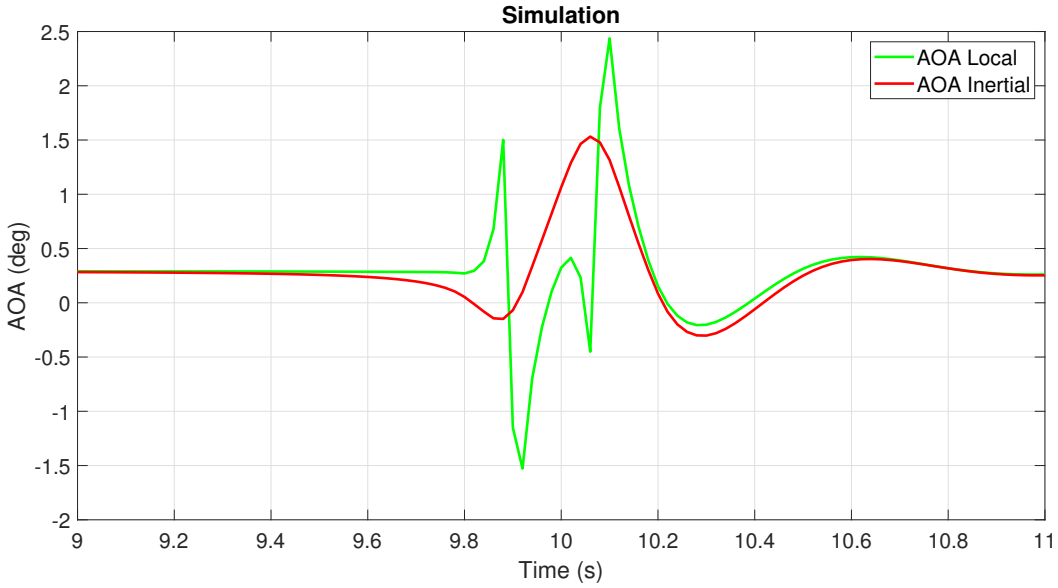

Figure 5.26: AOA of the following aircraft during wake encounter: simulation.

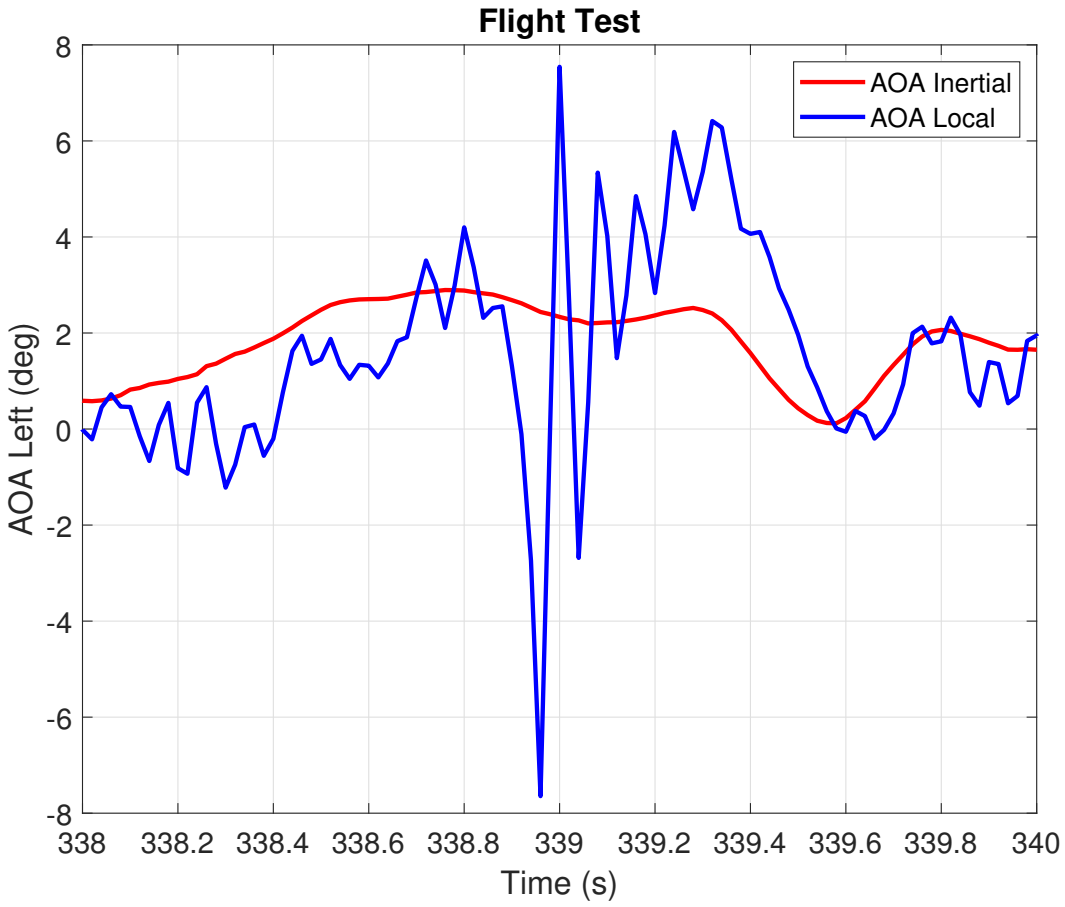

Figure 5.27: AOA of the following aircraft during wake encounter: flight test.

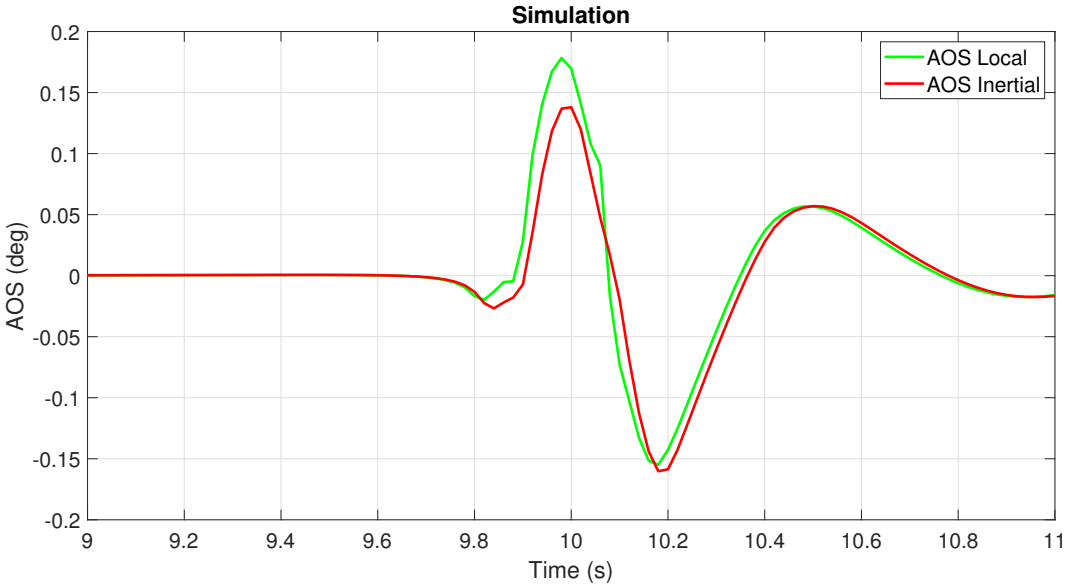

Figure 5.28: AOS of the following aircraft during wake encounter: simulation.

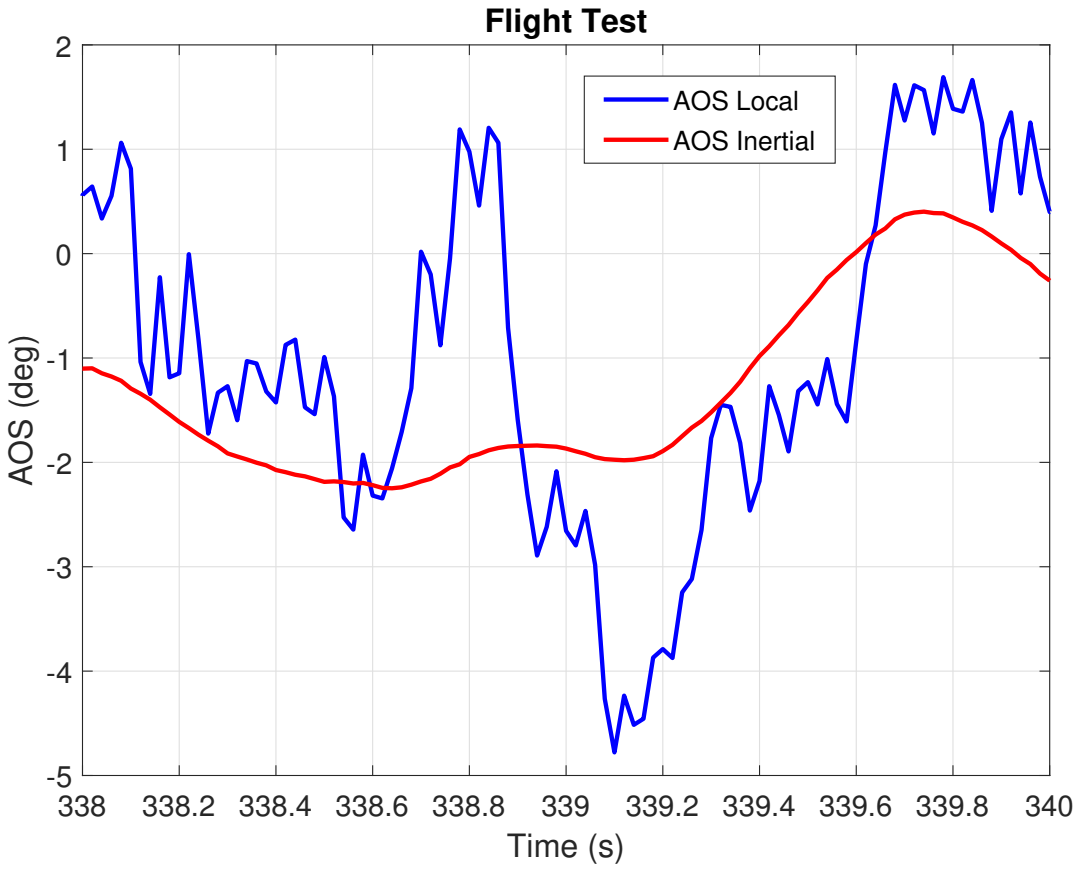

Figure 5.29: AOS of the following aircraft during wake encounter: flight test.

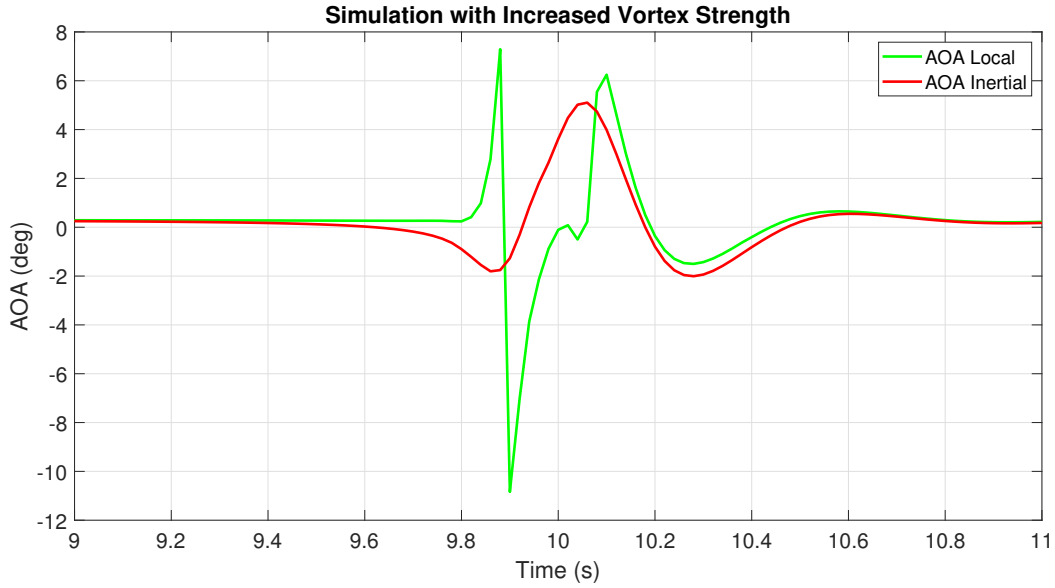

Figure 5.30: AOA of the following aircraft during wake encounter with stronger strength

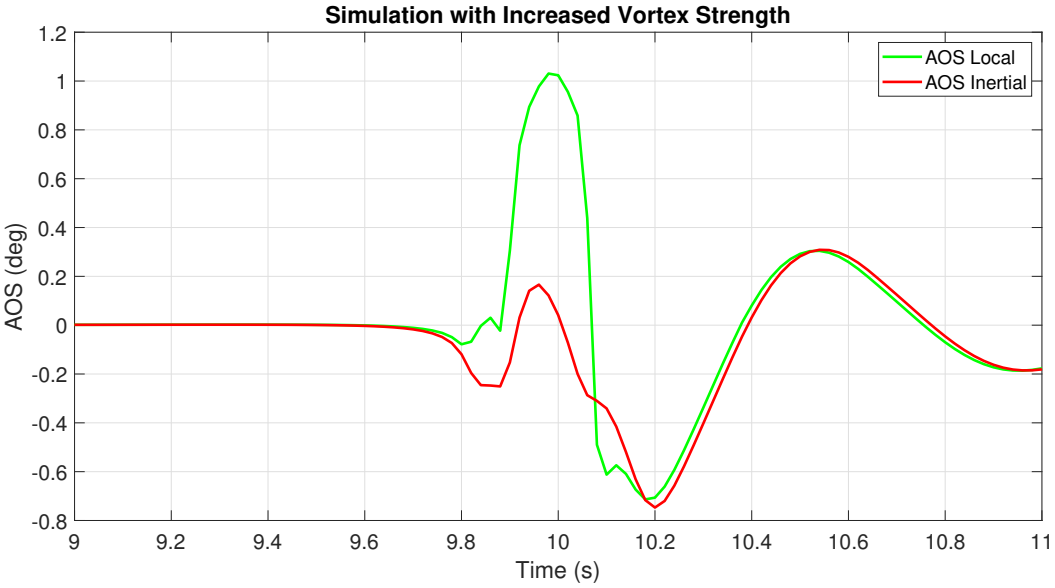

Figure 5.31: AOS of the following aircraft during wake encounter with stronger strength.

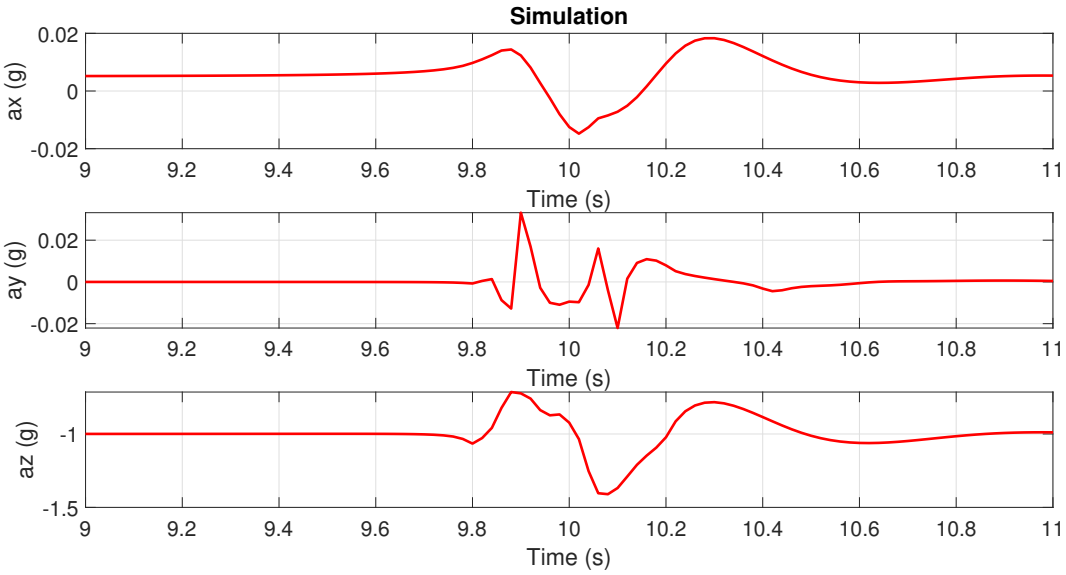

Figure 5.32: Accelerations of the follower during wake encounter: simulation.

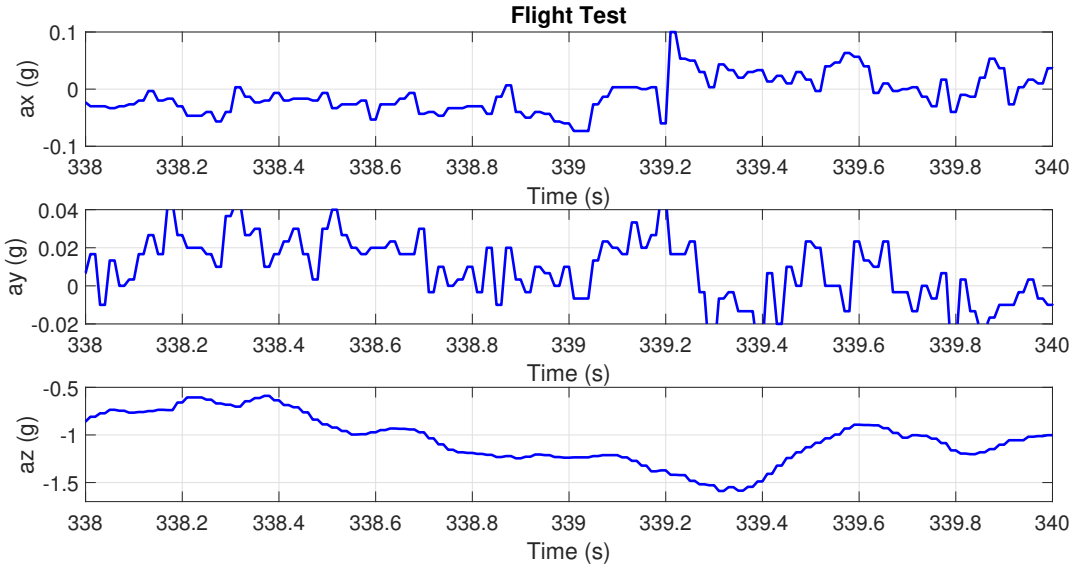

Figure 5.33: Accelerations of the follower during wake encounter: flight test.

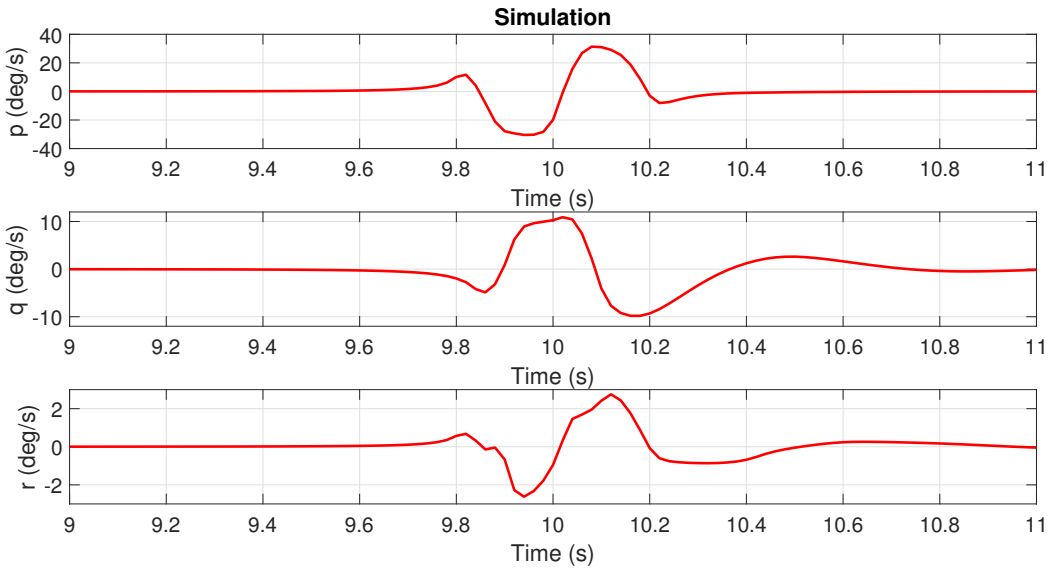

Figure 5.34: Rotation rates of the follower during wake encounter: simulation.

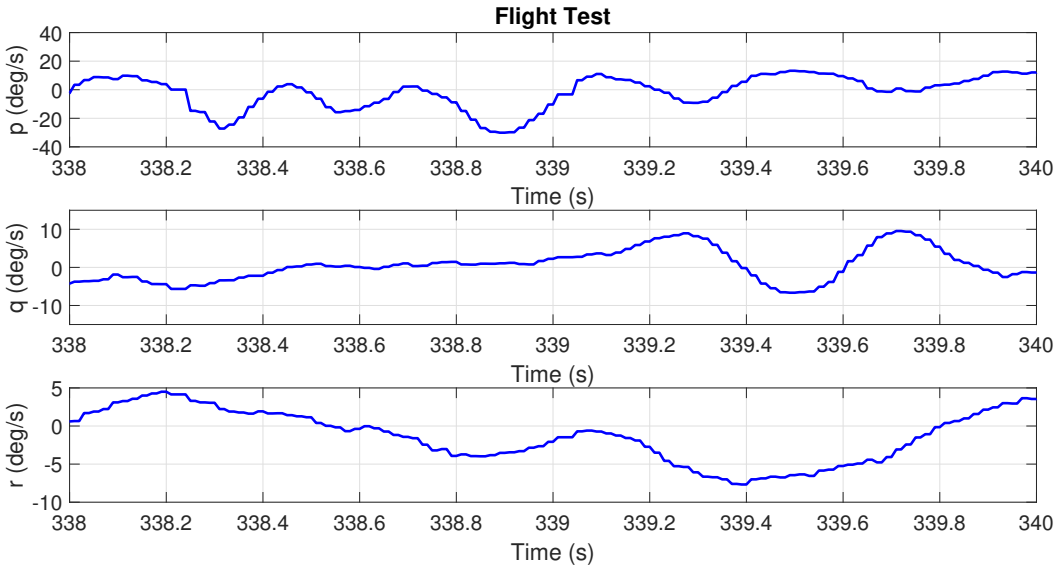

Figure 5.35: Rotation rates of the follower during wake encounter: flight test.

Chapter 6

Conclusions and Future Work

6.1 Conclusions

This dissertation provides new approaches on how to use UAVs to sense and estimate surrounding flow fields and on how to model and simulate UAV responses to certain dynamic flow fields, especially wake vortices. The goal is to narrow the gaps between the aircraft navigation and control community, the aerodynamics and fluid dynamics community, and the meteorological community by using small fixed-wing UAVs as effective wind/flow sensing platforms. Specifically, a thorough survey of wind field sensing and estimation methods using small fixed-wing UAVs is provided in Chapter 2. Chapter 3 focuses on the AOA and AOS estimation problem for small UAVs. CF and EKF based AOA/AOS estimation filters are designed and evaluated on two different UAV platforms. Simulation and flight test results show that proposed filters are able to estimate AOA and AOS without direct flow angle and GPS measurements accurately. The root mean square errors of estimated inertial AOA and AOS are less than 1.5 degrees under nominal flight conditions and around 2 degrees under aggressive maneuvers, compared with direct flow angle measurements obtained from flow angle vanes and 5-hole Pitot-tube. In Chapter 4, two EKFs (a 9-state EKF and a 12-state EKF) are proposed for the problem of 3D wind estimation without using direct flow angle measurements. Both filters are validated through simulation and UAV flight tests. Simulation results show that the proposed 9-state EKF can estimate 3D prevailing wind accurately while the 12-state EKF can estimate prevailing wind as well as sinusoidal wind wave. Furthermore, flight test results show that both filters can estimate 3D wind accurately when compared with mean wind measurements from a 3D sonic anemometer on the ground. Chapter 5 focuses on the modeling

and simulation of UAV wake encounters. A novel framework (HawkWakeSim) for UAV wake encounter simulation is designed and implemented, with coupled aerodynamics and flight dynamics. The proposed UAV wake encounter framework is validated by both simulation and UAV close formation flight results. Several wake encounter scenarios with different lateral encounter angles and following clearances are simulated and investigated. UAV responses in one of the simulated scenarios are compared with experimental data obtained from a UAV close formation flight. Results from HawkWakeSim match the overall trend of flight test results, which demonstrates its effectiveness. Additionally, aircraft responses during wake encounters under different control configurations are simulated and analyzed.

6.2 Future Work

Several potential future directions can be explored from each of the three main focuses of the dissertation:

1. Airflow angle estimation
   - Theoretical analysis on sensitivity and observability of different filter formulations;
   - Online calibration of sensor biases and alignment errors.
2. Wind estimation
   - Refine wind and turbulence models and incorporate them with estimation filters;
   - Use switching wind models to support cases where UAVs fly in different types of wind fields;
   - Online gain tuning for EKFs in different wind conditions;
   - Cooperative wind field sensing and estimation using multiple UAVs;
   - Cross validation using more accurate ground truth such as LiDAR or SODAR.

3. Wake encounters

   - Enable real-time simulation capabilities through parallel computing;

   - Wake model parameter identification from flight test data.

References

[1] R. B. Stull, *An Introduction to Boundary Layer Meteorology*. Springer Science & Business Media, 1988, vol. 13.

[2] N. B. Negra, O. Holmstrøm, B. Bak-Jensen, and P. Sørensen, "Model of a synthetic wind speed time series generator," *Wind Energy: An International Journal for Progress and Applications in Wind Power Conversion Technology*, vol. 11, no. 2, pp. 193–209, 2008.

[3] A. Shamshad, M. Bawadi, W. W. Hussin, T. Majid, and S. Sanusi, "First and second order Markov chain models for synthetic generation of wind speed time series," *Energy*, vol. 30, no. 5, pp. 693–708, 2005.

[4] R. W. Beard and T. W. McLain, *Small Unmanned Aircraft: Theory and practice*. Princeton University Press, 2012.

[5] F. M. Hoblit, *Gust loads on aircraft: concepts and applications*. AIAA Education Series, AIAA, Reston, VA, 1988.

[6] U.S. Military Specification, *MIL-F-8785C*, 1980.

[7] U.S. Military Handbook, *MIL-HDBK-1797*, 1997.

[8] T. R. Oke, *Boundary Layer Climates*. Routledge, 2002.

[9] J. Gedeon, "Dynamic analysis of dolphin-style thermal cross-country flight: Part ii," *Technical Soaring*, vol. 3, no. 3, pp. 17–34, 1973.

[10] J. S. Touma, "Dependence of the wind profile power law on stability for various locations," *Journal of the Air Pollution Control Association*, vol. 27, no. 9, pp. 863–866, 1977.

[11] J. D. Holmes, *Wind Loading of Structures*. CRC press, 2018.

[12] D. Burnham and J. Hallock, "Chicago monostatic acoustic vortex sensing system. volume iv. wake vortex decay." Transportation systems Center Cambridge MA, Tech. Rep., 1982.

[13] T. Sarpkaya, "New model for vortex decay in the atmosphere," *Journal of Aircraft*, vol. 37, no. 1, pp. 53–61, 2000.

[14] J. Pahle, D. Berger, M. Venti, C. Duggan, J. Faber, and K. Cardinal, "An initial flight investigation of formation flight for drag reduction on the C-17 aircraft," in *AIAA Atmospheric Flight Mechanics Conference*. AIAA Paper 2012-4802, 2012.

[15] P. Oettershagen, F. Achermann, B. Müller, D. Schneider, and R. Siegwart, "Towards fully environment-aware UAVs: Real-time path planning with online 3D wind field prediction in complex terrain," *arXiv preprint arXiv:1712.03608*, 2017.

[16] F. Achermann, N. R. Lawrance, R. Ranftl, A. Dosovitskiy, J. J. Chung, and R. Siegwart, "Learning to predict the wind for safe aerial vehicle planning," in *2019 International Conference on Robotics and Automation (ICRA)*. IEEE Pages 2311–2317, 2019.

[17] R. M. Watson, J. N. Gross, Y. Bar-Sever, W. I. Bertiger, and B. J. Haines, "Flight data assessment of tightly coupled PPP/INS using real-time products," *IEEE Aerospace and Electronic Systems Magazine*, vol. 32, no. 8, pp. 10–21, 2017.

[18] C. Demonceaux, O. Morel, D. Fofi *et al.*, "Vision based UAV attitude estimation: Progress and insights," *Journal of Intelligent & Robotic Systems*, vol. 65, no. 1-4, pp. 295–308, 2012.

[19] W. Gracey, "Summary of methods of measuring angle of attack on aircraft," Langley Aeronautical Laboratory, Tech. Rep., 1958.

[20] S. A. Whitmore, R. J. Davis, and J. Fife, "In-flight demonstration of a real-time flush airdata sensing system," *Journal of Aircraft*, vol. 33, no. 5, pp. 970–977, 1996.

[21] T. K. McDevitt and F. K. Owen, "An optical angle of attack sensor," in *International Congress on Instrumentation in Aerospace Simulation Facilities*. IEEE Pages 113–124, 1989.

[22] R. Barthelmie, P. Crippa, H. Wang, C. Smith, R. Krishnamurthy, A. Choukulkar, R. Calhoun, D. Valyou, P. Marzocca, D. Matthiesen *et al.*, "3d wind and turbulence characteristics of the atmospheric boundary layer," *Bulletin of the American Meteorological Society*, vol. 95, no. 5, pp. 743–756, 2014.

[23] G. Bishop and G. Welch, "An introduction to the Kalman filter," *Proc of SIGGRAPH, Course*, vol. 8, no. 27599-23175, p. 41, 2001.

[24] H. Fang, N. Tian, Y. Wang, M. Zhou, and M. A. Haile, "Nonlinear bayesian estimation: from kalman filtering to a broader horizon," *IEEE/CAA Journal of Automatica Sinica*, vol. 5, no. 2, pp. 401–417, 2018.

[25] M. S. Arulampalam, S. Maskell, N. Gordon, and T. Clapp, "A tutorial on particle filters for online nonlinear/non-gaussian bayesian tracking," *IEEE Transactions on signal processing*, vol. 50, no. 2, pp. 174–188, 2002.

[26] H. Hong, M. Wang, F. Holzapfel, and S. Tang, "Fast real-time three-dimensional wind estimation for fixed-wing aircraft," *Aerospace Science and Technology*, vol. 69, pp. 674–685, 2017.

[27] K. T. Borup, T. I. Fossen, and T. A. Johansen, "A machine learning approach for estimating air data parameters of small fixed-wing uavs using distributed pressure sensors," *IEEE Transactions on Aerospace and Electronic Systems*, 2019.

[28] G. Balmer, T. Muskardin, S. Wlach, and K. Kondak, "Enhancing model-free wind estimation for fixed-wing UAV," in *2018 International Conference on Unmanned Aircraft Systems (ICUAS)*. IEEE Pages 1242–1247, 2018.

[29] A. Van den Kroonenberg, T. Martin, M. Buschmann, J. Bange, and P. Vörsmann, "Measuring the wind vector using the autonomous mini aerial vehicle M^2AV," *Journal of Atmospheric and Oceanic Technology*, vol. 25, no. 11, pp. 1969–1982, 2008.

[30] A. Rautenberg, M. S. Graf, N. Wildmann, A. Platis, and J. Bange, "Reviewing wind measurement approaches for fixed-wing unmanned aircraft," *Atmosphere*, vol. 9, no. 11, p. 422, 2018.

[31] T. Niedzielski, C. Skjøth, M. Werner, W. Spallek, M. Witek, T. Sawiński, A. Drzeniecka-Osiadacz, M. Korzystka-Muskała, P. Muskała, P. Modzel *et al.*, "Are estimates of wind characteristics based on measurements with Pitot tubes and GNSS receivers mounted on consumer-grade unmanned aerial vehicles applicable in meteorological studies?" *Environmental monitoring and assessment*, vol. 189, no. 9, p. 431, 2017.

[32] J. W. Langelaan, N. Alley, and J. Neidhoefer, "Wind field estimation for small unmanned aerial vehicles," *Journal of Guidance, Control, and Dynamics*, vol. 34, no. 4, pp. 1016–1030, 2011.

[33] B. Reineman. (2017) Measuring the ocean and air-sea interactions with unmanned aerial vehicles. [Online]. Available: https://alps-ocean.us/talks/day1/reineman.pdf

[34] A. Mohamed, M. Abdulrahim, S. Watkins, and R. Clothier, "Development and flight testing of a turbulence mitigation system for micro air vehicles," *Journal of Field Robotics*, vol. 33, no. 5, pp. 639–660, 2016.

[35] J. Reuder and M. O. Jonassen, "First results of turbulence measurements in a wind park with the small unmanned meteorological observer SUMO," *Energy Procedia*, vol. 24, pp. 176–185, 2012.

[36] F. A. P. Lie and D. Gebre-Egziabher, "Synthetic air data system," *Journal of Aircraft*, vol. 50, no. 4, pp. 1234–1249, 2013.

[37] A. Cho, J. Kim, S. Lee, and C. Kee, "Wind estimation and airspeed calibration using a UAV with a single-antenna GPS receiver and pitot tube," *IEEE Transactions on Aerospace and Electronic Systems*, vol. 47, no. 1, pp. 109–117, 2011.

[38] T. A. Johansen, A. Cristofaro, K. Sørensen, J. M. Hansen, and T. I. Fossen, "On estimation of wind velocity, angle-of-attack and sideslip angle of small UAVs using standard sensors," in *2015 International Conference on Unmanned Aircraft Systems (ICUAS)*. IEEE Pages 510–519, 2015.

[39] M. Brossard, J.-P. Condomines, and S. Bonnabel, "Tightly coupled navigation and wind estimation for mini UAVs," in *AIAA Guidance, Navigation, and Control Conference*. AIAA Paper 2018-1843, 2018.

[40] A. Cho, Y.-s. Kang, B.-j. Park, and C.-s. Yoo, "Airflow angle and wind estimation using GPS/INS navigation data and airspeed," in *2013 13th International Conference on Control, Automation and Systems (ICCAS)*. IEEE Pages 1321–1324, 2013.

[41] A. Wenz, T. A. Johansen, and A. Cristofaro, "Combining model-free and model-based angle of attack estimation for small fixed-wing UAVs using a standard sensor suite," in *International Conference on Unmanned Aircraft Systems*. IEEE Pages 624–632, 2016.

[42] P. Tian and H. Chao, "Model aided estimation of angle of attack, sideslip angle, and 3D wind without flow angle measurements," in *AIAA Guidance, Navigation, and Control Conference*. AIAA Paper 2018-1844, 2018.

[43] H. Ryu and S. Park, "Vision-based wind and position estimation with fixed-wing unmanned aerial vehicle," *Journal of Guidance, Control, and Dynamics*, vol. 41, no. 10, pp. 2283–2292, 2018.

[44] I. Guilliard, R. Rogahn, J. Piavis, and A. Kolobov, "Autonomous thermalling as a partially observable Markov decision process (extended version)," *arXiv preprint arXiv:1805.09875*, 2018.

[45] M. B. Rhudy, Y. Gu, J. N. Gross, and H. Chao, "Onboard wind velocity estimation comparison for unmanned aircraft systems," *IEEE Transactions on Aerospace and Electronic Systems*, vol. 53, no. 1, pp. 55–66, 2017.

[46] M. B. Rhudy, T. Larrabee, H. Chao, Y. Gu, and M. Napolitano, "UAV attitude, heading, and wind estimation using GPS/INS and an air data system," in *AIAA Guidance, Navigation, and Control Conference*. AIAA Paper 2013-5201, 2013.

[47] M. B. Rhudy, Y. Gu, and H. Chao, "Wind field velocity and acceleration estimation using a small UAV," in *AIAA Modeling and Simulation Technologies Conference*. AIAA Paper 2014-2647, 2014.

[48] S. Notter, P. Schrapel, P. Groß, and W. Fichter, "Estimation of multiple thermal updrafts using a particle filter approach," in *AIAA Guidance, Navigation, and Control Conference*. AIAA Paper 2018-1854, 2018.

[49] S. Mayer, G. Hattenberger, P. Brisset, M. O. Jonassen, and J. Reuder, "A 'no-flow-sensor' wind estimation algorithm for unmanned aerial systems," *International Journal of Micro Air Vehicles*, vol. 4, no. 1, pp. 15–30, 2012.

[50] S. Park, "Autonomous crabbing by estimating wind using only GPS velocity," *IEEE Transactions on Aerospace and Electronic Systems*, vol. 52, no. 3, pp. 1399–1407, 2016.

[51] H. Chao, Y. Gu, P. Tian, Z. C. Zheng, and M. R. Napolitano, "Wake vortex detection with UAV close formation flight," in *AIAA Atmospheric Flight Mechanics Conference*. AIAA Paper 2015-2396, 2015.

[52] R. Jategaonkar, *Flight Vehicle System Identification: A Time Domain Methodology*. AIAA Progress in Astronautics and Aeronautics, AIAA, Reston, VA, 2006, vol. 216.

[53] K. Sun, C. D. Regan, and D. Gebre-Egziabher, "Observability and performance analysis of a model-free synthetic air data estimator," *Journal of Aircraft*, vol. 56, no. 4, pp. 1471–1486, 2019.

[54] L. Rodriguez, J. A. Cobano, and A. Ollero, "Wind field estimation and identification having shear wind and discrete gusts features with a small UAS," in *2016 IEEE/RSJ International Conference on Intelligent Robots and Systems (IROS)*. IEEE Pages 5638–5644, 2016.

[55] J. W. Langelaan, J. Spletzer, C. Montella, and J. Grenestedt, "Wind field estimation for autonomous dynamic soaring," in *2012 IEEE International Conference on Robotics and Automation*. IEEE Pages 16–22, 2012.

[56] P. Tian, H. Chao, and H. Wu, "UAS-based wind estimation using sinusoidal gust model," in *AIAA Atmospheric Flight Mechanics Conference*. AIAA Paper 2019-1597, 2019.

[57] J. D. Anderson Jr, *Fundamentals of Aerodynamics*. McGraw-Hill Education, Sixth Edition, 2017.

[58] V. Klein and E. A. Morelli, *Aircraft System Identification: Theory and Practice*. AIAA Education Series, AIAA, Reston, VA, 2006.

[59] P. Bala, E. Kupcis, and W. Fisher, "Aircraft stall warning system," Mar. 13 1990, US Patent 4,908,619. [Online]. Available: https://www.google.com/patents/US4908619

[60] P. Catlin, D. Ballard, G. Watson, and A. Worden, "Aircraft stall warning system," Jan. 21 1997, uS Patent 5,595,357. [Online]. Available: https://www.google.com/patents/US5595357

[61] B. d'Enquetes et d'Analyses, "Final report on the accident on 1st june 2009 to the airbus a330-203 registered f-gzcp operated by air france flight af 447 rio de janeiro–paris," *Paris, France: BEA*, 2012.

[62] K. A. Wise, "Flight testing of the X-45A J-UCAS computational alpha-beta system," in *AIAA Guidance, Navigation, and Control Conference and Exhibit*. AIAA Paper 2006-6215, 2006.

[63] D. Fischenberg, "A method to validate wake vortex encounter models from flight test data," in *27th International Congress of the Aeronautical Sciences*. ICAS 2010-6.9.1, 2010.

[64] E. A. Haering Jr, "Airdata measurement and calibration," NASA, Tech. Rep., 1995.

[65] ——, "Airdata calibration of a high-performance aircraft for measuring atmospheric wind profiles," NASA, Tech. Rep., 1990.

[66] E. A. Morelli, "Real-time aerodynamic parameter estimation without air flow angle measurements," *Journal of Aircraft*, vol. 49, no. 4, pp. 1064–1074, 2012.

[67] T. Berger, M. Tischler, S. G. Hagerott, D. Gangsaas, and N. Saeed, "Longitudinal control law design and handling qualities optimization for a business jet flight control system," in *AIAA Atmospheric Flight Mechanics Conference*. AIAA Paper 2012-4503, 2012.

[68] ——, "Lateral/directional control law design and handling qualities optimization for a business jet flight control system," in *AIAA Atmospheric Flight Mechanics Conference*. AIAA Paper 2013-4506, 2013.

[69] R. P. Quinlivan, "Aircraft angle-of-attack and sideslip estimator," Sep. 6 1977, uS Patent 4,046,341. [Online]. Available: https://www.google.com/patents/US4046341

[70] J. E. Zeis, "Angle of attack and sideslip estimation using an inertial reference platform," Master Thesis, Air Force Institute of Technology, 1988.

[71] R. D. Colgren, "Method and system for estimation and correction of angle-of-attack and sideslip angle from acceleration measurements," Aug. 14 2001, uS Patent 6,273,370. [Online]. Available: https://www.google.com/patents/US6273370

[72] N. Shantha Kumar and G. Girija, "Filtering and fusion based reconstruction of angle of attack," in *National Conference on Range Technology*, 2006.

[73] S. Myschik, F. Holzapfel, and G. Sachs, "Low-cost sensor based integrated airdata and navigation system for general aviation aircraft," in *Proceedings of AIAA Guidance, Navigation, and Control Conference and Exhibit*. AIAA Paper 2008-7423, 2008.

[74] J. Perry, A. Mohamed, B. Johnson, and R. Lind, "Estimating angle of attack and sideslip under high dynamics on small UAVs," in *the 21st International Technical Meeting of the Satellite Division of The Institute of Navigation*, 2008.

[75] C. Ramprasadh and H. Arya, "Multistage-fusion algorithm for estimation of aerodynamic angles in mini aerial vehicle," *Journal of Aircraft*, vol. 49, no. 1, pp. 93–100, 2012.

[76] M. Heller, S. Myschik, F. Holzapfel, and G. Sachs, "Low-cost approach based on navigation data for determining angles of attack and sideslip for small aircraft," in *AIAA Guidance, Navigation, and Control Conference and Exhibit*. AIAA Paper 2003-5777, 2003.

[77] P. Tian, H. Chao, Y. Gu, and S. G. Hagerott, "UAV flight test evaluation of fusion algorithms for estimation of angle of attack and sideslip angle," in *AIAA Guidance, Navigation, and Control Conference*. AIAA Paper 2016-0645, 2016.

[78] NASA. (2015) Inclination effects on lift. [Online]. Available: https://www.grc.nasa.gov/www/k-12/airplane/incline.html

[79] F. R. David. (2015) Absolute angle of attack. [Online]. Available: http://www.nar-associates.com/technical-flying/angle_of_attack/absolute_wide_screen.pdf

[80] Wikipedia. (2017) Slip (aerodynamics). [Online]. Available: https://en.wikipedia.org/wiki/Slip_(aerodynamics)

[81] B. Martos and D. F. Rogers, "Low cost accurate angle of attack system," in *55th AIAA Aerospace Sciences Meeting*. AIAA Paper 2017-1215, 2017.

[82] P. Tian, A. He, H. Chao, Z. C. Zheng, and Y. Gu, "Wake encounter simulation and flight validation with UAV close formation flight," in *AIAA Guidance, Navigation, and Control Conference*. AIAA Paper 2017-1910, 2017.

[83] J. L. Crassidis, F. L. Markley, and Y. Cheng, "Survey of nonlinear attitude estimation methods," *Journal of Guidance, Control, and Dynamics*, vol. 30, no. 1, pp. 12–28, 2007.

[84] J. N. Gross, Y. Gu, M. B. Rhudy, S. Gururajan, and M. R. Napolitano, "Flight-test evaluation of sensor fusion algorithms for attitude estimation," *IEEE Transactions on Aerospace and Electronic Systems*, vol. 48, no. 3, pp. 2128–2139, 2012.

[85] M. R. Napolitano, H. Chao, Y. Gu, C. E. Hanson, and M. T. Stanley, "Cooperative gust sensing and suppression for aircraft formation flight," NASA LEARN Project Phase I, Final Report, Tech. Rep., 2014.

[86] M. Rhudy, J. Gross, Y. Gu, and M. Napolitano, "Fusion of GPS and redundant IMU data for attitude estimation," in *AIAA Guidance, Navigation, and Control Conference*. AIAA Paper 2012-5030, 2012.

[87] Y. Gu, S. Gururajan, B. Seanor, H. Chao, and M. R. Napolitano, "Building better tools: Experimental UAV research at West Virginia University," in *American Control Conference*. IEEE Pages 1454–1459, 2013.

[88] MicroStrain, *3DM-GX3®-25 Datasheets*, LORD Corporation, 2014.

[89] A. K. McGrail, "Onboard parameter identification for a small UAV," Master Thesis, West Virginia University, 2012.

[90] H. Chao, H. P. Flanagan, P. Tian, and S. G. Hagerott, "Flight test investigation of stall/spin detection techniques for a flying wing UAS," in *AIAA Atmospheric Flight Mechanics Conference*. AIAA Paper 2017-1631, 2017.

[91] MicroStrain, *3DM-GX3®-25 Data Communications Protocol*, MicroStrain Inc., 2011.

[92] W. Gracey, "Measurement of aircraft speed and altitude," Langley Research Center, Tech. Rep., 1980.

[93] L. Van Eykeren and Q. Chu, "Sensor fault detection and isolation for aircraft control systems by kinematic relations," *Control Engineering Practice*, vol. 31, pp. 200–210, 2014.

[94] FAA. (2018) FAA releases 2016 to 2036 aerospace forecast. [Online]. Available: https://www.faa.gov/news/updates/?newsId=85227

[95] I. Van der Hoven, "Power spectrum of horizontal wind speed in the frequency range from 0.0007 to 900 cycles per hour," *Journal of Meteorology*, vol. 14, no. 2, pp. 160–164, 1957.

[96] T. J. Mueller and J. D. DeLaurier, "Aerodynamics of small vehicles," *Annual Review of Fluid Mechanics*, vol. 35, no. 1, pp. 89–111, 2003.

[97] S. Watkins, J. Milbank, B. J. Loxton, and W. H. Melbourne, "Atmospheric winds and their implications for microair vehicles," *AIAA Journal*, vol. 44, no. 11, pp. 2591–2600, 2006.

[98] S. Watkins, M. Thompson, B. Loxton, and M. Abdulrahim, "On low altitude flight through the atmospheric boundary layer," *International Journal of Micro Air Vehicles*, vol. 2, no. 2, pp. 55–68, 2010.

[99] N. Lawrance and S. Sukkarieh, "Wind energy based path planning for a small gliding unmanned aerial vehicle," in *AIAA Guidance, Navigation, and Control Conference*. AIAA Paper 2009-6112, 2009.

[100] J. W. Langelaan, "Gust energy extraction for mini and micro uninhabited aerial vehicles," *Journal of Guidance, Control, and Dynamics*, vol. 32, no. 2, pp. 464–473, 2009.

[101] J. H. Lee, H. E. Sevil, A. Dogan, and D. Hullender, "Estimation of maneuvering aircraft states and time-varying wind with turbulence," *Aerospace Science and Technology*, vol. 31, no. 1, pp. 87–98, 2013.

[102] M. B. Rhudy, M. L. Fravolini, M. Porcacchia, and M. R. Napolitano, "Comparison of wind speed models within a Pitot-free airspeed estimation algorithm using light aviation data," *Aerospace Science and Technology*, vol. 86, pp. 21–29, 2019.

[103] D. Long, "Modelling and measurement of near-surface oceanic winds," *International Journal of Modelling and Simulation*, vol. 13, no. 4, pp. 156–161, 1993.

[104] V. A. Banakh and I. N. Smalikho, "Lidar observations of atmospheric internal waves in the boundary layer of the atmosphere on the coast of Lake Baikal," *Atmospheric Measurement Techniques*, vol. 9, no. 10, pp. 5239–5248, 2016.

[105] C. Patel and I. Kroo, "Control law design for improving UAV performance using wind turbulence," in *44th AIAA Aerospace Sciences Meeting and Exhibit*. AIAA Paper 2006-231, 2006.

[106] N. Gavrilovic, E. Benard, P. Pastor, and J.-M. Moschetta, "Performance improvement of small unmanned aerial vehicles through gust energy harvesting," *Journal of Aircraft*, vol. 55, no. 2, pp. 741–754, 2017.

[107] R. E. Bartels, "Development, verification and use of gust modeling in the NASA computational fluid dynamics code FUN3D," NASA, Tech. Rep., 2012.

[108] P. Tian, H. Chao, H. P. Flanagan, S. G. Hagerott, and Y. Gu, "Design and evaluation of UAV flow angle estimation filters," *IEEE Transactions on Aerospace and Electronic Systems*, vol. 55, no. 1, pp. 371–383, 2019.

[109] C. K. Patel and I. M. Kroo, "Theoretical and experimental investigation of energy extraction from atmospheric turbulence," in *26th International Congress of the Aeronautical Sciences*, 2008.

[110] FAA. (2015) Air traffic organization policy. [Online]. Available: https://www.faa.gov/news/updates/?newsId=85227

[111] F. Proctor and D. Hamilton, "Evaluation of fast-time wake vortex prediction models," in *47th AIAA Aerospace Sciences Meeting including The New Horizons Forum and Aerospace Exposition*. AIAA Paper 2009-344, 2009.

[112] M. J. Vachon, R. Ray, K. Walsh, and K. Ennix, "F/A-18 aircraft performance benefits measured during the autonomous formation flight project," in *AIAA Atmospheric Flight Mechanics Conference and Exhibit*. AIAA Paper 2002-4491, 2002.

[113] A. Dogan, S. Venkataramanan, and W. Blake, "Modeling of aerodynamic coupling between aircraft in close proximity," *Journal of Aircraft*, vol. 42, no. 4, pp. 941–955, 2005.

[114] D. Saban, J. F. Whidborne, and A. Cooke, "Simulation of wake vortex effects for UAVs in close formation flight," *The Aeronautical Journal*, vol. 113, no. 1149, pp. 727–738, 2009.

[115] A. Inasawa, F. Mori, and M. Asai, "Detailed observations of interactions of wingtip vortices in close-formation flight," *Journal of Aircraft*, vol. 49, no. 1, pp. 206–213, 2012.

[116] J. R. Branstetter, E. Hastings Jr, and J. C. Patterson Jr, "Flight test to determine feasibility of a proposed airborne wake vortex detection concept." DTIC Document, Tech. Rep., 1991.

[117] T. Lampe, Y. Sedin, and P. Weinerfelt, "Flight test verification of a wake vortices model," in *Flight Test–Sharing Knowledge and Experience Meeting Proceedings*. RTO-MP-SCI-162 Pages 4-1–4-16, 2005.

[118] G. T. Spence, A. L. Moigne, D. J. Allerton, and N. Qin, "Wake vortex model for real-time flight simulation based on large eddy simulation," *Journal of Aircraft*, vol. 44, no. 2, pp. 467–475, 2007.

[119] D. Vicroy, P. Vijgen, H. Reimer, J. Gallegos, and P. Spalart, "Recent NASA wake-vortex flight tests, flow-physics database and wake-development analysis," in *AIAA and SAE, 1998 World Aviation Conference*. AIAA Paper 1998-5592, 1998, p. 5592.

[120] T. Melin, "A vortex lattice MATLAB implementation for linear aerodynamic wing applications," Master Thesis, Royal Institute of Technology (KTH), Sweden, 2000.

[121] T. Larrabee, H. Chao, M. Rhudy, Y. Gu, and M. R. Napolitano, "Wind field estimation in UAV formation flight," in *2014 American Control Conference*. IEEE Pages 5408–5413, 2014.

[122] A. He, H. Chao, Z. C. Zheng, and P. Tian, "Development of a coupled CFD simulation with flihgt control algorithm," in *Proceedings of the ASME 2016 IMECE*. IMECE 2016-65971, 2016.

[123] A. He, Z. C. Zheng, H. Chao, P. Tian, and Y. Gu, "A study on wake turbulence encounter during UAV formation flight using coupled aerodynamics/flight dynamics simulation," in *8th AIAA Atmospheric and Space Environments Conference*. AIAA Paper 2016-3439, 2016.

Publication List

Journal Papers

1. **Pengzhi Tian**, Haiyang Chao, Harold Patrick Flanagan, Steven G. Hagerott, and Yu Gu, Design and Evaluation of UAV Flow Angle Estimation Filters, IEEE Transactions on Aerospace and Electronic Systems, Vol. 55, Issue 1, pp. 371-383, February, 2019.

2. **Pengzhi Tian**, Haiyang Chao, Huixuan Wu, Huazhen Fang, and Nathaniel A. Brunsell, 3D Wind Estimation for Unmanned Aerial Vehicles without Air Flow Angle Measurements, under preparation, 2020.

3. **Pengzhi Tian**, Haiyang Chao, Wind Sensing and Estimation Using Small Fixed-Wing UAVs: A Survey, under preparation, 2020.

4. Saket Gowravaram, Haiyang Chao, Andrew Molthan, Tiebiao Zhao, **Pengzhi Tian**, Harold Flanagan, Lori Schultz, and Jordan Bell, Radiometric Cross-Calibration of UAS Multispectral Imagery Using Free and Open Satellite Surface Reflectance Images, under preparation, 2020.

Conference Papers

1. Haiyang Chao, Justin Mat, Harold Patrick Flanagan, **Pengzhi Tian**, and Saket Gowravaram, Atmospheric Sensing of Wildland Fire Plumes Using KHawk UAS, 100th American Meteorological Society Annual Meeting, January, 2020.

2. **Pengzhi Tian**, Haiyang Chao, and Huixuan Wu, UAS-based Wind Estimation Using Sinusoidal Gust Model, AIAA Atmospheric Flight Mechanics Conference, January, 2019.

3. Saket Gowravaram, Haiyang Chao, Andrew L. Molthan, Lori A. Schultz, J. R. Bell, **Pengzhi Tian**, and Harold Patrick Flanagan, Evaluating the 22 June 2017 South Dakota hail damage using KHawk UAS: Accuracy quantification and cross validation with satellite imagery, 99th American Meteorological Society Annual Meeting, January, 2019.

4. Saket Gowravaram, **Pengzhi Tian**, Harold Patrick Flanagan, Jacksen Hugh Goyer, and Haiyang Chao, UAS-based Multispectral Remote Sensing and NDVI Calculation for Post Disaster Assessment Presentation, International Conference on Unmanned Aircraft Systems, June, 2018.

5. **Pengzhi Tian** and Haiyang Chao, Model Aided Estimation of Angle of Attack, Sideslip Angle, and 3D Wind without Flow Angle Measurements, AIAA Guidance, Navigation, and Control Conference, January, 2018.

6. Saket Gowravaram, Harold Patrick Flanagan, **Pengzhi Tian**, and Haiyang Chao, Prescribed Fire Monitoring Using KHawk Unmanned Aircraft Systems, AIAA Infotech Conference, January, 2018.

7. **Pengzhi Tian**, Anpeng He, Haiyang Chao, Zhongquan Charlie Zheng, and Yu Gu, Wake Encounter Simulation and Flight Validation with UAV Close Formation Flight, AIAA Guidance, Navigation, and Control Conference, January, 2017.

8. Haiyang Chao, Harold Patrick Flanagan, **Pengzhi Tian**, and Steven G. Hagerott, Flight Test Investigation of Stall/Spin Detection Techniques for a Flying Wing UAS, AIAA Atmospheric Flight Mechanics Conference, January, 2017.

9. Anpeng He, Zhongquan Charlie Zheng, Haiyang Chao, and **Pengzhi Tian**, Development of a Coupled CFD Simulation with Flight Control Algorithm, ASME 2016 IMECE, November,2016

10. Anpeng He, **Pengzhi Tian**, Zhongquan Charlie Zheng, and Haiyang Chao, A Study on UAS Wake Turbulence Encounter Using Coupled Aerodynamics and Flight Dynamics Simulation, AIAA Atmospheric and Space Environments Conference, June, 2016.

11. **Pengzhi Tian**, Haiyang Chao, Yu Gu, and Steven G. Hagerott, UAV Flight Test Evaluation of Fusion Algorithms for Estimation of Angle of Attack and Sideslip Angle, AIAA Guidance, Navigation, and Control Conference, January, 2016.

12. Haiyang Chao, Yu Gu, **Pengzhi Tian**, Zhongquan Zheng, and Marcello Napolitano, Wake Vortex Detection with UAV Close Formation Flight, AIAA Atmospheric Flight Mechanics Conference, June, 2015.